THE UNIVERSITY *of* EDINBURGH

Improving the Torque Density of C-GEN Direct Drive Axial Flux Air Cored Permanent Magnet Generator

Okechukwu Godswill Ubani

Doctor of Philosophy

The University of Edinburgh

2020

To my loving Father,

Without whom this would not have been possible

Onyemaechi Onwubiko Ubani

Abstract

In the energy sector, the fossil fuels available are being exhausted and to support the increase in energy demand and reduction of greenhouse gases, countries are looking towards renewable energy. Wind power offers many advantages, which explains why it's one of the fastest-growing energy source and it is expected to continue to flourish as countries seek to reduce their carbon footprint.

The newer wind turbines are better at generating wind power, especially in variable wind speeds. They have bigger rotors, higher towers, and lighter blades which increases the capacity of the turbine, therefore, improving reliability and efficiency. Nevertheless, as wind turbines grow increasingly in size and weight, this can make it difficult to manufacture and to transport the generator as a whole. The C-GEN air-cored permanent magnet machine offers many attractive advantages over existing generator technologies used for direct drive. It's modular concept makes it easy to assemble and disassemble for transportation, manufacture and repairs. The output power depends on the number of stages among other factors, which gives rise to the idea of stackability.

This thesis lays out the concept and operating principles of Halbach arrays and applies it to a C-GEN Axial Flux Air-Cored Permanent Magnet Generator. The machine is analysed using analytical methods and 2D/3D FEA simulations. A conclusion of the undertaking is given with a brief discussion of possible design considerations in a bid to find a highly torque-dense generator.

Acknowledgements

I must express my thanks to all those who helped in realising and implementing the objectives described in this work.

A heartfelt gratitude goes to my supervisors, Dr John Chick and Professor Markus Mueller. Both gave me ideas, constant help, guidance and support during the course of my research. This work would not have been possible without them. I also would like to thank Dr Alasdair McDonald, who found time to allow me pick his brain, our conversations were invaluable.

I will be remiss if I didn't express my appreciation to William K. Thompson of the Glenn Research Center, Cleveland, Ohio for the resources and ideas he offered. I am thankful as it all aided in the realisation of this undertaking.

I thank the scholarship I received from the University of Edinburgh, Energy Technology Partnership (ETP) and the now dismantled NGenTec Ltd.

I would like to thank Dr Prashant Valluri and the School of Engineering for the support and patience I was given throughout my family's ordeal.

Thanks to all the friends and colleagues that were part of the long and difficult joumey towards the completion of this disertation. Dr Renaldi Renaldi, Dr Hawwooi Chuan, Dr. Ozan Keysan, Dr. Joseph Burcell, Dr. Jose Ignacio Barajas Solano, Dr. Kaswar Mostafa, Dr Juan Pablo Echenique, Dr Winnie Xiayun Rong, Dr Monika Kreitmair, Dr. Anna Garcia-Teruel, Dr Ben Mcgilton and the triple A group. Thanks for sharing your knowledge and welcomed distractions.

Finally, to my dear friends in Manchester, family and beloved partner Cherie Whitlock I am grateful and humbled to have you in my life, through the good and bad you have been there and to that I owe you.

Declaration

I declare that this thesis was composed by myself, that the work contained herein is my own except where explicitly stated otherwise in the text, and that this work has not been submitted for any other degree or professional qualification except as specified.

Okechukwu Godswill Ubani

Contents

Figures and Tables

Figures

Tables

Nomenclature

α	Temperature Coefficient
$\boldsymbol{\phi}$	Magnetic Flux
$\hat{\mathbf{n}}$	The outward unit normal
$\hat{B}_g$	Peak Airgap Flux Density
λ	wavelength of the array between like poles
μ	Permeability of a Material
μ_o	Permeability of Free Space
μ_r	Relative Permeability
ρ	Electrical Resistivity
σ	Electrical Conductivity
σ_m	Surface Charge Density
τ_m	Magnet/Iron Width Ratio
$\mathbf{j}_m$	Surface Current Density
$\mathbf{x}$	Observation Point
$\mathbf{x}'$	Source Point
A_{rms}	Electric Loading
B_ϕ	Azimuthal Field Component
B_{gap}	Airgap Magnetic Flux Density
B_r	Radial Field Component
I_{load}	Load Current
k	wavenumber
N_m	Number of Magnets
P_{out}	Output Power
r_1	Inner Radius
r_2	Outer Radius
V_{load}	Load Voltage
$V_{no\ load}$	No Load Voltage
z_1	Bottom of Sector
z_2	Cylindrical Vector
z_2	Top of Sector
$\mathrm{B_r}$	Remanence Magnetisation

m_o	maximum magnitude of each component
m_r	resultant magnetization vector
m_x	magnetization vector in the x direction
m_y	magnetization vector in the y direction
m_z	magnetization vector in the z direction
B_{demag}	Demagnetization value
B_{PM}	Flux Density of the Magnet
B_{prox}	Demagnetization Proximity Field
H_{PM}	Field Strength of the Magnet
J	Electric Current Density
M	Normal Vector of Magnetization
m	Number of PM pieces per wavelength
P_E	Output Electrical Power
P_M	Input Mechanical Power
P_{LOSS}	Power Loss
T_0	No-load Operating Point at ambient
T_L	Load Operating Point
$\mathbf{A}$	Area through which the flux passes
$\mathbf{B}$	Magnetic Flux Density
$\mathbf{H}$	Magnetic Field Strength
$\mathbf{M}$	Magnetisation Vector
$\mathbf{m}$	Magnetic Dipole Moment
i	Indexing Variable
n	Index Number
g	Magnet Gap
h	Array Height
w	Magnet Width
x	Horizontal Displacement
y	Vertical Displacement
n	Harmonic Number
S	Surface
V	Volume

Chapter 1

Introduction

In this chapter the current state of wind power deployment is established followed by a discussion on the state of the art of drive-train technologies used in wind turbines. The chapter then lays out the aims of the thesis.

1.1 Global Status of Wind Energy

Increasing global energy demand, coupled with the emission of harmful gases caused by conventional fossil fuel energy plants, have resulted in a need for renewable energy sources to supply global demand. Wind technology has seen significant improvements over the last few years. For example there have been considerable advances in power electronics, improved planning and overall management, more affordable storage and better grid management which have led to

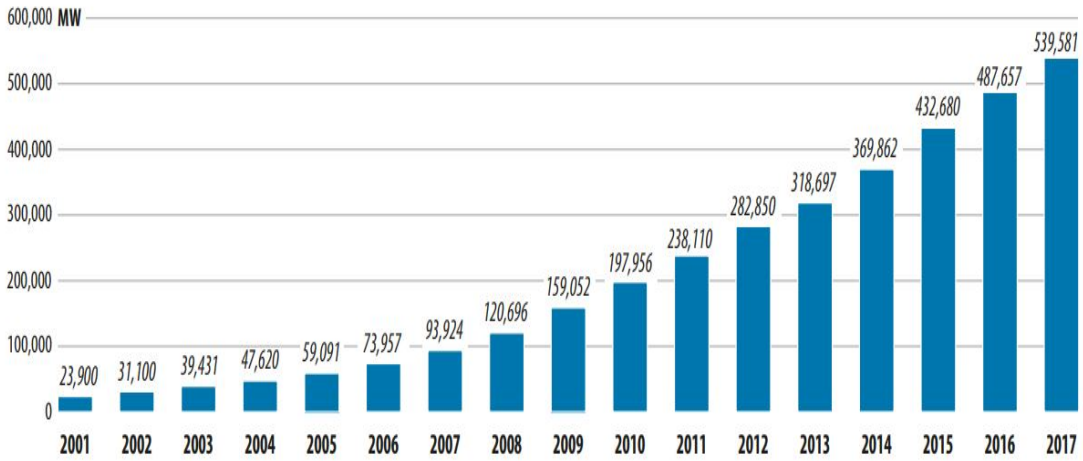

Figure 1.1: Global cumulative installed wind capacity 2001-2017 (Image taken from [1])

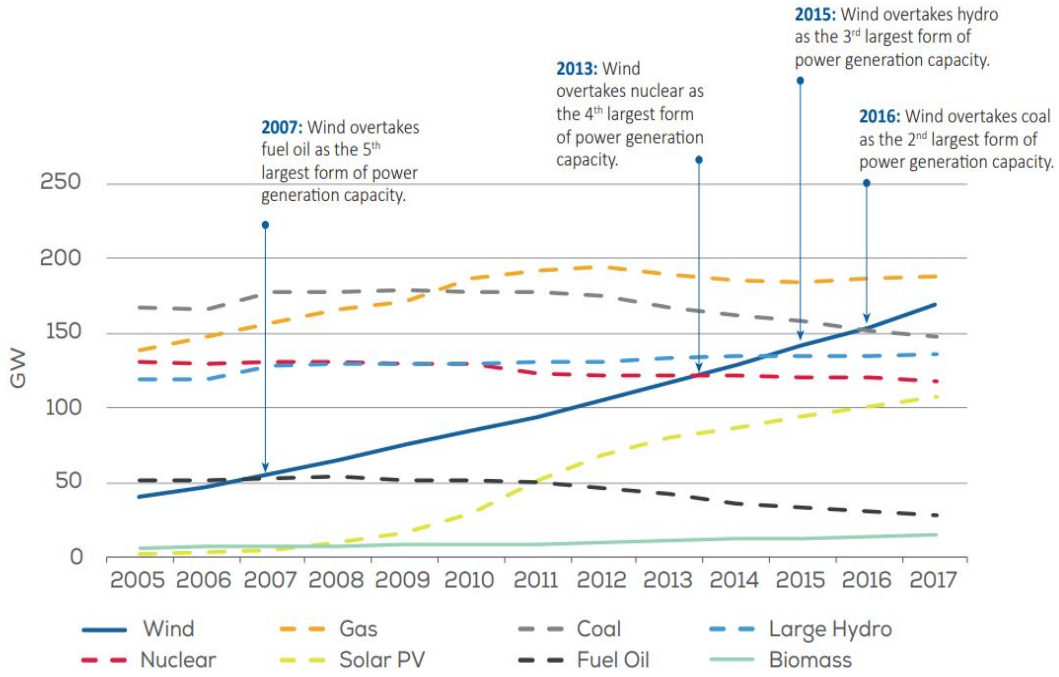

Figure 1.2: Total Power Generation Capacity in the European Union (EU) 2005 -2017 (Image taken from [2])

improved reliability and more competitive prices [1]. By the end of 2017 a total of 539 GW of global cumulative installed wind capacity was recorded by the Global Wind Energy Council [1] and Figure 1.1 illustrates the growth trend in installed wind capacity over the last two decades. The global installation of 52 GW of new wind power, despite representing a drop of 3% compared to growth of the previous year, is a result of wind energy now operating in increasingly more markets on a commercial basis.

The biggest driver of global market growth for most of the last decade remains China. It will cross the 200 GW mark in 2018, adding to an already exceptional history in renewable wind development. India set a record in 2017, by installing more than 4 GW of new wind capacity and it is expected to continue on this growth starting in 2019, contrary to a gap in 2018. This reinforces Asia as the biggest regional market for new wind power development, and it is expected to remain so for the foreseeable future [1].

Europe had an extraordinary record year in 2017, both offshore and onshore, adding 16.8 GW (15.6 GW in EU) of new wind power capacity to the grid with new records set in the UK, Germany, France, Belgium, Ireland and Croatia [2]. A total of 3.2 GW in the EU was offshore which doubled from the previous year

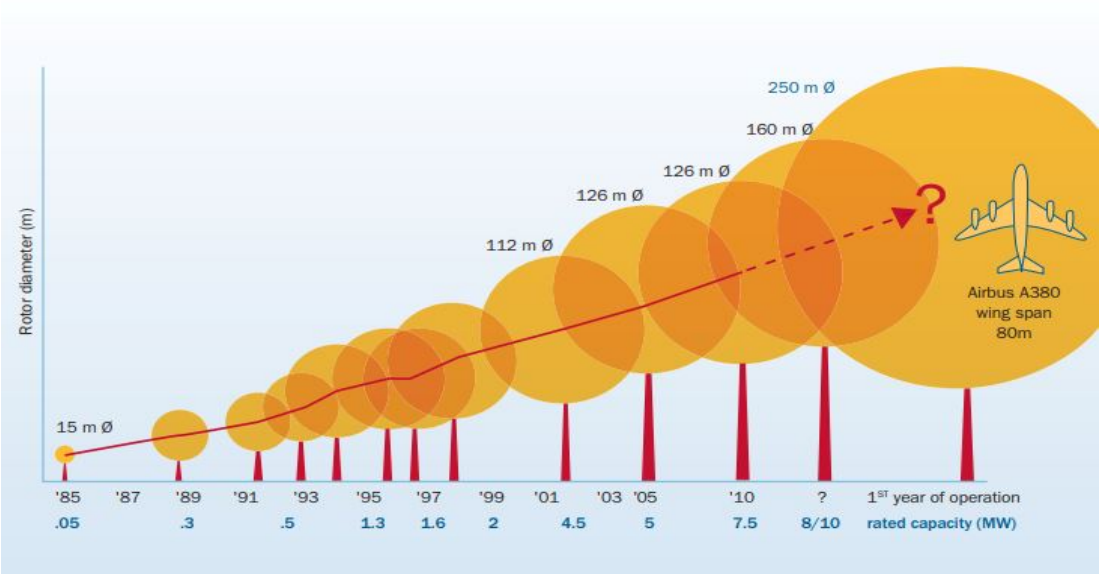

Figure 1.3: Increase in the wind turbines power rating and size in the last 30 years (Image taken from [3])

whilst onshore installations increased by 14% [1]. According to Wind Europe Annual Statistics 2017, wind power remains the second largest power resource in Europe, quickly approaching gas installations. The trend of wind power in comparison to other energy sources can be seen in Figure 1.2.

The UK is considered to be an offshore wind powerhouse with the largest amount of installed offshore wind capacity in Europe, representing 43% of all installations. A new wind capacity of 4.3 GW (1.7 GW offshore) was installed in 2017 in the UK, which is five times more than in 2016. Although, the UK comes in second to Germany, which enjoyed a 6.6 GW of new wind capacity, representing an increase of 15% compared to 2016 and of which 19% was offshore [2]. France came in third with 1.7 GW of onshore wind power capacity (9% increase over 2016), nevertheless, her total installed wind power capacity (13.5 GW) is enough to power 11 million homes [4] [5]. Spain installed only 96 MW of new wind power in 2017, although they remain a big player in the EU wind energy sector, being one of the three countries representing 58% of all the cumulative installed capacity, with Germany (56.1 GW) and the UK (23.2 GW) occupying the other two spots [2].

The US successfully installed over 7 GW of capacity in 2017, amidst the harsh policy environment. The US is second to China in terms of total installed capacity, with Texas remaining a big player in the country, with 22.7 GW of wind power at

the end of 2017. Brazil contributed over 2 GW of new wind capacity representing more than three quarters of the installations in the region. Brazil has "some of the best wind resources in the world." [1], 2017 was a record year for Brazil, generating 10% and 11% of national electricity demand in August and September respectively [1]. Canada continues to grow in installed capacity, with over 12 GW of installed wind energy capacity, capable of supplying 6% of the country's electricity demand as stated in Canadian Wind Energy Capacity (CWEA) report. Acccording to CWEA, 10 projects were completed that added 350 MW of installed capacity and it is expected to continue on this strong growth making Canada yet another global leader in wind energy [6].

Wind energy has developed gradually world wide and it is now the most competitively priced technology in many markets. The emergence of wind/solar hybrids, the presence of more sophisticated grid management and increasingly affordable storage, a fully commercial fossil-free future is on the horizon [1]. Nonetheless, reducing the cost of energy remains the biggest challenge facing the wind energy sector. The estimated cost for the installation of onshore wind turbines is €1.6 m/MW and nearly double that amount for offshore wind turbines [7]. As the turbines power ratings increase, the cost of installation and maintenance costs per kWh reduces, resulting in a trend towards higher power rated turbines [8]. This is why the size and power rating of wind turbines has increased tremendously over the last 30 years and this trend can be observed in Figure 1.3.

Offshore wind farms are advantageous due to the enormous amount of energy potential. The strong and steady wind flows imply greater power generation although they require greater initial investment, operational and maintenance cost compared to onshore [9] and the energy policy and regulations are important considerations for the cost of offshore wind energy. The Onshore wind energy market is considered to be relatively mature with offshore wind beginning to hit its stride in early 2017. In the EU, the global new installed offshore wind capacity in 2017 doubled from 2016 representing 3.2 GW of the 12.5 GW total installed whilst annual onshore installation increase by only 14%. Overall, there was a 25% increase of new installations compared to 2016 [1][2].

Nonetheless, the levelised cost of energy (LCOE) [1] still remains a factor especially

1. LCOE is essentially the cost of electricity. It is an economic assessment of the cost of energy including all the costs over its lifetime, that is, initial investment, operations and maintenance, cost of fuel, cost of capital divided by the total energy output over that lifetime.

for the offshore market aiming for large scale commercialisation [7]. The average LCOE of the offshore wind farms from projects reaching Final Investment Decision (FID) in the UK is £97/MWh during 2015-2016, achieving a 32% reduction when compared to 2012's figure of £142/MWh and this is as a result of the adoption of larger turbines, lower cost of capital, increased competition and change in policies [11]. This is a remarkable achievement, having come four years ahead of its 2020 schedule [11], but it is still more expensive than many new coal and gas power stations, which can cost as low as £39/MWh [12]. It is relevant to mention onshore wind does far better with an average of £49/MWh [7] and combined with the rapid cost reduction of offshore below levels set by any other large-scale, low-carbon energy source, points towards a future where wind energy can compete with conventional fossil fuels. Reducing the cost of energy is paramount in order for offshore wind to compete and it is largely dependent on reliability, availability and longevity of the wind turbines. These properties are improving as larger offshore turbines with optimized rotor diameter and improved control systems are deployed which boost wind turbine production and reliability but it remains necessary that there is a clear understanding of the factors that affect these properties if offshore wind is to survive the economic challenges of installation [13] [14].

Wind turbines require a significant amount of maintenance and regular servicing and if necessary repairs and this is purely down to the tough ambient conditions they are subjected to and the extremely high dynamic loading of the various components. Therefore, it is necessary to incorporate this into the design and selections of materials and in the selection of suitable drive train options based on the requirements, in order to mitigate or minimize component failure.

The next section, is a review of drive-train options inspired by the literature covered in [15].

1.2 Drive-Train Options for Wind Turbines

1.2.1 Direct Drive Permanent Magnet Generator System

The conventional mechanical gearbox is a mature technology. They are used in a considerable number of industries such as transport, energy and process industries and are considered as indispensable, vital components with significant high mean time to repair (MTTR) when compared to other subsystems. Gearbox failures have been a massive issue facing the wind turbine industry, accounting for extensive downtime and cost of repair. Although, they continue to be used as they are easily available and cheaper, and there exists a wealth of practical knowledge of geared wind turbines which has enabled better improvements on the design and prediction of fault over the years leading to better reliability [16] [17]. Nonetheless, direct-drive permanent magnet (DDPM) turbines offer an option of a drive train without a gearbox, therefore fewer moving parts, and ultimately improved reliability. Direct drive generators are capable of generating the required torque directly at their output shaft , without the need of a gearbox, thereby satisfying the requirement of high torque at low revolutions per minute (RPM) which is necessary as the focus here is larger diameter machines (high power rating). However, the biggest drawback of direct-drive is the high diameter resulting in considerably increased structural mass. For example, Enercon E-126 7.5 MW as seen in Figure 1.4, the structural support is greater than 60% of the total mass. A patented C-GEN air-cored permanent magnet has been proposed which reduces the structural mass of the generator by eliminating the stator iron [18][19].

Radial flux permanent magnet generators have been mostly used for large direct-drive, because of their simple and stable structure and higher power density. However the presence of permanent magnets makes the assembly more difficult especially in large machines and the possibilities for modularity are limited [15][8]. Transverse flux permanent magnet (TFPM) generators have a higher torque density compared to radial flux permanent magnet machines which reduces the size and mass of the machine, and with a more lightweight structure and modular opportunities makes it a good candidate. However, these types of machines are characterised by very complex flux path making their construction and manufacture difficult [15]. The C-GEN air-cored axial flux permanent magnet (ACAFPM) generator offers significant advantages over an equivalent RFPM; simple winding,

Figure 1.4: Enercon E-126 7.5MW, 13rpm excited synchronous generator (Image taken from [16])

no cogging torque, short axial length of machine, higher torque to volume ratio and interestingly an ease of modularity which can be significant when dealing with nacelle requirements. As with any technology it is not without shortcomings, the most significant of all is the larger outer diameter compared to RFPM, resulting in significantly more permanent magnets and structural instability [8]. Halbach array techniques have been adopted in a bid to reduce the permanent magnet content and structural mass with promising results, although, further study is required to understand its application in large scale wind turbines.

However, the dependency of the generator cost to fluctuations in Permanent Magnet (PM) prices makes DDPM generators very challenging. However, with technological innovation and competitiveness, this may lead to prolonged stability in prices [20].

1.2.2 Medium Speed Generator Option

In a bid to reduce the costs associated with the high amount of permanent magnets in DDPM generators, an alternative is the medium speed generator utilising single or double stage gearboxes and a medium speed permanent magnet generator, effectively offering a reduction in the required permanent magnet and the total generator mass [21]. They are considered to be an intermediate option between direct-drive and geared solutions [16], which is more reliable and highly

efficient. The generator and gearbox are typically of roughly the same size and are combined together to form a more balanced and compact single unit as opposed to a direct-drive solution and this is demonstrated in Multibrid technology. Here, the system is fitted directly in the main frame of the machine, and with the generator bearings being part of the gearbox assembly leads to a reduction in structural mass as well as a reduction in the number of bearings [22] [15]. The concept shows significant superiority in terms of annual energy production around the 5 MW over the direct-drive systems [22] but as stated in [15] its scalability in the very high MW, has not been proved yet.

1.2.3 Hydraulic Systems

In modern wind turbines, hydraulics have been mainly used for auxiliary mechanisms such as pitch systems intended to implement active control in wind turbines. In hydraulics systems, power is essentially transferred via the flow of a fluid. Robustness and high power density are features typical of fluid power transfer. This is as a result of the large force density possible to transmit by means of a fluid. Albeit, this large force density is still smaller compared to mechanical systems, it is only limited by the maximum pressure that a pump can reach rather than by the material properties which is often the case for mechanic power transfer [23]. There are some available hydraulic drive trains designs such as the WinDrive, ChapDrive, DOT and Artemis Digital Displacement, but the key concern with these designs, is how it responds to grid fault. Due to the lack of a middle stage between the generator and the grid, the adopted control loop would need to be fast enough to respond to a grid-fault with grid requirements [15]. Furthermore, with lower efficiencies in comparison to more common drive trains, this technology has struggled to see much traction [15].

1.2.4 Magnetically Geared Generators

Magnetic Gear solutions have been around for over 100+ year [24]. McGilton et al offers a review of the recent developments of the technology with a focus on marine energy. Magnetic gears operate by transmitting torque between input and output via magnetic attraction and repulsion between moving permanent magnets [16]. They are completely contactless, removing the need for lubrication and being able to achieve high torque densities makes them a great alternative to a conventional mechanical gearbox [24] [25]. The most common type of magnetic

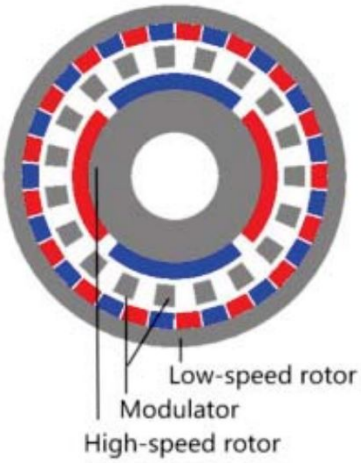

Figure 1.5: Concentric Magnetic Gear (Image taken from [24])

gear design is that proposed by Atallah et al, which is the Concentric Magnetic Gear and it is considered to be the modern leading design in magnetic gears [26]. These type of gears are able to achieve high torque densities in the range of 70 -150 kNm/m^3 which is comparable to that of traditional mechanical gear (50 -150 kNm/m^3) [24]. They are characterised by ferromagnetic segment in the air gap between the rotors to act as modulator of the magnetic flux, this is shown in Figure 1.5. It operates by either keeping the ferromagnetic poles stationary and high speed and low speed rotors are allowed to rotate or the ferromagnetic poles are allowed to rotate whilst keeping one of the rotors stationary. Both modes of operation affect the gear ratio and the direction of rotation [24].

It is clear magnetic gearboxes offers a promising alternative to reduce O&M costs and prolong the lifetime of future wind turbines. They are considered to be more reliable than conventional drive trains avoiding both limitations faced by geared and direct-drive and can achieve very high efficiencies of 99%. Nonetheless, this technology is not fully mature and with most design typically quite expensive, further study is required to allow magnetic gears to become an economically viable option [24].

1.3 Summary & Aim of Thesis

It is clear especially for offshore wind turbines that the power rating of these turbines is expected to continue to increase as it leads to a desirable reduction in the installation and operational costs. However, the issues of high tower head mass and reliability need to be tackled in order to provide a smooth pathway for offshore wind.

In wind turbine applications, the drive-train system must be designed for high reliability, good efficiency, and long service life with reasonable maintenance requirements. The C-GEN ACAFPM generators offer significant amount of attractive features which are outlined in this chapter. The high degree of modularity along with the air-cored windings has significant benefits in terms of component manufacture and assembly. However, the mass of such generators is a significant issue due to the considerable amount of permanent magnet material.

The main aim of this thesis is to improve the torque density performance of the C-GEN air-cored axial flux permanent magnet generator by using the state-of-the-art Halbach technology. The objectives include:

- To review the existing literature on Halbach array and its applications.
- To review the current state of the patented C-GEN technology.
- To develop analytical field expressions which can be used early on in the design process to assess the use of Halbach array in a C-GEN permanent magnet topology.
- To build finite element (FE) models to accurately perform analyses of the required designs and verify the analytical calculations.
- To compare the analytical and simulation results of the different generator designs with particular reference to the mass and torque density of these generators.

1.4 Layout of Thesis

This next chapter of this thesis introduces the phenomenon of Halbach array. The fundamental properties of Halbach array and some common applications are reviewed.

In Chapter 3, a review of NGenTec C-Gen direct-drive air-cored permanent magnet generators is presented, highlighting its merits and demerits.

Chapter 4, a review of the common Halbach Two dimensional magnetic field equation is presented alongside a common misconception and a more accurate three dimensional equation is explored and expanded upon to incorporate more degrees of rotation.

Chapter 5, presents the NGenTec 25 kW and 1 MW Axial Flux Permanent Magnet Generator. A Halbach C-GEN topology is proposed and 3D finite element analysis is used to predict the flux distribution and to analyse different aspects such as torque density, harmonics and mass.

Chapter 6 summarises the major findings from the undertaking, along with major contributions to research. Finally, suggestions for future work are provided.

Chapter 2

A Brief Introduction to Halbach Array

It is a general misconception that Halbach Array was invented by the Berkeley Lab Physicist Klaus Halbach. On the contrary, the Halbach Array phenomenon was first discovered over 40 years ago in 1973, by John C.Mallinson and they were called "One-Sided Fluxes". Mallinson noticed the magnetic flux produced from planar structures such as tapes, disks, demonstrated a partial ability of cancelling above the structure and summing up below, depending on the direction of rotation [27]. As limited knowledge was known of these one-sided fluxes they were originally referred to as a "Magnetic Curiosity" [27].

One-sided fluxes were shown to exist in the typical contact write and print through process in audio tape recordings and then furthermore in magnetic tape recoding [28] [29] [30] . An experiment was conducted to officially validate the existence of this type of magnetization pattern which involved subjecting a special tape wrapped around a small cylinder to a strong magnetic field [31] [32].

It was in the 1980s, the Halbach Array effect was established, named after its inventor, Klaus Halbach. Halbach arrays were first applied in insertion devices (wigglers and undulators) to focus particle beams, electrons and lasers [33]. K.Halbach went on further to design permanent magnets for use in accelerators and as sources of synchrotron radiation in electron storage rings [34]. A photo of Halbach with his colleague discussing a model is presented in Figure 2.1 and a completed prototype in Figure 2.2.

The Basic principle described by Mallinson can be seen in Figure 2.3. Restricting the problem to only two-dimensional magnetization, Figure 2.3 a and Figure 2.3 b shows two sheets magnetized longitudinally and perpendicularly respectively. Superimposing these two vectors of magnetization results in a clockwise rotation

of the magnetization as seen in Figure 2.3 c. It becomes obvious, overlaying the two magnetizations has led to a cancellation of flux above the sheet and a summation below the sheet yielding the term one-sided fluxes, where the x and y component are $\pi/2$ out phase in this case [27]. In a later paper, Mallinson offers a more generalized similarity between one-sided fluxes and a Hibert transform[1] as they both exhibit the same phase shift when considering a perpendicular pair of magnetization components [32] [35]. The magnetization vector equations for the patterns seen in Figure 2.3 can be expressed as [27];

$$\mathrm{m_x} = \mathrm{m_o} \sin(k\mathrm{x}) \tag{2.1}$$

$$\mathrm{m_y} = \mathrm{m_o} \cos(k\mathrm{x}) \tag{2.2}$$

$$\mathrm{m_z} = 0 \tag{2.3}$$

$$\mathrm{m_r} = \mathrm{m_x} + \mathrm{m_y} \tag{2.4}$$

where k is the wave number, $2\pi/\lambda$, and λ is the wavelength of the array between like poles and $\mathrm{m_o}$ is the maximum magnitude of each component.

Figure 2.1: Klaus Halbach, left shown in 1986 with Kwan-Je Kim discussing a model of an undulator designed by Halbach (Image taken from [36])

1. The Hilbert transform is simply a linear mathematical operator which shifts the phases of all frequency components by $\pi/2$

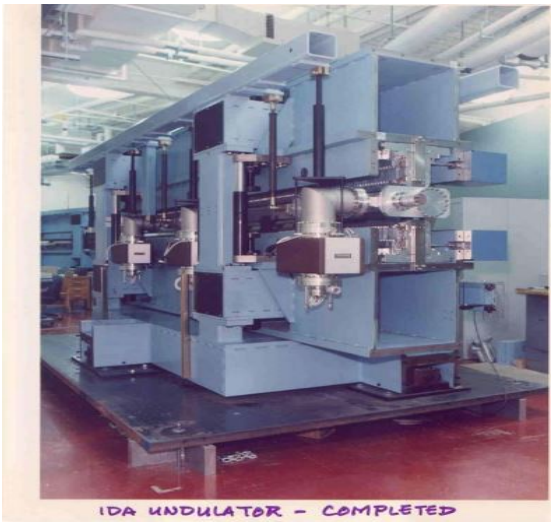

Figure 2.2: Advanced Light Source Hybrid (Permanent Magnet (PM)+Iron) Undulator 1973 (Image taken from [36])

2.1 Properties of an Ideal Halbach PM

An ideal Halbach PM yields a form of continuous magnetization which rotates as you move along the array resulting in a sinusoidal flux. As this is quite unrealistic to manufacture, especially in electrical machines of very large diameter, a reasonable approximation can be produced by assembling a desired number of discrete PMs [37]. The fields lines of the most common type of dual Halbach array (90^{o} rotation between consecutive PM segments) is presented in Figure 2.4. It demonstrates the ability of a Halbach array to be repulsive or attractive depending on the magnetic orientation. A linear comparison between a conventional arrangement of PMs and various halbach array arrangements is presented in Figure 2.5.

Below are some of the key beneficial features associated with an ideal Halbach magnetised machine:

- The distribution of the field in the air-gap is sinusoidal, which in turn reduces the stator iron loss making it suitable for application requiring high-speed and high efficiency. This is only applicable to electrical machines with an iron cored stator, this improvement is not recognised in an air cored stator. A by product of this is a more sinusoidal back electromotive force (EMF) and reduced cogging torque.
- This type of field distribution is inherently self-shielding. As described earlier, flux escapes through one end and is cancelled at the opposite end.

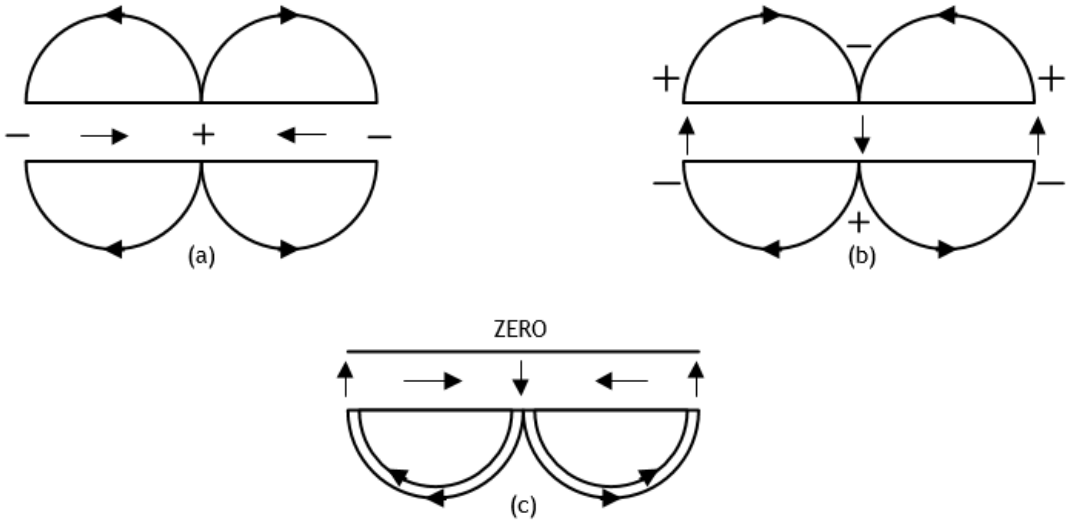

Figure 2.3: (a) Flux from horizontal magnetized sheet. (b) Flux from vertical magnetized sheet. (c) Flux from rotating vector magnetized sheet (Image modified from [27]).

Therefore, the need for magnetic rotor back iron is not essential, which not only provides a greater choice of materials for the rotor, but also leads to a reduction in rotor mass and inertia and hence better dynamic performance.

- There is no need for the use of distributed windings which is typically employed in traditional permanent magnet motors to weaken the impact of the harmonic magnetomotive force in order to arrive at a more sinusoidal back emf and to remove cogging torque. Due to its improved sinusoidal distribution of the magnetic field and less impact of the harmonic magnetic field, concentrated windings can be used in Halbach motors.
- Due to the inevitable presence of harmonics in the air gap magnetic field, skewed slots are generally used in the stator-rotor framework to weaken their impact in traditional permanent magnet motors. Due to the elevated sinusoidal distribution of air gap magnetic field and the tiny harmonic content, the stator and magnet rotor do not need skewed slots in Halbach motors. Therefore, eliminating the manufacturing costs associated with skewing [39].

The use of Halbach arrays has been documented in improving the air-gap flux density and thus the torque carrying capability (electromagnetic torque) of a Permanent Magnet Synchronous Motor (PMSM) [40] [41] [42] [43] . A more sinusoidal shape of the air-gap flux density results in a better ratio of the fundamental

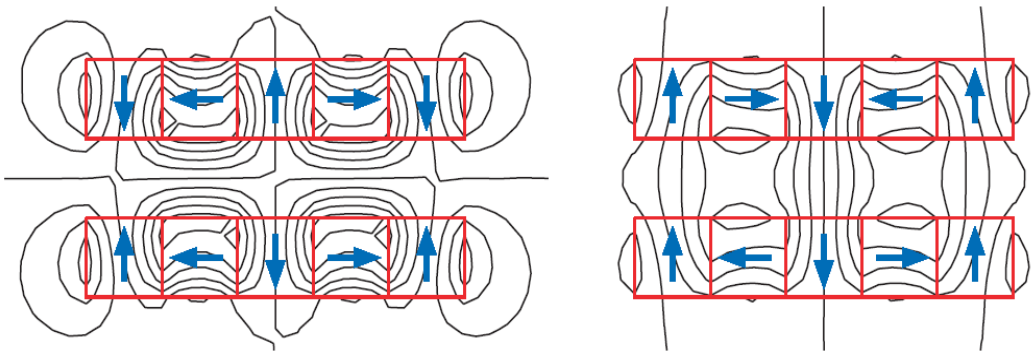

(a) In repulsion. (b) In attraction.

Figure 2.4: Linear Halbach Field lines in an arrangement of Repulsion and Attraction (Image taken from [38].)

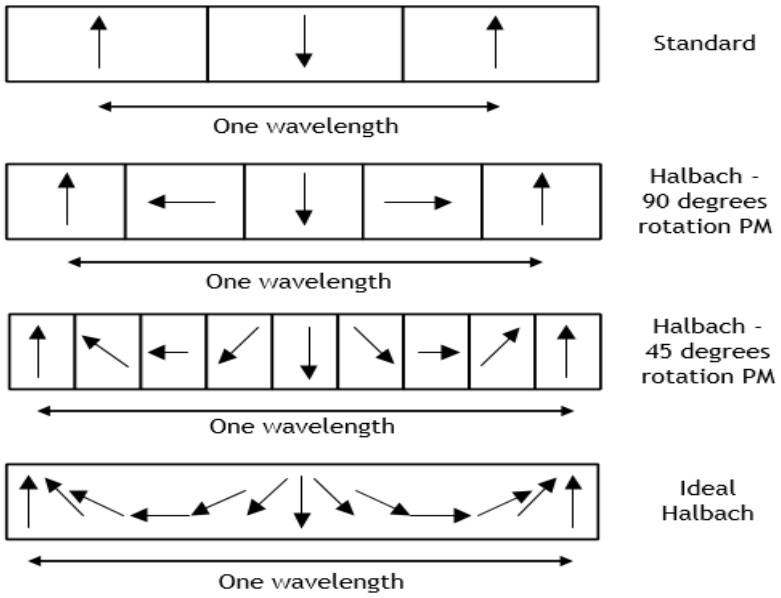

Figure 2.5: Comparison between a typical PM arrangement and various Halbach array, each of equal array length and different (Image modified from [38].)

component in relation to the overall air-gap flux, and this has been shown in various studies when adapting a Halbach configuration [44] [45] [46] [47]. As it is the fundamental component that is responsible for producing the torque, whilst the other harmonics have other effects such as stator core saturation, it is necessary to have high value of this ratio which results in better torque capability [48].

It is clear from the above, the torque/force carrying capabilities of a motor is greatly enhanced when employing Halbach arrays. However, deciding on the time and place to use this type of configuration over the conventional is important. Halbach arrays offer a more efficient use of magnetic material, but the main disadvantage lies in the increased difficulty in manufacturing and assembly which needs to be considered [49]. A complete pole in a Halbach configuration is assembled out of segments with different directions of magnetization, with each segment acting to repel each other, posing more difficult assembly procedures and reduced robustness of the rotor; do you assemble the magnets magnetised, dealing with the forces during assembly and ensuring the unit remains secure during its use?. Hence, understanding the safety factors and performing careful analyses is necessary when implementing a Halbach configuration [50]. Typically, Quasi-Halbach arrays [2] are preferred over full-Halbach arrays as they offer reduction in costs, manufacturing and assembly. Another disadvantage of Halbach arrays arises from the fact that more PM material is required which increases the mass of the electrical machine. Although, as mentioned earlier, there is minimal requirement for a magnetic material to act as a return path for flux. Thus, the rotor can be made up of low weight material such as aluminium or carbon fibre composites or a very high strength material (titanium, stainless steel) [51].

In some instances, high grade soft magnetic material can be employed in a bid to improve torque density, this works by increasing the magnetic loading limits of the machine. However, while a magnetic material will result in a stronger air-gap field, and therefore a better torque carrying capability, this comes at the cost of increase mass density and a considerably higher economic factor [45] [52].

It is important to note, each segment forming a complete pole and with different magnetization directions, is acting to demagnetise their neighbouring magnets, typically the corners [50] [53] [54] [55], even at no-load [48]. This is more of an issue

2. Quasi-Halbach arrays in this context refers to an array with fewer PMs per wavelength

in cases were quasi-halbach arrays (fewer PM pieces per wavelength) are preferred over full-Halbach arrays and can be further exacerbated when operating under elevated temperature conditions.

In light of the above mentioned issues, for an application requiring high torque density, careful comparative studies needs to be carried out to understand whether the increased performance gained by the used of the Halbach array outweighs the extra cost and weight due to the increased PM material.

As discussed and presented in later chapters, the above points to maximise the torque density performance of the machine are all taken into consideration and careful studies are carried out to confirm the validity of the Halbach array scheme. By performing this in a structured methodology, considerable improvements in terms of torque density can be achieved.

2.2 Noticeable Applications of Halbach Array

It's been nearly half a century since the discovery of one-sided fluxes now commonly referred to as Halbach array. Halbach array has seen an increasing use over this period, ranging from the most simple case such as the refrigerator magnet to more complex applications such as Maglev train track/Inductrack, which highlights its varying use and growing popularity. A review of Halbach array and its applications can be seen in Shute et al [32], Zhu et al [43] and Zhu [56]. A brief summary of these reviews is provided for completeness sake, along with other relevant studies which aided in the evolution of the proposed novel design.

2.2.1 The Refrigerator Magnet

The most simplest and widely used application of Halbach array is in the manufacture of the refrigerator magnet often found on permeable refrigerator doors which holds items such as souvenirs, pictures and drawings and so on. They appear in various shapes and sizes but the most commonly found are of a flat and rubbery nature which generally bears a printed form of advertisement on one side [57]. They are usually composed of some sort of powdered ferrite mixed in with a flexible rubber such as molten vinyl, which is rolled flat, then subjected to an alternating magnetic field giving rise to a magnetic field pattern which looks

like a row of horseshoe magnets placed side by side [57][58]. The magnetic pole arrangement of this type of Halbach array can be seen in Figure 2.6 and the magnetic flux lines and flux density plot of a Halbach array refrigerator magnet can be seen in Figure 2.7.

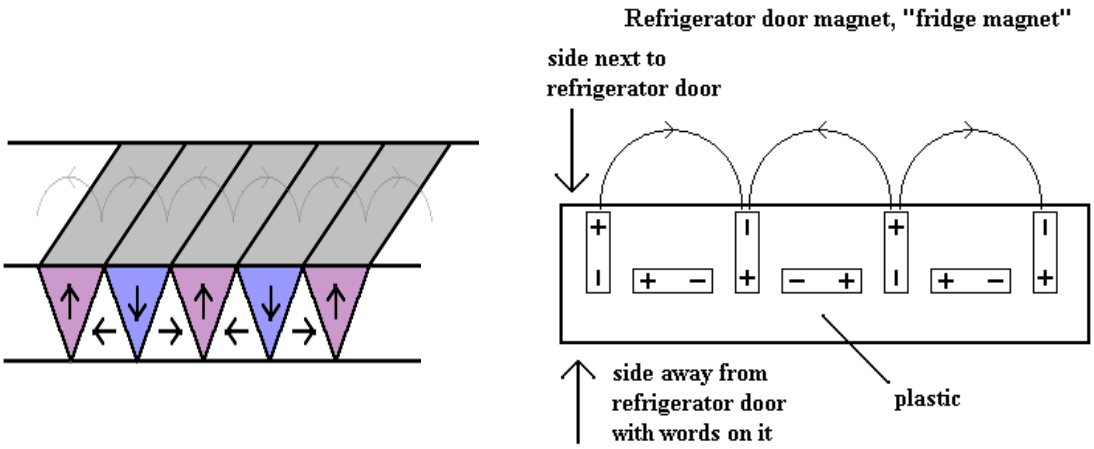

Figure 2.6: Magnetic Polarity of a refrigerator magnet (Images modified from [58] [59]).

In order to comprehend the behaviour of a Halbach array on a small scale, passing two refrigerator magnets over each other forward and backwards results in an attraction and repulsion between the two which indicates the presence of both north and south pole contained in one body [58]. The maximum flux density generally expected on the enhanced side of the refrigerator magnet is about 0.2 T with a wavelength of 0.1 cm [32].

2.2.2 Undulators and Wigglers

Undulators and wigglers are widely used in an area of applied physics called accelerator physics, in fact this was the original intended application of Klaus Halbach [33] [60] [34]. They can be found in colliders, production of synchrotron radiation (SR), free-electron lasers (FELs), and charged-particle storage rings [61]. SR is electromagnetic radiation which is produced when a beam of charged particles, most likely electrons are accelerated periodically to and fro transverse to the direction of the beam. As the electrons approach the speed of light, the radiation is bound by relativistic effects [3] to a narrow beam parallel to

3. Relativistic effect refers to the change in certain parameters of a body which is dependent on the view from the source and the observer. The object is subject to Einstein's Law of Relativity.

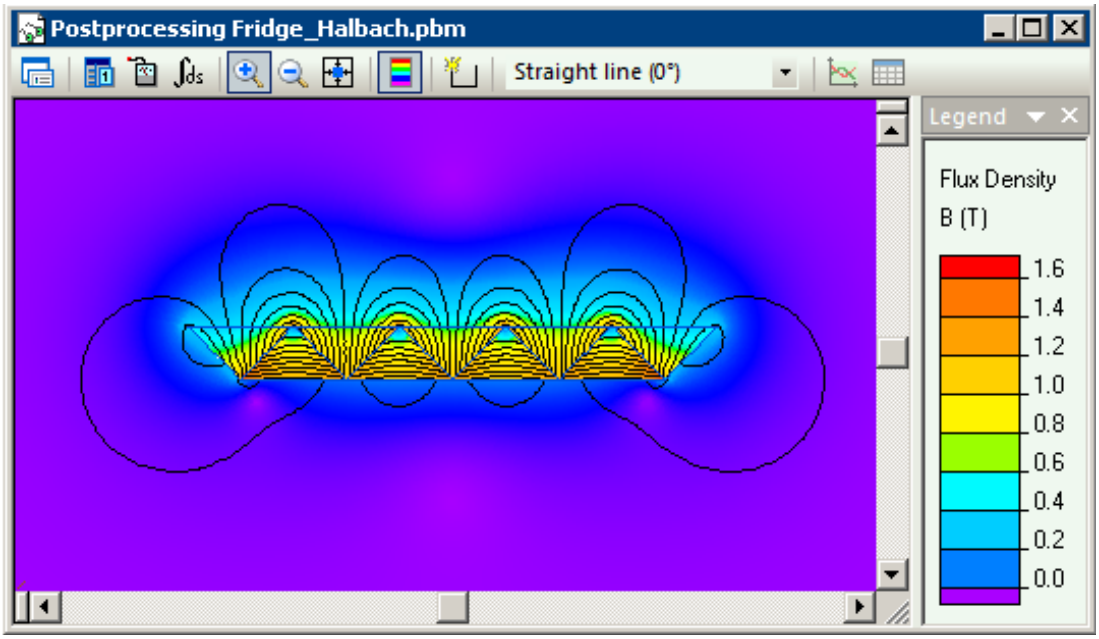

Figure 2.7: Magnetic Flux Lines and Flux Density Plot of Refrigerator Magnet (Images modified from [58] [59]).

the direction of the electrons [32]. It was in 1951, Hans Motz of the Stanford University studied the radiation generated from relativistic electrons travelling back and forth through a magnetic field of alternating polarity [62]. He quickly became a pioneer in this field and subsequently this type of magnetic system was named the undulator by Motz [61]. Typically, in FELs, there exist two linear block arrangements of PMs usually made of Neodymium Iron Boron or Samarium Cobalt PM material which produce an alternating field in the z direction causing an electron beam to wiggle transversely, under the influence of Lorentz force in x direction [32]. This can be seen in Figure 2.8, and they are often regarded as insertion devices in modern and advanced synchrotron light sources [61].

Wigglers are synonymous for undulators, as they are both insertion devices but with subtle differences. The term undulator is used when referring to an alternating magnetic structure with a long period and small bends whereas wigglers are regarded as undulators with a small number of periods and larger bends [61]. This can be observed in Figure 2.9, it is important to note the more sizeable the bend, the greater the magnetic field and power generated but this is not always the requirement. [64][65]. Originally, bending magnets were used for SR light

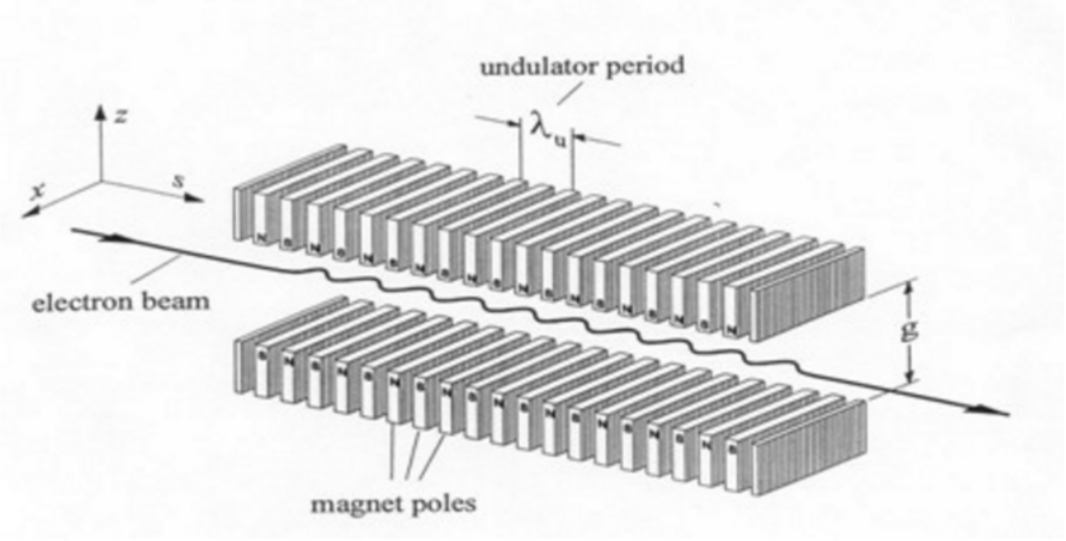

Figure 2.8: Typical Undulator Setup (Image taken from [63]).

sources as they are inexpensive and cover a broad spectrum range (microwave to x-rays) but they have limited coverage of hard x-rays [4] and are not as bright as undulators [66]. An electron beam travelling through a bending magnet can be seen in Figure 2.10 as it begins to produce a horizontal spread of SR over a wide radiation fan [65]. An illustration of a typical electromagnetic spectrum can be seen in Figure 2.11, the user can select the required wavelength for the desired experiment by adjusting the emission wavelength of the insertion devices [65].

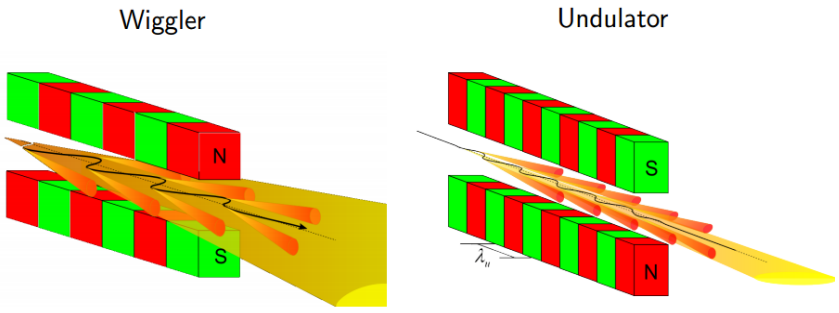

Figure 2.9: Undulator and Wiggler Bends (Image modified from [64]).

4. Hard x-rays are the highest energy x-rays, while the lower energy x-rays are referred to as soft x-rays. Hard x-rays are typically those with energies greater than around 10 keV

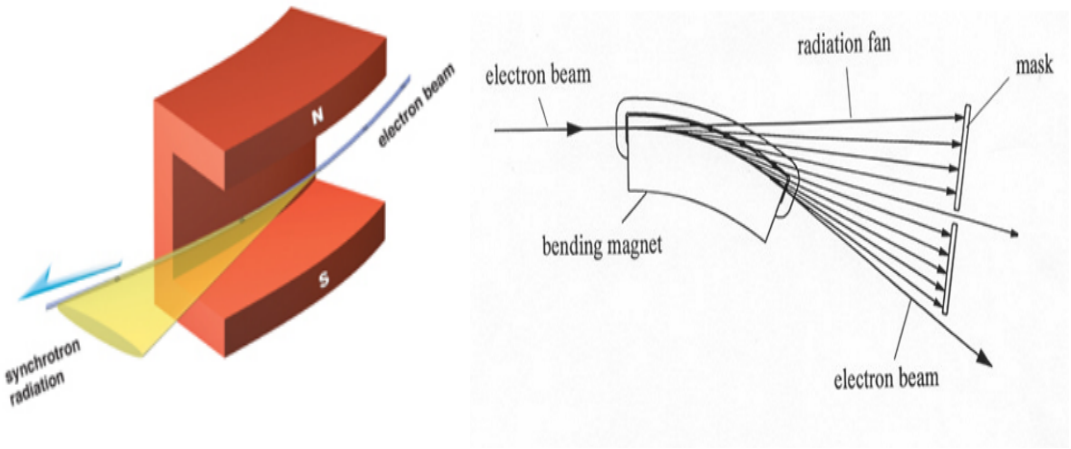

Figure 2.10: Electon Beam travelling through a Bending Magnet (Image taken from [67]).

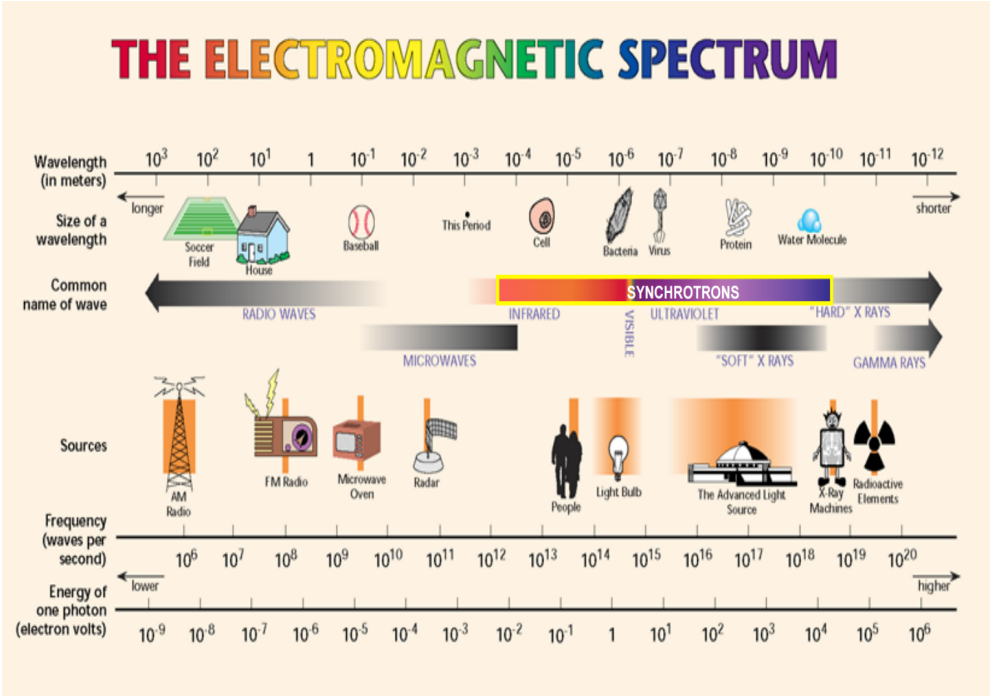

Figure 2.11: The Electromagnetic Spectrum (Image taken from [68]).

2.2.3 CSIRO Solar-Powered Electric Vehicle

One alternative to conventional drivetrains (motor, gearbox, transmission and so on) is to incorporate the motor into each individual wheel, known as an in-wheel drive system, or hub motor. This concept is not a new idea, in 1990 at the World's Fair in Paris the "System Lohner-Porsche" was debuted. The "System Lohner-Porsche" was an electric vehicle driven by two in-wheel motors; this vehicle was capable of over 35mph and set several Austrian speed records [69].

In-wheel motors offer several attractive advantages, such as elimination of drive-train losses for higher efficiency, better utilisation of space in the vehicle, and the possibility of new advanced traction control systems [70].

One of the most well-known and successful applications of in-wheel motor technology was developed by Australia's CSIRO. The design of an in-wheel electric motor for the solar powered vehicle "Aurora", was entered in the 1996, 3010 km, Darwin - Adelaide World Solar Challenge solar car race, and won and subsequently was presented in 1997 at Electrical Machines and Drives Conference (EMD97) [71].

In the world of solar cars, operating efficiency is paramount, which led to the first design decision of a PMSM. The CSIRO brushless DC motor was more efficient (97.5 percent compared to 92-95 percent) and lighter (8.3 kg compared to 12-16 kg) than all other direct-drive motors, and more efficient than all motor/gear combinations, in the race. This was achieved by the use of high flux density rare-earth magnets, and computer aided optimisation of an axial-flux configuration consisting of a Halbach magnet array and an ironless air-gap winding, completely eliminate the iron losses (eddy currents and hysteresis losses) which occur in most motors. An axial flux topology was preferred over radial flux of equivalent air-gap area, as the latter would not fit in the narrow wheel area [71] [70].

The design basically consists of two rotor rings of magnets in a Halbach Array, with copper Litz wire windings in the air-gap between them, this can be seen in Figure 2.12.

This efficient, lightweight, direct-drive, in-wheel motor, was ultimately placed in the single front wheel of the Aurora solar car. The efficiency of the motor was optimised, incorporating a mass penalty to allow for tyre rolling resistance. Cost was not considered in the design.

Based on this general topology, an optimised design was reached which featured

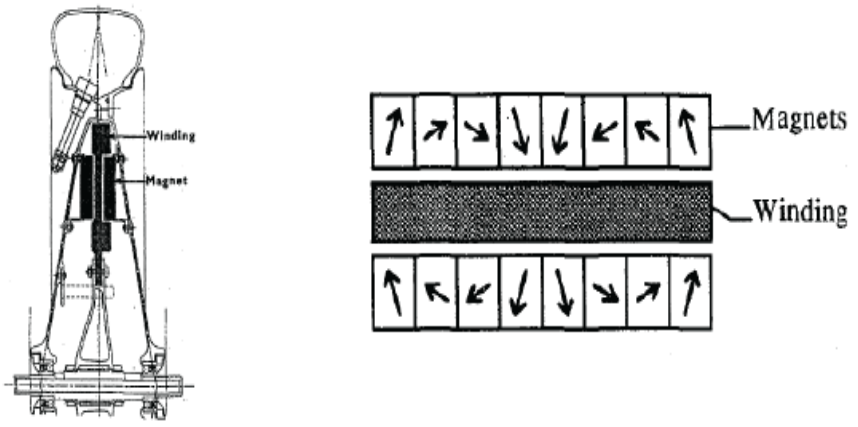

Figure 2.12: CSIRO Aurora Solar Car Topology (Image taken from [71]).

a 40-pole design, and thanks to the Halbach array managed 0.91T peak air-gap flux density.

The motor has a continuous power rating of 1.8kW, or up to 5.6kW for 72 seconds (such as for acceleration or when climbing a short hill). Continuous torque is 16.2Nm with a peak of 50.2Nm. The motor has a total active mass of 6.4kg (4.8kg of which being magnets), with a total wheel weight of 14kg.

Copper loss is identified as the main source of inefficiency in the design, and heat build up in the stator windings is the limiting factor in continuous power rating. One disadvantage identified with ironless stators is the low thermal mass, which means heat builds up quickly if the motor is used above its continuous rating.

Although the motor is extremely efficient, its power and torque density of around 0.3kW/kg and 2.5Nm/kg is not particularly impressive, and would be inadequate for either road-going cars (public road cars) or Formula SAE [5] vehicles [70][71].

5. Formula SAE is a design competition organised by the Society of Automotive Engineers (SAE) International which challenges teams of university students to construct and race Formula-style vehicles

2.2.4 High-Efficiency Electromechanical Battery (EMB)

Ambient-Temperature Passive Magnetic Bearings: Theory and Design Equations

There has been an increasing demand in today's electrified society for efficient cost-effective means for storing electrical energy. Whilst electrochemical (EC) cells in principle can address these needs, they are not without limitations. EC cells are less efficient (EMB projected to exceed 95 percent) and pose safety concerns such as the emission of hazardous gases which may be toxic when compared to EMB. The EMB is a modular unit consisting of an evacuated housing containing a modern flywheel supported by nearly frictionless magnetic bearings integrated with a special ironless generator motor. [72] [73]. The EMB works by a charging and discharging of the generator motor. The advanced design discussed by Post features a special array of PMs known as Halbach array in the generator motor to perform the actions of charging and discharging [73]. The storage of energy in a flywheel is not a new invention. The general concept was studied in the 1970s and 1980s, but with the development in strong lightweight materials, in magnetics and solid-state electronics, it has seen a significant advancement in areas such as stored energy versus weight, output power levels, energy recovery efficiency, service life, maintenance, and capital cost [72].

A detailed layout of the EMB module showing one of its more integral parts, the Halbach array can be seen in Figure 2.13. The design of the generator motor, a critical element of the EMB, has benefited greatly from the introduction of the "Halbach array" [72]. The design adopted by Post uses a dipole form of this array, used in a completely "ironless" system, to produce the rotating magnetic field that couples inductively (through a glass-ceramic vacuum barrier) to the air-cored windings of the assembly. An end view of the permanent magnet assembly, with the axes of magnetization of the individual linear magnets shown by arrows can also been seen in Figure 2.13. Also shown in the top right, is the cross section of the glass-ceramic cylinder that separates the evacuated region and the outside world, where the windings are located. On the same figure is shown the results of a computer-code calculation of the field lines produced by the Halbach array. As is evident, not only is a very uniform dipole field created inside, but there is a high degree of cancellation of the field external to the magnets. The dipole version of Halbach's magnet arrangement has been chosen so as to make the inductive coupling between the magnets and the windings relatively insensitive to the radial

gap between them, thus easing the mechanical clearance problem considerably. [72]

The efficiency and power density of this generator motor was computed and was found to be far higher than conventional generators and motors [72]. Although, as the rotor is slowed down during discharge, the voltage output will invariably drop which leads to a drop in the efficiency at constant power output. For example, as stated by Post, at the one-half-speed point (three-fourths discharged) the copper losses at a power output of 5.5 kW will rise to about 25 W, and the efficiency will have correspondingly fallen to 0.9954 per unit, which is still a very high value. Regarding the power needed for a vehicle, a combination of 25 of these modules with a power output of 5.5 kW per module corresponds to an available power of 137.5 kW, or about 180 hp [72].

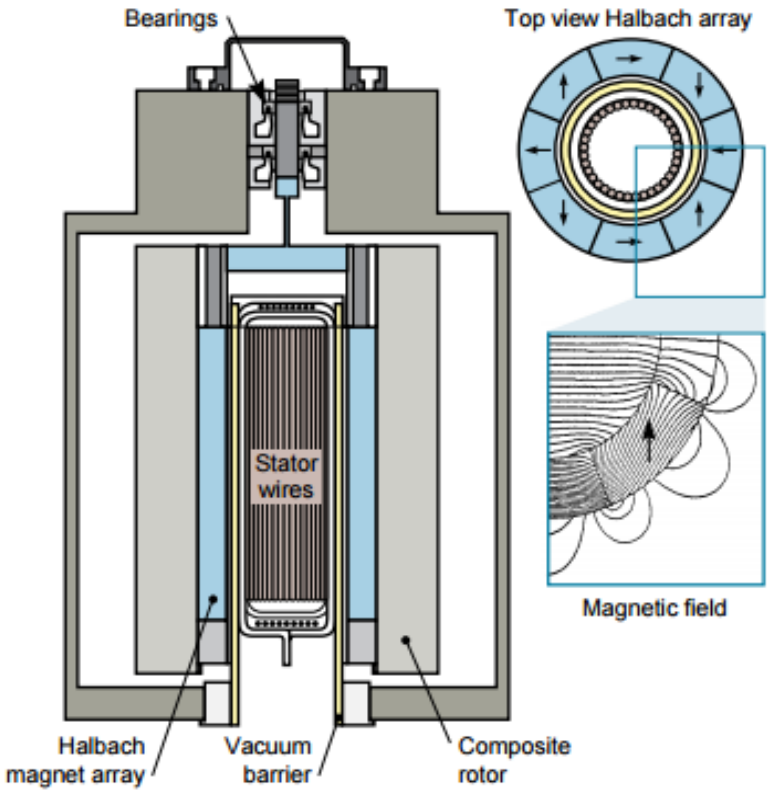

Figure 2.13: Detailed Layout of EMB incorporating (Image taken from [73]).

2.2.5 Permanent Magnetic Bearings

The advent of high-energy product PM materials has led to investigations into magnetic bearings for applications from turbo machines to flywheels for energy storage. Bearing longevity is an issue that can be solved with PM magnetic bearings in tiny high-speed turbo compressors. In space instrument applications, magnetic bearings eliminate the need for lubricants that can contaminate optical surfaces; and in flywheels for energy storage, PM magnetic bearings enable vacuum operation [74]. Magnetic bearings can be grouped into two categories; active or passive. Actively-controlled magnetic bearings are commonly used in industry for rotor levitation in supporting large load. They have attractive features such as stiffness and damping, and dynamic control compared to passive magnetic bearings. Although, they require very complicated and expensive power electronics such as digital signal processors, amplifiers, digital-to-analog converters, analog-to-digital converters, and software. On the other side, passive magnetic bearings do not need this hardware. They can be produced smaller, they are more reliable and more efficient and they provide larger rotor-stator gap [75]. The disadvantages of passive magnetic bearings are; they typically have less stiffness and damping than active magnetic bearings of similar size, and implementation of vibration control is not possible [76].

The NASA John H. Glenn Research Center has a great deal of experience in Halbach array technology specifically for high-speed spacecraft applications. The goals of its Fundamental Aeronautics Program include improving efficiency, reliability and safety [77]. Two types of non-contact bearings were investigated; Axial and Radial Halbach magnetic bearings. A Halbach magnetic bearing has the capacity to produce four times as much force as a conventional magnetic bearings with similar volume, making it very attractive [78]. Both types of NASA magnetic bearings are passive, in that there is no need for complex active control to achieve effective magnetic levitation. Magnetic levitation is achieved by repulsive electromagnetic force between the moving Halbach permanent magnet array and an induced electric current in stationary coils as a result of the motion of the magnetic field. This is depicted in Figure 2.14 and a simple view of the rotor and stator in both bearing types can been seen in Figure 2.15 and Figure 2.16 [79] [80].

A number of radial Halbach magnetic bearings ranging from half inch long to twenty inch in rotor diameter and an axial version of 4.7 inch in rotor diameter

were developed and tested under the Fundamental Aeronautics Program. In each case, magnetic levitation was achieved albeit for a short period. The combined impact of temperature rise and skin effect at higher speeds weaken the current and hence the lifting force [81] [82]. Although, for large machines of diameter greater than 1m, the factors limiting the bearings performance improves significantly. There is less resistive heating and the bigger size provides more thermal mass and more surface area from which heat can dissipate [81] [82].

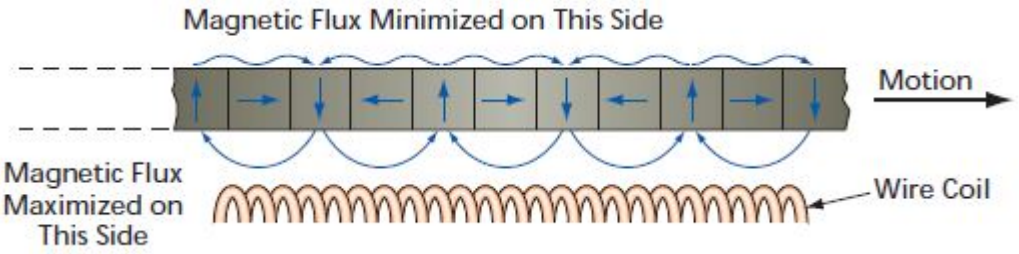

Figure 2.14: A Basic Halbach Array Levitation (Image taken from [79]).

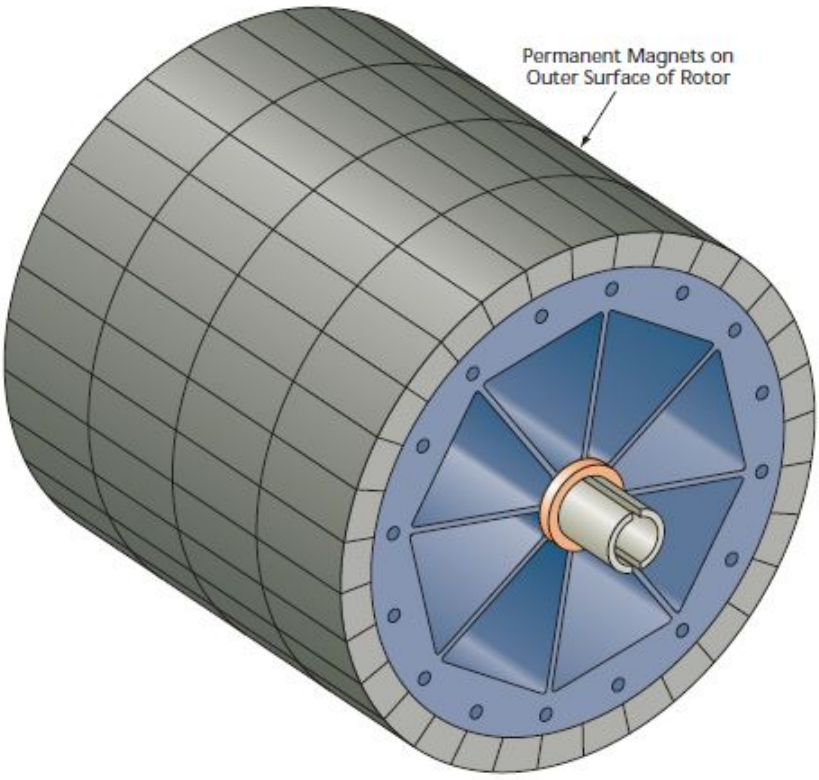

Figure 2.15: The Rotor in a Radial Halbach Magnetic Bearing (NASA) (Image taken from [80])

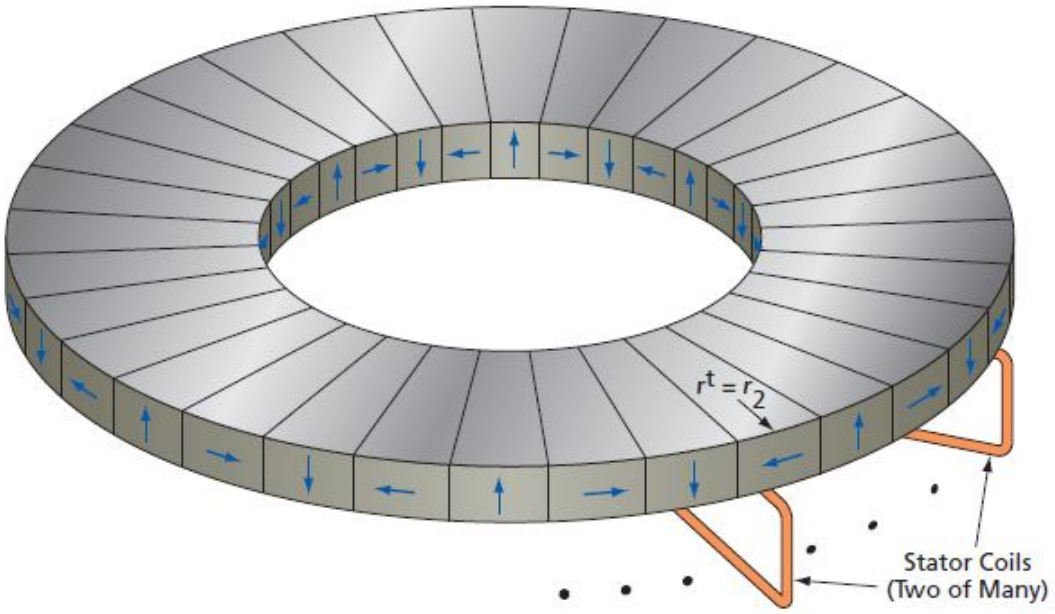

Figure 2.16: The Rotor in a Axial Halbach Magnetic Bearing (NASA) (Image taken from [79]

2.3 Conclusion

This chapter provides a background introducing Halbach array, its properties, benefits and drawbacks. A generator employing Halbach array leads to a more sinusoidal and higher flux density in the air-gap compared to a conventional permanent magnet generator, this is one of the most key features of a Halbach array and the most focused on during this research. All the other features are a by-product. Although, this benefit is not always the case and this is described in the next chapter with techniques to curtail this. There are multiple combination of angles to produce a Halbach array, generally the more blocks you have in one wavelength, which is analogous to having a smaller angle of rotation, the more homogeneous and stronger the field output, which in turn results in an improved efficiency. This is not always the case, in reality performance of Halbach arrays involves the combination of many variables such as magnet size and shape, temperature conditions and environment.

Furthermore, we saw the various applications of Halbach array, these range from industrial servo, automotive, aerospace to household appliances, as well as gen-

erators for wind turbines. Halbach arrays are gaining more and more traction but the fact still remains as with any developing technology, it is not without challenges and issues some of which were detailed in this chapter, nonetheless it offers very many advantages which require further investigation.

Chapter 3

History of C-GEN Topology

C-GEN technology is a novel multi-stage air-cored electrical PM generator that is applicable to direct drive, slow or medium speed generator design [83]. A patented C-GEN topology was developed in 2005 by Professor Markus Mueller and Dr Alasdair Mcdonald in the School of Engineering within the Institute for Energy Systems at the University of Edinburgh, in order to address the challenges of using conventional generator technology in direct-drive renewable energy systems for wind, wave and tidal energy. In its simplest form the C-GEN technology is based on a steel C-core and permanent magnets, as shown in Figure 3.1 [19].

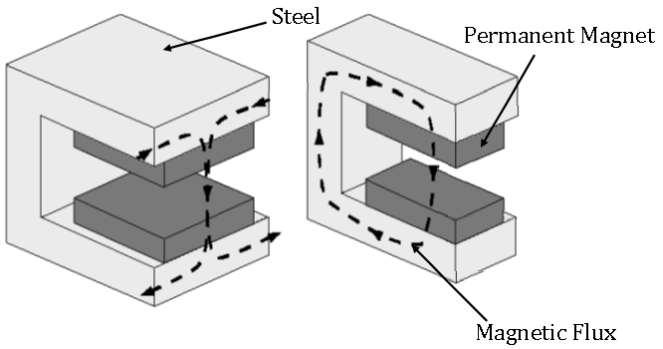

Figure 3.1: Steel C-core with permanent magnets (smallest C-GEN module) showing Longitudinal (left) and Transverse (Right) Flux Path (Image modified from [84])

In a conventional PM machine steel exists in the rotor, and the coils are embedded in a steel structure, so that significant magnetic attraction forces exist. In order to overcome these attraction forces and maintain a small physical clearance between moving and stationary sections a very large structure is required, which accounts for more than 60% of the total mass in a direct-drive generator [18].

The innovation in C-GEN lies in the use of a PM C-core arrangement and air-cored coils. An air-cored coil contains no steel so that when it is inserted into the C-core, there are no magnetic attraction forces. Hence the support structure for

the generator only needs to support the mass of the C-cores and coils, and does not have to overcome any magnetic attraction forces [19]. A rotor assembly consists of a number of C-cores mounted circumferentially as illustrated in Figure 3.2. By mounting the PMs onto the C-core, the attraction forces are reacted by the C-core structure rather than at the shaft several metres away.

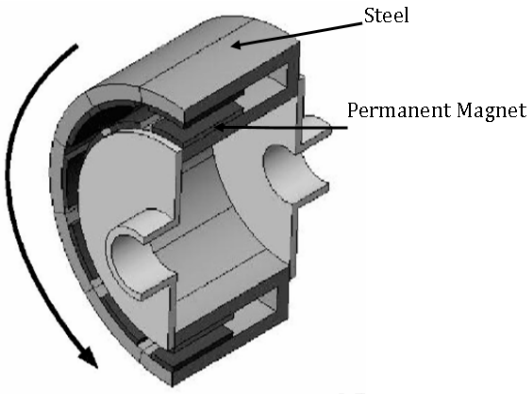

Figure 3.2: Cross section of a C-GEN rotor made up of C-cores

C-GEN technology can be used as radial-flux, axial-flux and stacked multi-stage generators. Figure 3.3 shows examples of various types of C-GEN generators mounted at the same radius. Different applications with different weight or size sensitivities mean different C-GEN types are optimal. Stacked multi-stage axial-flux C-GEN machines have the advantage that the same fundamental C-GEN unit can be replicated, the number of units varied for different torque/power levels [84]. In the linear form, the C-GEN can be used in wave energy devices taking advantage of the up and down nature of wave energy [85].

The following key unique selling points (USPs) over existing generator technologies used for direct-drive in terms of Design and Operation, Factory to Installation and Operation and Maintenance (O&M) can be seen below and is illustrated in Figure 3.4 [86]:

- No magnetic attraction forces closing the air gap: In C-GEN the electrical coils are wrapped around materials which have the same magnetic properties as air. Although this means that the magnetic field is slightly weaker than conventional machines, it also means that there are no forces trying to close the gap between the rotating and the stationary parts. Furthermore, the magnetic forces between PMs and steel are eliminated due to the novel arrangement of magnets and steel. This simplifies the support structure

required, making modules safer to handle, which has positive benefits in terms of manufacturing and transportation.

- No cogging torque: In a conventional permanent magnet machine the magnets try to align themselves with steel teeth on the stationary part of the generator. Torque, known as cogging torque, is required to overcome this alignment force. This tends to increase the cut-in wind speed (the minimum speed at which the turbine produces power) and is also a source of vibration in the generator. C-GEN technology has no cogging torque to overcome.
- High Degree of Modularity: The C-GEN generator can be built of a number of small modules due to the high degree of modularity in both the stator and rotor. This helps reduce the manufacturing costs in terms of reduced size of components, ability to outsource manufacturing of modules and repeatability of manufacturing steps.
- Higher availability: Due to the high degree of modularity, the C-GEN is a multi-stage machine, which means a completed generator can be built of a number of smaller generators. For instance, a 4 stage 1MW generator consists of 4 separate 250 kW machines, all of which can be isolated. This property of stacking provides the benefits of redundancy and robustness. If there is a fault in one of the stacked generators, that machine can be isolated, and the turbine can continue to generate and hence gain revenue until a suitable O&M window is available. Bear in mind, stacking is only possible due to the modularity of the machine which is inherent of the C-GEN technology.
- Ease of O&M: The high degree of modularity enables replacement of single faulty modules rather than the complete machine. This reduces O&M costs and increases the turnaround of any O&M procedures. Depending upon the size of the device, the O&M procedure could be done on board a ship using an on-board crane. Modules can be designed to have a mass typical of craneage on a ship.
- Reduced cost of installation: In any installation, cranes are required to lift the nacelle to the top of the tower, and this lifting equipment is rated according to the heaviest component in the nacelle, which is most likely to be the direct-drive generator. The lightweight and modular C-GEN enables the crane to have a lower rating – depending on the assembly option this could be the mass of the generator or the biggest module.

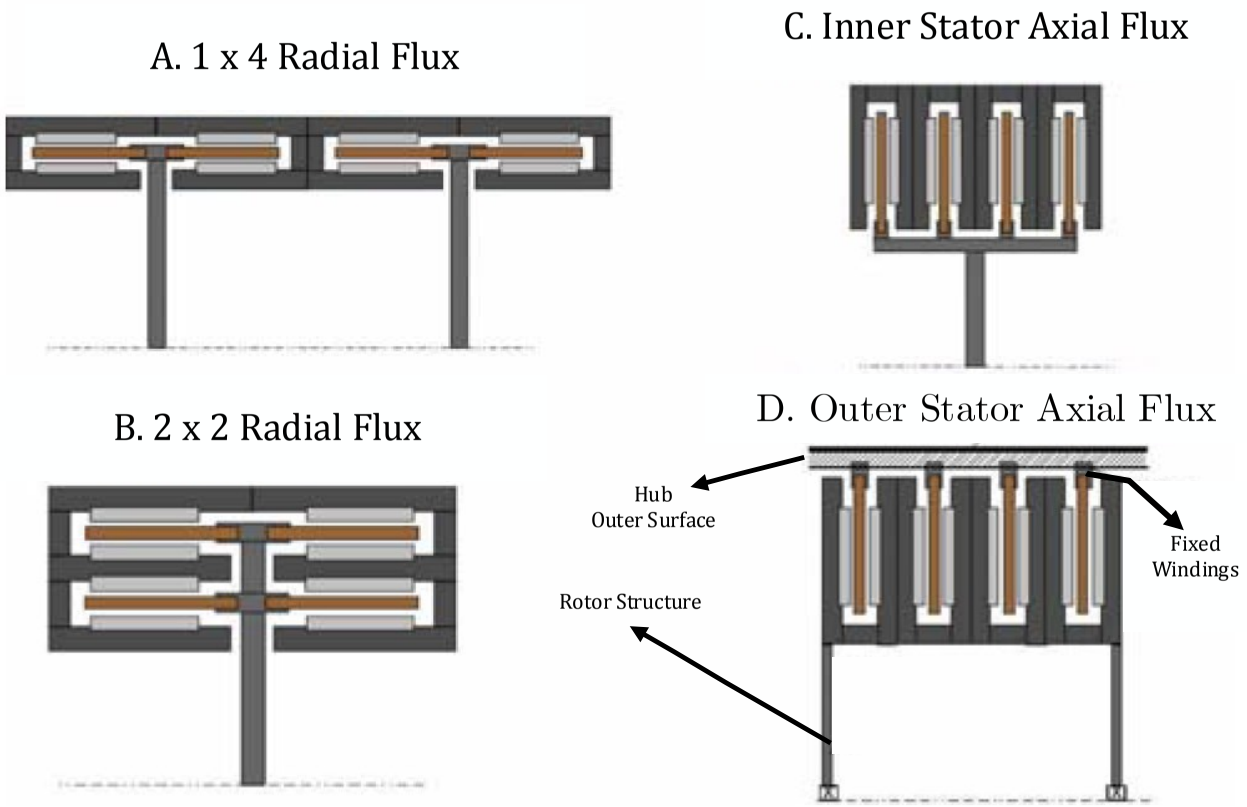

Figure 3.3: Multi-stage topology options (Image modified from [87])

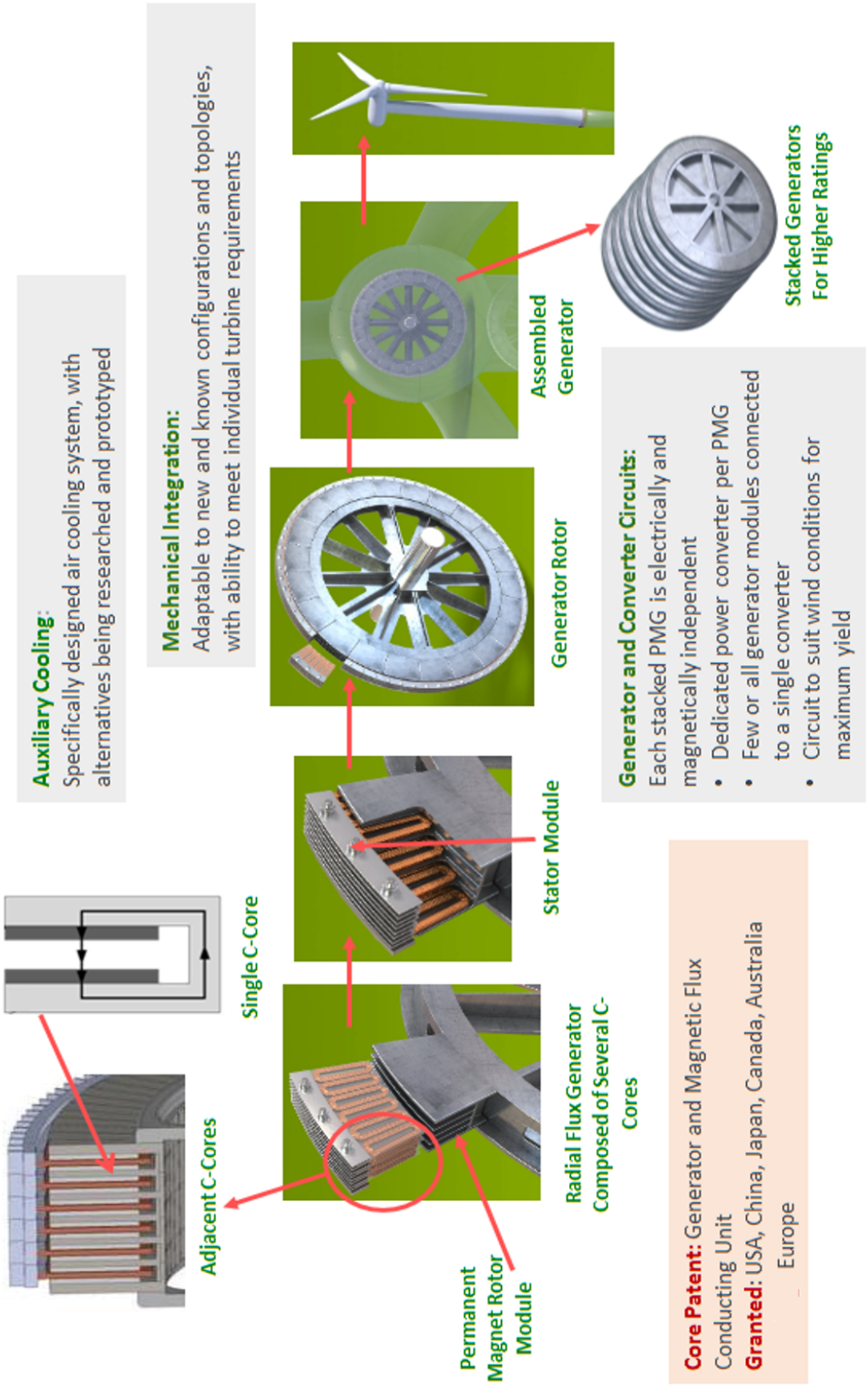

Figure 3.4: Summary of USPs of C-GEN (Image taken from [88])

3.1 C-GEN Prototype Demonstrators

The development of C-GEN prototype demonstrators aims to design a generator topology that specifically meets the requirements for direct-drive renewable systems (wind, wave and tidal stream). The following objective were established [86]:

- To prove the fundamental engineering principles.
- To verify design tools and procedures.
- To demonstrate manufacture and assembly techniques.
- To show high level of performance in terms of efficiency.
- To build confidence in developing a 1MW demonstrator.

3.1.1 What is the Design Tool?

An in-house electromagnetic design tool based on analytical equations with a link to finite element analysis and CAD has been advanced and verified during the course of the projects discussed in the following sections. The design tool fully integrates the electro-magnetic, thermal and structural aspects of the generator.

The tool allows the electrical machine designer to compare various critical design parameters and optimize the performance using parameters such as efficiency, cost and so on [18].

A number of prototypes ranging in scale from 15 kW to 1 MW, have been shown to validate the scientific concept, including a model of a 50 kW prototype for wave energy applications. All of which have taken place in the lab, with experiments in realistic environments. Most recently, testing of a 150 kW C-GEN linear machine funded by the Wave Energy Scotland (WES) is ongoing, with the potential to take the technology from Technology Readiness Level (TRL) 4 to TRL 5-6 which will demonstrate that C-GEN can satisfy the requirements for operation under a harsh environment [89]. A brief description of the stages in the C-GEN history is given below: The following sections is not of the author's own work rather they are integral to

3.1.2 Scottish Enterprise (SE)

The C-GEN generator was developed by the University of Edinburgh under the Scottish Enterprise Proof of Concept (PoC) Programme. In this stage the concept was proven at scales of 20 kW (100 rpm) and 15 kW (150 rpm). Both prototypes were built by Fountain Design Ltd and subsequently tested at the University of Edinburgh. The 15 kW machine was also demonstrated on a commercially available wind turbine. The design tools developed were validated with experimental results from the two prototypes. The modularity and ease of manufacture of the technology were key outcomes from this stage. Results from these projects can be seen in [19] [90].

3.1.3 SMART Award

On the success of the SE PoC, Prof. Mueller founded a spin-out company, NGenTec Ltd, with colleague Dr. Alasdair McDonald in 2009 to commercialise C-GEN technology. An exclusive royalty free license was signed in November 2009 covering all patents filed, know-how, design tools developed and access to all prototypes built [**?**]. In this stage, the previous concept was further developed into a 25 kW, 100 rpm multi-stage axial flux machine, which would be scaled up to 1 MW.

Further validation of design tools was achieved using experimental results from the machine and new manufacturing and assembly techniques were demonstrated, which are applicable to up-scaling to multi-MW levels [84]. The thermal performance was also investigated and in particular a novel passive cooling system. The 25 kW demonstrator was tested at the University of Edinburgh [91].

3.1.4 Department of Energy & Climate Change (DECC) Grant

NGenTec secured inward investment of £2 million from Amsterdam based SET Venture Partners and SE's Scottish Co-investment Fund (SCF) which enabled the company to demonstrate the C-GEN technology on a multi-megawatt scale [92]. NGenTec worked very closely with David Brown on the testing and validation of the generator technology [93].

A 1 MW test rig was designed, built and tested by David Brown Gears at their development facility in Huddersfield. The 1 MW prototype was designed to operate at the equivalent of a 6 MW machine, demonstrating 1/6 th of a

6 MW generator [87]. Thus this demonstrator showed that this technology can easily be scaled from tens of kW up to multi-MW in one single step.

Unfortunately, NGenTec ceased trading in 2013, but all the Intellectual Property was passed back to the University of Edinburgh for continuous development.

3.1.5 Carbon Trust Marine Accelerator Programme

In order to explore the C-GEN for wave energy applications, funding was obtained under the Carbon Trust Marine Accelerator Programme and a 50 kW (peak), 1m/s linear generator, weighing in the region of 1.6 tons was built and tested to prove the concept and the analytical models. The verification of the thermal and electromagnetic models is discussed in [85] and the no-load- and load-test results are presented in [94].

3.1.6 Engineering and Physical Sciences Research Council (EPSRC)

In October 2016, Swift TG Energy (Scotland) Limited was awarded a grant for the value of £200k under the supervision of Dr Jonathan Shek, to build a self-starting, active-pitch, vertical-axis wind turbine, WindSurf, to tackle the challenges of inefficient wind capture in urban areas.

Typically, the nature of the wind is more turbulent and swirling near urban areas, which makes traditionally designed wind turbines undesirable as they are more efficient in locations where there is a steady, uninterrupted flow of air. The Swift project presents a novel patented control technology, which continually varies blade pitch, allowing a self-start in wind speeds as low as 3 m/s, leading to better energy capture in urban sites. These areas have the added benefit of being closer to the consumer and therefore, results in reduced transmission losses.

A 16 kW 2-stage electrical generator was developed for WindSurf based on the C-GEN direct-drive technology which resulted in reduced cost and improved performance. Although, the generator designed and built as part of this project is for wind turbines, the design and techniques used can be applied to other sectors [95].

3.1.7 Wave Energy Scotland (WES) Project Neptune

The success of the Carbon Trust Programme led to future funding from WES in 2015 as part of its Novel PTO call to focus on critical components, the windings and bearings. In May 2017, Professor Markus Mueller was awarded £2.5 million by WES as part of the Stage 3 PTO call, with the aim to demonstrate the C-GEN technology at a relevant scale, in this case a 150 kW linear machine and under real marine conditions. Project Neptune is the current main project to develop C-GEN for the wave energy sector [83].

3.1.8 Mocean Energy

Mocean Energy WEC is a hinged rafting device. The dynamic response of the two bodies of the raft to the wave's forces leads to a flexing motion over the hinge that drives a mechanism for power take-off (PTO), which converts kinetic energy into electricity [96].

Mocean Energy received £3.3 million from Wave Energy Scotland (WES) to develop and build a scaled prototype of their Blue Horizon wave machine and the start-up company has chosen C-GEN technology to provide its PTO stating:

> "*Blue Horizon is a hinged raft with a unique geometry which flexes in two dimensions via a relatively slow-moving single hinge. C-GEN is a good match for us because it delivers high efficiencies in the right range of speeds.*"
>
> —Cameron McNatt (Mocean Energy Managing Director)

Both teams will now build a test rig, of a 10 kW two stage rotary machine, which will be tested at Supply Design, a specialist power electronics developer in Rosyth, where the C-GEN PTO will undergo performance and acceptance testing using representative wave data. The same PTO will then be installed in Mocean Energy's half-scale prototype which will be manufactured and deployed at the European Marine Energy Centre in Orkney in 2020 [97].

The success of this programme, will potentially result in the industrialisation of C-GEN for marine renewable applications and demonstrate C-GEN in a real environment and under realistic conditions.

Due to the availability of experimental results provided by the University of Edinburgh, which will form the basis of the analysis in the following chapters and the appealing nature of the axial flux multi-stage topology over radial flux

multi-stage, the next section will focus on the experimental results for the 25 kW and 1 MW Axial Flux generator.

3.2 SMART Key Axial 25 kW Results

In order to scale up the technology from 20kW to MW scaled, NGenTec in partnership with the University of Edinburgh decided that the axial flux topology provided more benefits compared to the radial flux topology of the 20 and 15kW prototypes, this is well documented in [87]. Hence, a further prototype was built to verify various design and manufacturing aspects that would be implemented in a MW scale demonstrator.

In a radial flux machine the coils are supported at one end and hence there is a limit to how far one can cantilever the coils. The radial topology does not lend itself to a high degree of modularity.

In the axial case the coils are supported vertically and hence there is no issue in terms of supporting a cantilevered structure. Modularity in the axial direction also enables stacking of generators making it more flexible than in the radial case.

The following aims were set out and fulfilled [88] :

- Can we build an axial-flux version ?
- Can we build a multi-stage version ?
- Can we build a modular version ?
- Can we cast rotor modules ?

The axial flux machine is modular on both the stator and rotor as can be seen in Figure 3.5 in which the stator and rotor have been partially assembled to illustrate the modularity aspect. The rotor modules on the left are simply cast sections including all 3 stages within one cast module. Casting modules in this way is very cheap.

Figure 3.6 shows the main features of the axial flux multi-stage machine. For the 25 kW prototype only 8 cast rotor modules are required leading to a reduction in the part count. The stator can only be modularised within a stage and not across stages as in the case of the rotor. Each stator module consists of a single blade potted in epoxy which contains 3 coils, one for each phase for the 25kW prototype. For each stage of the 25 kW machine there exists 8 such stator modules.

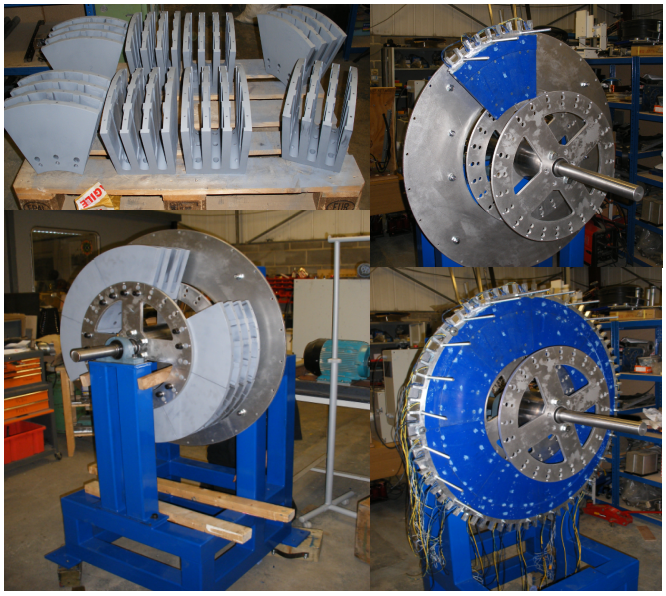

Figure 3.5: Modularity assembly of C-core rotor (Left) and air-cored stator (Right) (Image modified from [88]

Figure 3.6 also shows the complete machine installed on a test rig at the University of Edinburgh, but with only one stator stage installed. The other two stator stages were installed in-situ on the test rig to demonstrate the ease of assembly due to the lack of magnetic attraction forces between the stator and rotor. Subsequently it was found that two stator modules in one of the stages had to be replaced, which was done by hand [84]. Thus, demonstrating one of the USPs of this machine.

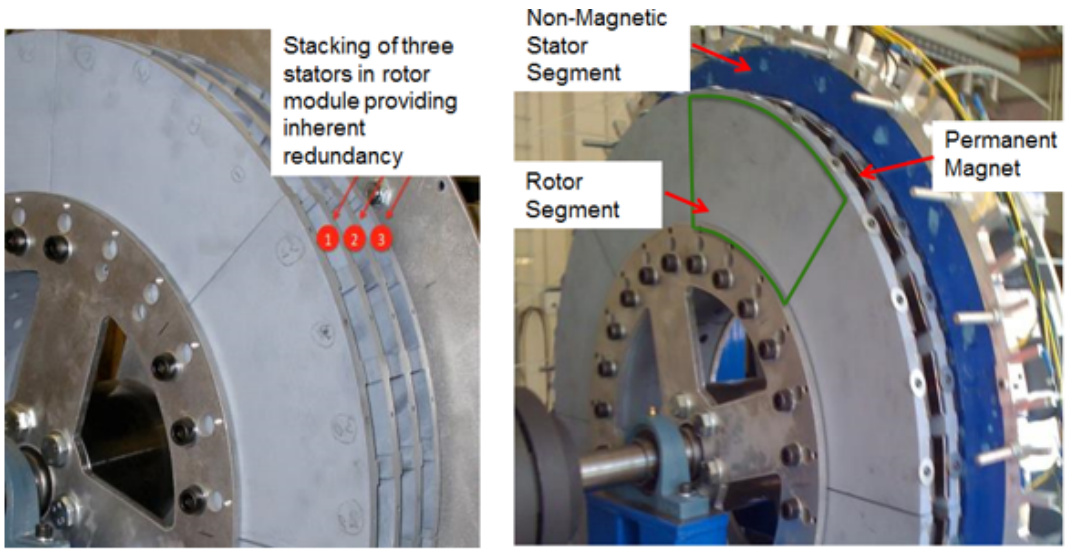

Figure 3.6: 3-stage axial flux arrangement with coil modules sandwiched between PM rotor plates (Image taken from [88])

The 25 kW axial flux 3-stage machine was designed using the design tool developed in the SE Proof of Concept Project, with the main output parameters listed in Table 3.1, along with measured values, which clearly show good correlation with the design results.

Parameter	Design	Measured	Units
Nominal Speed	100	100	rpm
$B_{gap}(FluxDensity)$	0.54	0.54	T
$V_{no\,load}$	298.5	299.8	rms
V_{load}	270.4	276.9	rms
I_{load}	10.4	9.8	rms
$P_{out}(W/Stage)$	8472	8126	W

Table 3.1: Basic Specification for the 25 kW prototype at full load (Table adapted from [84])

The thermal performance was investigated in [98], the authors compare experimental measurements against the results predicted using Computational Fluid Dynamics (CFD) methods. Figure 3.7 shows the regions of the coil surface used for measuring the temperature rise and the machine is ventilated through axial and radial air inlet holes present in the rotor structure as depicted in Figure 3.8. The temperature distribution of a CFD analysis with radial and axial hole ventilation can be seen in Figure 3.9 which was conducted along with other cases to demonstrate the importance of the right inlet configuration.

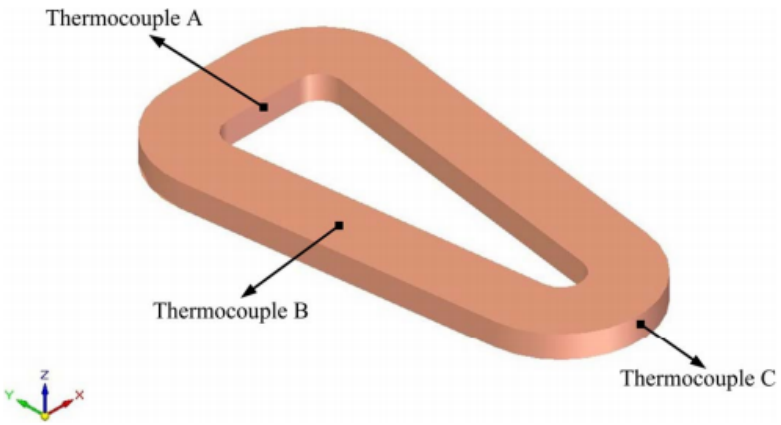

Figure 3.7: Thermocouple Locations on the stator coil (Image taken from [98])

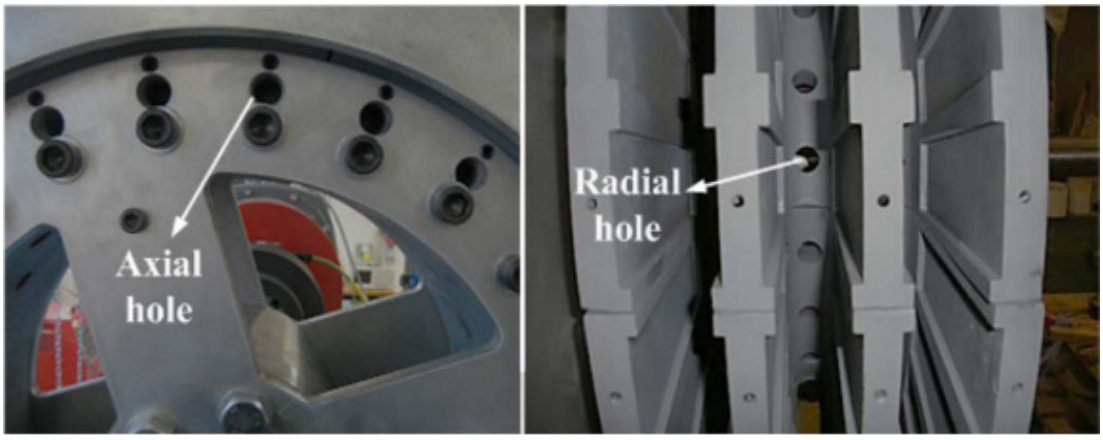

Figure 3.8: Ventilation Holes (Image taken from [98])

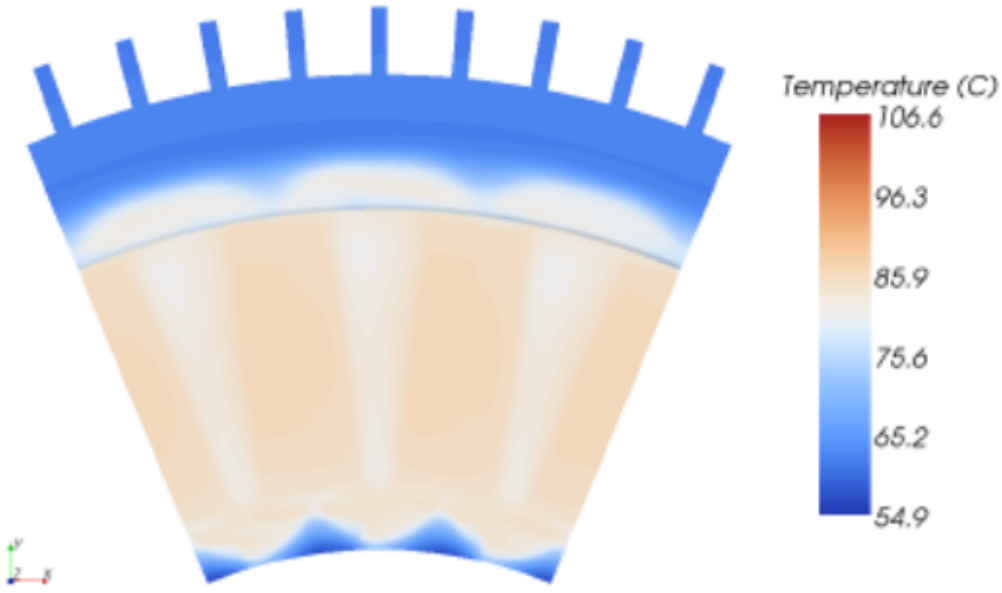

Figure 3.9: Temperature contour of the stator surface for a specific CFD analysis (Image taken from [98])

A comparison of experimental and simulated results is summarised in Table 3.2. The power losses in the CFD analysis was assumed to be uniformly distributed throughout the volumes of the machine parts and limitations of modelling techniques led to the discrepancies observed [98]. Nonetheless, there is still a good agreement between the measurements and simulation results.

The outcomes of this project de-risked the scaling up of the technology to MW level, by further validating design tools, demonstrating fabrication of stator coil modules, demonstrating a novel passive cooling system [91], and module replacement techniques.

Temperature Rise	Experimental Measurements	CFD Simulation
Thermocouple A	52.6°C	54.1°C
Thermocouple B	58.2°C	57.0°C
Thermocouple C	35.6°C	42.3°C

Table 3.2: Comparison of Experimental and CFD Simulated Temperature Rise (Axial and Radial Holes) (Adopted from [98][91])

3.3 DECC Key Axial Flux 1 MW Results

The DECC demonstration project builds upon the SMART project in that the generator technology is scaled up to 1MW, but rotating at the speed of a 6MW machine, 12rpm. The concept is the same as the 25kW machine, but the diameter is now 6.4m rather than 1.2m [87]. The authors used the design tools developed in the previous stages to provide the electromagnetic design of the machine. Due to the nature of the scale, a more detailed structural and thermal design was performed. NGenTec collaborated with Motor Design Ltd to enhance the thermal models, which were further verified experimentally. The DECC project proved that C-GEN technology can be scaled up to the MW scale, giving confidence that this technology will be able to provide a step advance in generator technology for the offshore wind sector.

Below are the key technical characteristics of this generator [88] and an overview of the 1 MW assembly is shown in Figure 3.10:

- Four equal stages (250 kW): any combination of stages can be satisfactory run (One Two, Three or Four stages)
- Output Voltage = 690 V_{rms}
- Speed circa. 12 rpm
- Single stack of potential 6 MW machine
- Insulation/ Temperature rise Class F

3.3.1 1 MW Prototype Detailed Test Results

Prior to the development of the 1 MW prototype, a test rig of a full scale module (See Figure 3.11) was built and tested to validate the thermal and CFD modelling. Figure 3.12 shows CFD plots of the temperature rise on the module surface and within the coils. The maximum coil temperature for 51 kW electrical losses (expected Joule losses at rated load) from experimentation is 60°C and from CFD it is 64°C as reported in [87]. This shows a good correlation between the measurement results and numerical analysis, giving further confidence in the CFD modelling and adopted design practices.

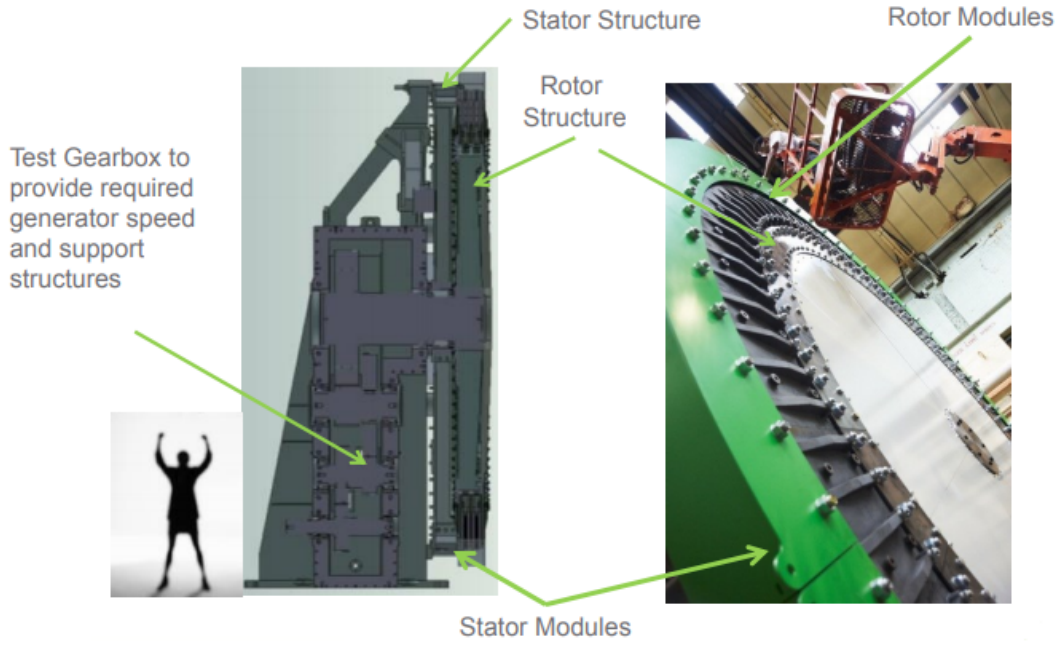

Figure 3.10: Overview of C-GEN 1 MW Prototype (Image taken from [88])

Figure 3.11: Test Module with fan casing (Image taken from [87])

The open circuit voltage is an important parameter in generator design, as it is the measure of the electromotive force (EMF) of the generator. This was measured

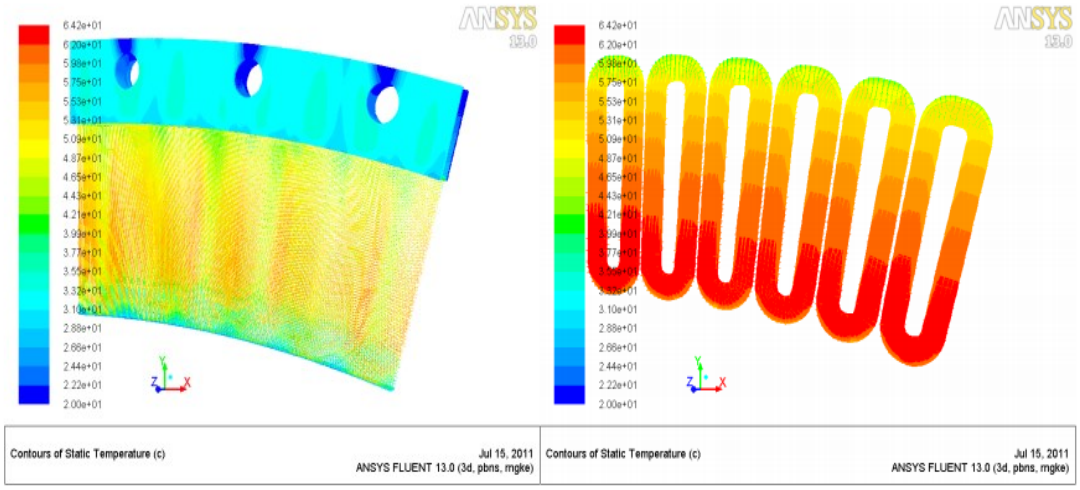

Figure 3.12: CFD Thermal Modelling (Image taken from [87])

across a number of stages on different days and the open circuit voltage against speed was plotted as seen in Figure 3.13. It is perfectly linear with no saturation effect, voltage is proportional to speed [88].

Another important performance feature of any electrical machine is the efficiency characteristic, especially for a large multi-megawatt generator designed for continuous operation. Figure 3.14 shows a comparison between measured and calculated efficiency at 25, 50, 75 and 100% load. At each load point, over 100 samples were taken of synchronised measurements of input and output power to arrive at the efficiency. The measurements revealed extra copper losses in the stator windings due to inner circulating currents and extra eddy current losses in solid conductive parts of the generator that were unaccounted. In [129], the authors stress the importance of accounting for these types of losses in this kind of configuration and proposes a methodology to predict with great accuracy the latter of the two losses.

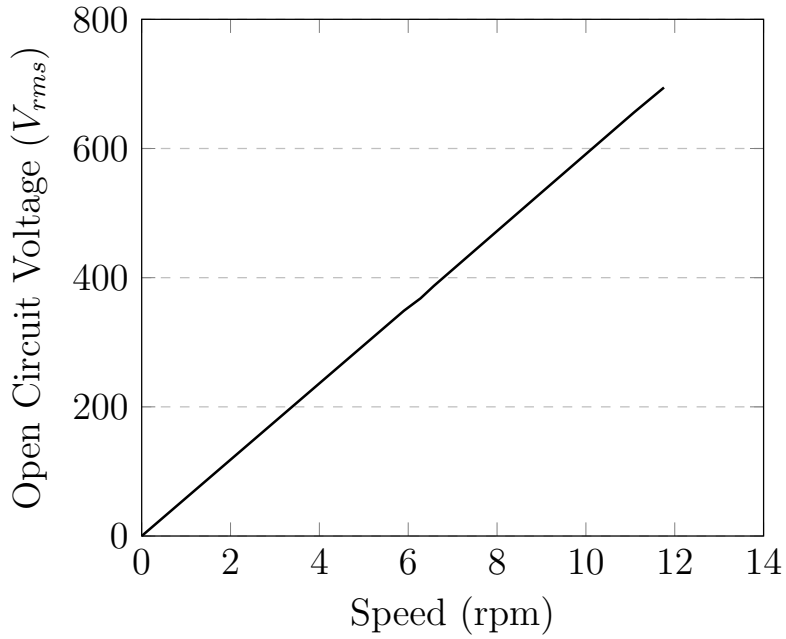

Figure 3.13: Open Circuit Voltage Characteristics as a function of generator speed (Graph adapted from [88])

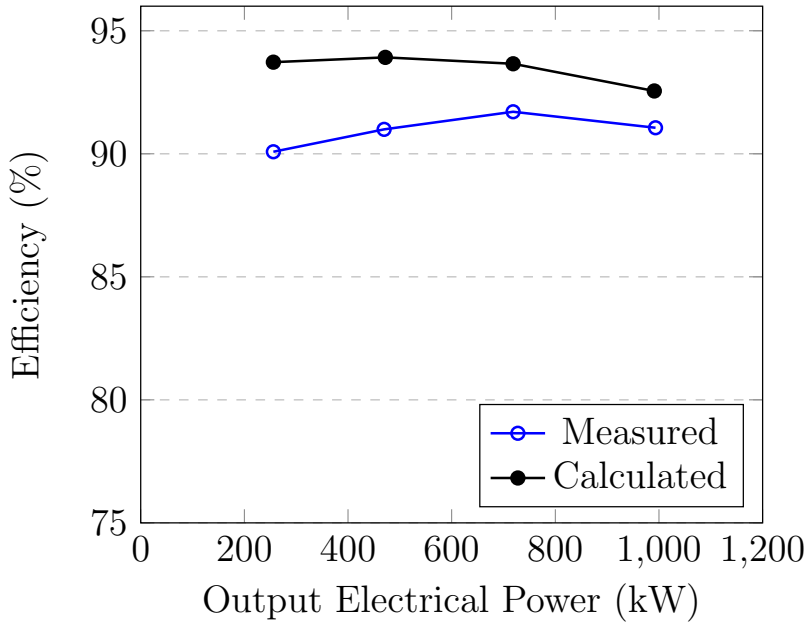

Figure 3.14: Efficiency as a function of the output power (Graph adapted from [88])

3.4 C-GEN Challenges

However, any breakthrough comes with challenges and these are highlighted below:

- Due to the lack of an iron-core in the stator as found in conventional machines, more permanent magnet material is needed to maintain the same air gap flux density, which results in increased cost, size and weight.
- As the application is direct-drive (no gearbox), this suggests an increased number of permanent magnets to achieve the same power (in order of megawatts) as its counterparts, thus increasing the overall cost and weight of the machine.
- Direct drive generator in the order of megawatts, entails large diameters and this can pose a problem as axial forces may arise which may compromise the air gap.

Ultimately, the desire is to increase the magnetic flux density of the effective air gap and the use of a Halbach array structure in the C-GEN topology may help realise this. We have already seen in Section 2.1, the Halbach array works by augmenting the magnetic field on one side of the array while cancelling the field to near zero on the other side. However, one key feature the author would like to amplify is the rotor yoke can be made of high strength non-ferromagnetic materials, such as glass fiber or carbon fiber instead of iron. These kind of materials are light weight, low cost and high strength, making it a good choice in order to reduce the mass of the C-GEN machines.

Chapter 4

Review of Two-Dimensional (2D) and Three-Dimensional (3D) Equations for an Axial Halbach Array

This chapter looks at the 2D and 3D equations established by Klaus Halbach [27] to describe the magnetic field equation of a Halbach array and proposes an improved 3D expression which is based on the equations established by Edward P Furlani [99]. Analytical models are less time consuming and can be extremely accurate when compared to FE models and they can serve as a crucial starting point for understanding the relationship between the input and output parameters [100]. Hence, they are commonly used for parametric optimization and design routines before any further FE modelling is implemented for further validation. However, in some complex cases, such as models with saturated soft magnetic materials or transient effects, FE methods are especially suitable [100].

4.1 Introduction to Relevant Maxwell Equations

This section provides a brief introduction into the equations that describes magnetic fields, which are necessary to aid in the derivation of the equations in the next section and to improve the understanding of the thesis.

A crucial component in magnetism is the magnetic dipole. It describes a set of closely separated magnetic poles, or equivalently a small current loop as seen in Figure 4.1 which is characterised by a magnetic dipole moment **m**. In permanent

magnets, a group of magnetic dipoles in a small vanishing volume V, the net magnetic dipole moment per unit volume, $\mathbf{M}$, is given by [101]

$$\mathbf{M} = \lim_{V \to 0} \frac{\sum \mathbf{m}}{V} \tag{4.1}$$

where $\mathbf{M}$ is characterized as the Magnetization of the material and is measured in A/m and the magnetic dipole moment $\mathbf{m}$ is measured in A m^2.

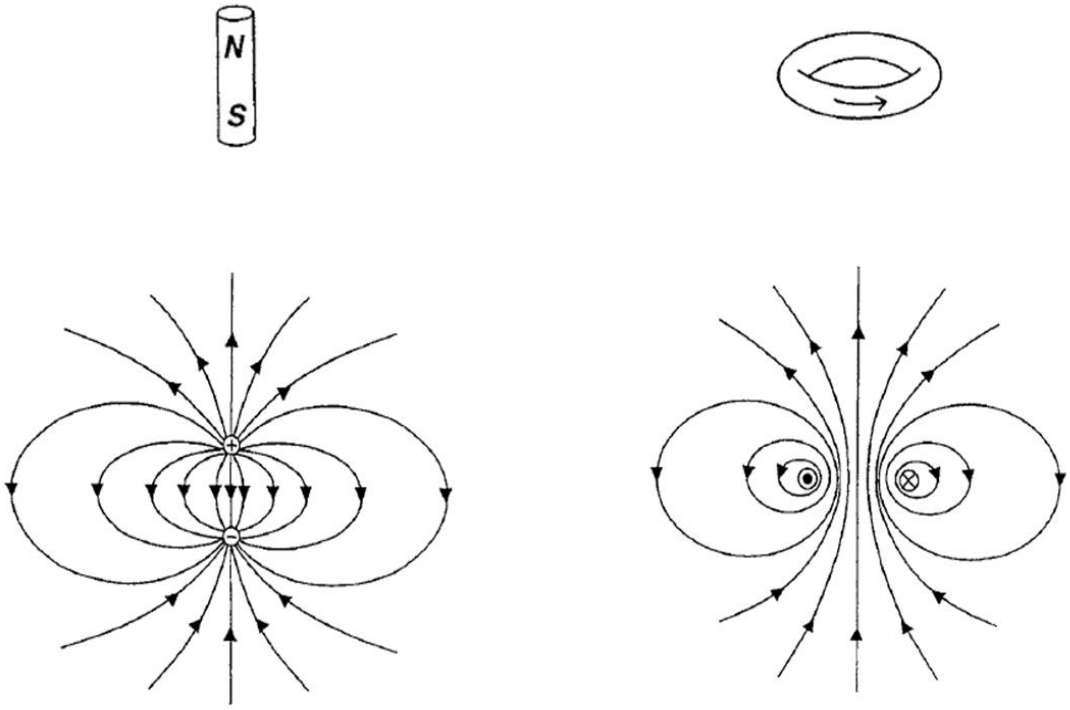

Figure 4.1: Magnetic Dipole of a Magnetic Charge Model and Current Loop (Image taken from [101])

In stationary, homogeneous [1] and linear materials, which is typically the case for rare-earth permanent magnets as a result of their high coercivity, the magnetic field, $\mathbf{B}$, in the presence of no external fields, is given by [101]

$$\mathbf{B} = \mu_o \mathbf{M} \tag{4.2}$$

where μ_o is known as the permeability of free space and is defined as $4\pi \times 10^{-7}$ T m/A.

1. A material is homogeneous if its permeability is not a function of position

As mentioned earlier, the magnetization of a material can otherwise arise from the presence of a circulating current which induces a magnetic field. This gives rise to another parameter regarded as the surface current density, $\mathbf{J}_m$ [101] which is given by

$$\mathbf{J}_m = \nabla \times \mathbf{M} \tag{4.3}$$

In order to establish a difference between the spontaneous magnetic field produced by the permanent magnet and the induced magnetic field from the current density $\mathbf{J}$ acting on said magnet, a further parameter is introduced, that is the induced magnetic field, $\mathbf{H}$, as seen below [38];

$$\mathbf{J} = \nabla \times \mathbf{H} \tag{4.4}$$

where $\mathbf{J}$ is measured in $\mathrm{A/m^2}$ and $\mathbf{H}$ is measured in A/m. Equation 4.4, is often regarded as a more general version of Ampere's Law [102].

The above equations by themselves don't provide a complete set of equations to describe the magnetic field. Thus, the magnetic field equations must be augmented by an additional independent equation as seen below [101];

$$\mathbf{B} = \mu_{\mathrm{o}}(\mathbf{H} + \mathbf{M}) \tag{4.5}$$

where $\mathbf{B}$ is referred to as the magnetic flux density and is measured in tesla.

Equation 4.5 may now be used to describe the magnetic field at all points within and outside a permanent magnet. Therefore, we now have the magnetic flux density $\mathbf{B}$ within the permanent magnet as a vector sum of $\mathbf{H}$ and $\mathbf{M}$, whereas anywhere outside the magnet, $\mathbf{M}$ tends to zero and the magnetic flux density is given as a relationship between the magnetic field intensity $\mathbf{H}$ and the constant μ_{o}. Consequently, the magnetic flux density $\mathbf{B}$ is continuous across the boundary whilst both $\mathbf{H}$ and $\mathbf{M}$ are discontinuous, this is further demonstrated in Figure 4.2 [102].

It is important to note, Equation 4.5 is only true for ideal permanent magnets, and it does not describe the situation of other materials in the presence of a magnetic field. In order to take this into consideration, we have [38];

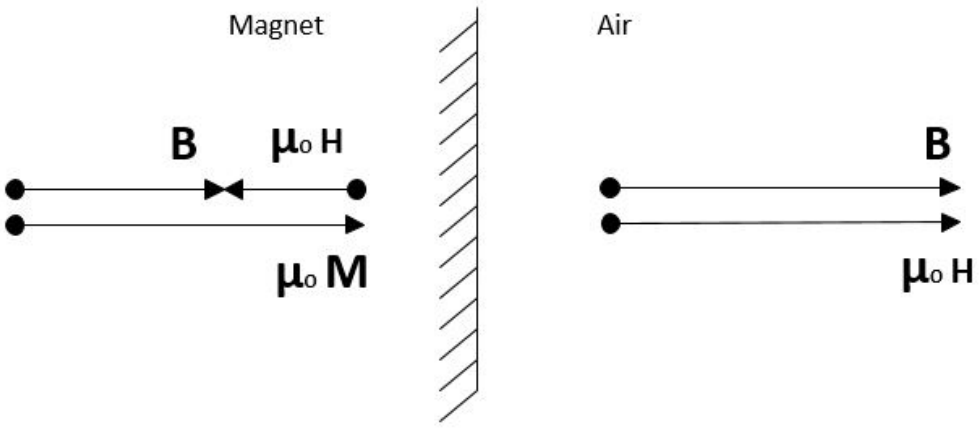

Figure 4.2: Field vectors either side of a magnet and air boundary (Image taken from [102])

$$\mu = \mu_{\mathrm{o}}\mu_{\mathrm{r}} = \frac{\mathbf{B}}{\mathbf{H}} \tag{4.6}$$

where μ is the permeability of a material and μ_{r} is described as relative permeability.

Inherently, the term magnetic flux density contains within it another phenomenon referred to as the magnetic flux, $\boldsymbol{\phi}$. This is used to describe the flow of magnetic fluid through a given area [38]. It is analogous with the flow of electric current through a conductor, although in this case the electric current is confined by the conductor. Therefore, we can define the amount of field lines passing through a certain amount of area as;

$$\boldsymbol{\phi} = \mathbf{B} \cdot \mathbf{A} \tag{4.7}$$

where the magnetic flux is measured in webers and $\mathbf{A}$ is area through which the flux passes.

4.2 Magnetic Field Equations of Permanent Magnet Materials

4.2.1 Choice of Analytical Model

There are two common analytical models used when describing the components of the magnetic field between permanent magnets, known as the surface charge otherwise referred to as the Coulombian model and the current model otherwise referred to as the Amperian model [101]. The charge method entails the determination of the scalar potential produced by the distribution of magnetic charges on the faces of the permanent magnet and inside it, whilst the current sheet model involves the determination of the vector potential established by assuming current flowing around or inside the magnets [103].

Expressions for the Coulombian model and Amperian model can be seen in Equation 4.8 and Equation 4.9 respectively. As we are dealing with rare earth permanent magnets, the magnetization of the magnets are assumed to be homogeneous and constant, therefore $\nabla \times \mathbf{M}$ and $\nabla \cdot \mathbf{M}$ tend to zero and are not included in the expressions [38]. Full derivation of the equations can be found in [101].

$$\mathbf{B}(\mathbf{x}) = \frac{\mu_{\mathrm{o}}}{4\pi} \oint_S \frac{\sigma_{\mathrm{m}}(\mathbf{x}')(\mathbf{x} - \mathbf{x}')}{\mid \mathbf{x} - \mathbf{x}' \mid^3} \delta s'. \tag{4.8}$$

where σ_{m}(surface charge density) $= \mathbf{M} \cdot \hat{\mathbf{n}}$ and it is measured in A/m, $\mathbf{x}$ is the observation point, $\mathbf{x}'$ is the source point, S is the surface and is $\hat{\mathbf{n}}$ the outward unit normal [101].

$$\mathbf{B}(\mathbf{x}) = \frac{\mu_{\mathrm{o}}}{4\pi} \oint_S \mathbf{j}_{\mathrm{m}}(\mathbf{x}') \times \frac{(\mathbf{x} - \mathbf{x}')}{\mid \mathbf{x} - \mathbf{x}' \mid^3} \delta s'. \tag{4.9}$$

where $\mathbf{j}_{\mathrm{m}}$(surface current density) $= \mathbf{M} \times \hat{\mathbf{n}}$ and is measured in A/m [101].

The two above approaches are equivalent and are used to derive the equations to calculate the magnetic field between permanent magnets of arbitrary geometry. The question here is what technique is most suitable for calculating the three components of the magnetic field generated by permanent magnets or in some cases via electromagnetic coils which is a relevant question posed by Ravaud and

Lemarquand [103]. As this is beyond the scope of the thesis, it is not discussed further but more information is provided in [38]. The equations described below employ the Amperian model and are used for further analysis as they have already been validated in the literature [60] [104].

4.2.2 Halbach Two and Three-Dimensional Magnetic Field Equation

Rare earth permanent magnet materials such as neodymium-iron-boron have a very high remanent field and a relative permeability close to 1. This allows for these materials to be considered as a vacuum with applied magnetization **M**. Hence, the magnetic field anywhere outside the permanent magnets can be described by Equation 4.10 and Equation 4.11:

$$\mathbf{B} = -\nabla \boldsymbol{\phi} \qquad (4.10) \qquad\qquad \mathbf{B} = \nabla \times \mathbf{A} \qquad (4.11)$$

where $\boldsymbol{\phi}$ is the scalar potential and **A** is the vector potential.

Subsequently, K.Halbach by solving the Poisson equation using Fourier transforms approximate 2D field expressions of the perpendicular and horizontal field as seen in (4.12) and (4.13) below [60] [105] [106]:

$$\mathbf{B}_y = 2\mathrm{B_r} \sum_{i=0}^{\infty} \frac{\sin(\epsilon n\pi/m)}{n\pi/m} \left(1 - e^{-nkh}\right) e^{-n\pi g/\lambda} \cosh(nky) \cos(nkx) \qquad (4.12)$$

$$\mathbf{B}_x = 2\mathrm{B_r} \sum_{i=0}^{\infty} \frac{\sin(\epsilon n\pi/m)}{n\pi/m} \left(1 - e^{-nkh}\right) e^{-n\pi g/\lambda} \sinh(nky) \sin(nkx) \qquad (4.13)$$

where k is the wave number, $2\pi/\lambda$, and λ is the wavelength of the array between like poles, $n = 1 + im$, m is the number of pieces per wavelength, h is the height of the permanent magnet in the array,ϵ usually set to 1, and g is the gap between permanent magnets in a double sided array.

Figure 4.3 shows a 2D view of a linear Halbach array. This is used to validate the field expressions established above using the selected design parameters:

$$h = 10\,mm$$
$$g = 22\,mm$$
$$\lambda = 145.846\,mm$$
$$\mathrm{B_r} = \mu_o \mathbf{M} = 1.1764\,T$$

These parameters match those of a 25 kW NGenTeC Halbach AFPM generator single-stage concept.

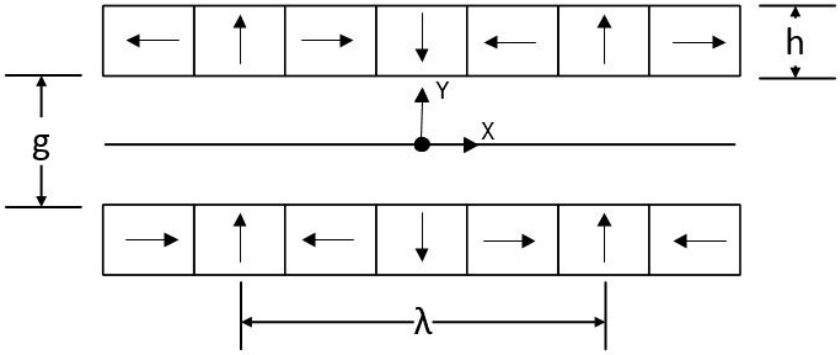

Figure 4.3: Planar Multipole Array

Finite Element Method Magnetics (FEMM) Version 4.2 was used to perform a magnetostactic analyis of the above model and a comparison with the theoretical results is presented in Figure 4.4.

> "*FEMM is a suite of programs for solving low frequency electromagnetic problems on 2D planar and axisymmetric domains. The program currently addresses linear/non-linear magnetostatic problems, linear/non-linear time harmonic magnetic problems, linear electrostatic problems, and steady-state heat/flow problems.* "
>
> — David Meeker

Figure 4.4 compares the horizontal dependence of the $\mathbf{B}_{\mathrm{y}}$ component of the analytical and FEMM models at a gap distance of $g = 0$. The FEMM results are shown as markers at selected points and the results of analytical expressions are shown as a smoothed blue line. The plot indicates a good agreement, with practically no difference between the implementation of the analytical model presented in this section and an equivalent (Finite Element Analysis) FEA model. Furthermore, Post established, in this type of arrangement of Halbach array, that with four magnets per wavelength, λ, the only significant undesirable harmonics asides from the fundamental is the fifth harmonic. This explains the distortion observed in Figure 4.4 and this decays with distance from the array [107]. More precisely, at gap values smaller than the thickness of the PMs, significant harmonics are present and even closer to the surface of the PMs, we find even higher order harmonics, this can be seen in Figure 4.5.

Although, this can be counteracted by introducing thin non-magnetic sheets

between adjacent PM pieces [108] or by separating adjacent PMs by incorporating small air gaps between PMs which also helps to reduce the risk of proximity demagnetization from adjacent PMs [54]. However as stated in [104] for most practically applications, which involve the computation of flux linkage in a winding, the gap is sufficiently large such that the undesirable harmonic content can be neglected.

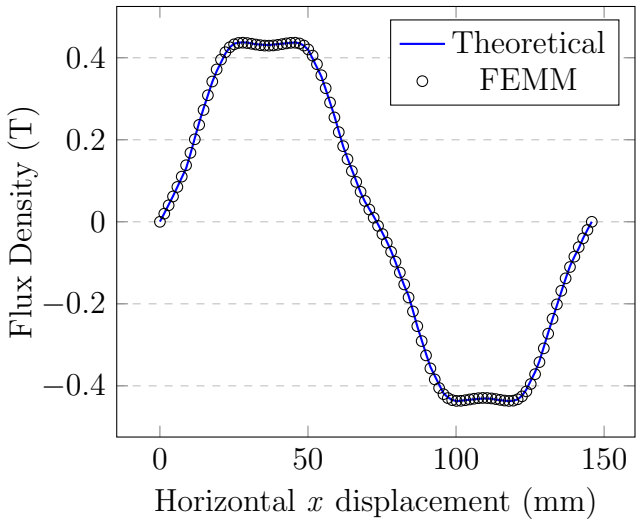

Figure 4.4: Perpendicular field values along the x axis for the planar Halbach array

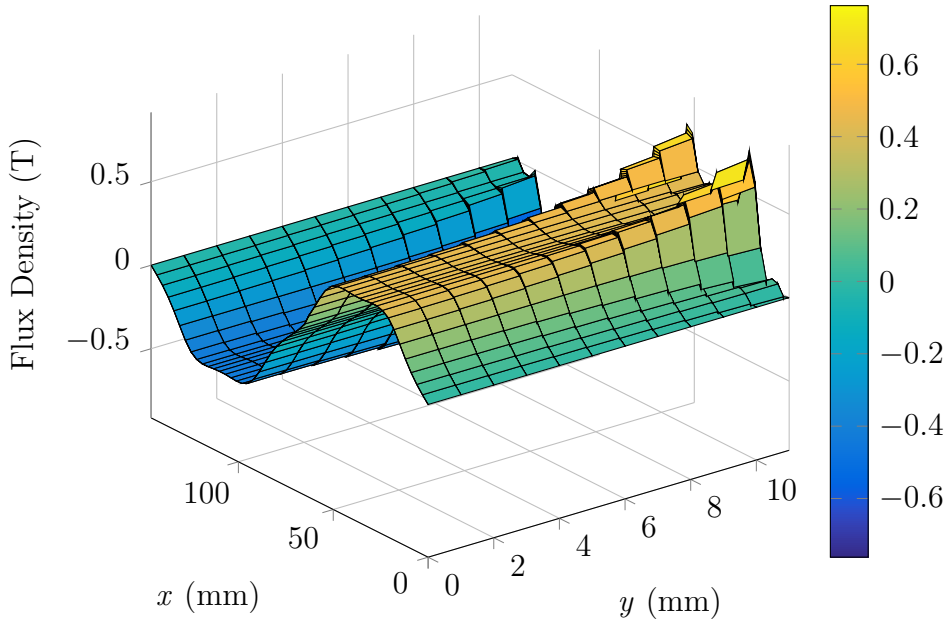

Figure 4.5: Spatial Distribution of By on the x-y plane

Only the analysis of the vertical component, B_y, is studied since the magnetic field is expected to be along the axial direction and hence, the induced voltage in the coils (not shown in Figure 4.4) is dependent on the vertical component of the magnetic field. The horizontal component, B_x may be analysed in a similar way as above.

Inherently, modelling a 3D problem in 2D, implies that the model is a constant cross-section extending to infinity in the third dimension, this is not always the case. Thus, if the approximation of an infinite pole in the $z-$direction turns out to be insufficient then the dependence on the third coordinate is proposed in [106] by introducing a correction factor.

Despite the benefit of the correction factor, there are still a number of limitations with the field equations:

- The introduction of the third dimension allows for a description of the model in the z dimension but limits the shape of the PMs to a rectangle. If the individual pieces are trapezoid as is found in the 25 kW AFPM NGenTec generator this cannot be fully explored.
- The field expressions are limited to a one-sided or double-sided array single-stage machine, a multi-stage topology is more complex and requires different field solutions.

Thompson developed a 3D field solution for an axially oriented cylindrical Halbach array based upon Furlani's work which addresses the above shortcomings [104]. The analysis is based upon the assumption of ideal magnets with fixed and uniform magnetization. The model also requires there to be a sufficiently large number of PMs in order to keep the angular span of each individual PM in the array small. This has the advantage of allowing each sector in the array (See Figure 4.6) to be reduced to four equivalent current sheets. Subsequently, the field solution is computed by employing the Amperian model and integrating Green's free space function over two spatial dimensions. This results in a field equation comprising of sums of 2D definite integrals. Furthermore, the total field is expressed as a sum of the contributions from all the sectors in the array by using the principle of linear superposition provided the PMs are not driven out of the linear portion of the BH curve (See Figure 4.7) [99].

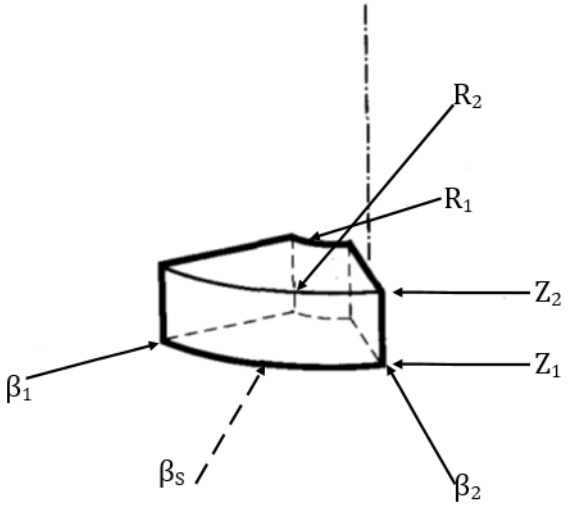

Figure 4.6: One Sector Geometry (Image modified from [99])

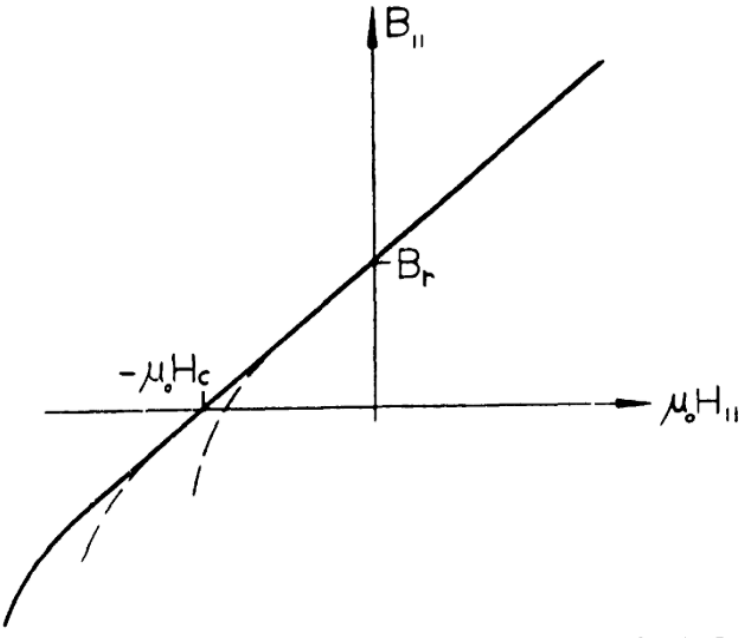

Figure 4.7: Typical BH Curve for Rare Earth Cobalt (REC) PM (Image taken from [60])

The field components for an axially magnetized PM is shown in Equation 4.14, 4.15 and 4.16 below [104]:

$$B_{r,a}(\vec{r}) = \pm\frac{\mu_o M}{4\pi}\sum_{j=1}^{2}(-1)^j \left[\left[\int_{z_1}^{z_2}\int_{\beta_1=\frac{(4n-1)\pi}{N_m}}^{\beta_2=\frac{(4n+1)\pi}{N_m}} \frac{(z-z')\cos(\phi-\phi')}{|\vec{r}-\vec{r'}|^3} r' d\phi' dz' \right]_{r'=r_j} + \left[\int_{z_1}^{z_2}\int_{r_1}^{r_2} \frac{(z-z')\sin(\phi-\phi')}{|\vec{r}-\vec{r'}|^3} dr' dz' \right]_{\phi'=\beta_j=\frac{(4n+2j-3)\pi}{N_m}} \right] \tag{4.14}$$

$$B_{\phi,a}(\vec{r}) = \pm\frac{\mu_o M}{4\pi}\sum_{j=1}^{2}(-1)^{j+1} \left[\left[\int_{z_1}^{z_2}\int_{\beta_1=\frac{(4n-1)\pi}{N_m}}^{\beta_2=\frac{(4n+1)\pi}{N_m}} \frac{(z-z')\sin(\phi-\phi')}{|\vec{r}-\vec{r'}|^3} r' d\phi' dz' \right]_{r'=r_j} - \left[\int_{z_1}^{z_2}\int_{r_1}^{r_2} \frac{(z-z')\cos(\phi-\phi')}{|\vec{r}-\vec{r'}|^3} dr' dz' \right]_{\phi'=\beta_j=\frac{(4n+2j-3)\pi}{N_m}} \right] \tag{4.15}$$

$$B_{z,a}(\vec{r}) = \pm\frac{\mu_o M}{4\pi}\sum_{j=1}^{2}(-1)^{j+1} \left[\left[\int_{z_1}^{z_2}\int_{\beta_1=\frac{(4n-1)\pi}{N_m}}^{\beta_2=\frac{(4n+1)\pi}{N_m}} \frac{r\cos(\phi-\phi')-r'}{|\vec{r}-\vec{r'}|^3} r' d\phi' dz' \right]_{r'=r_j} + \left[\int_{z_1}^{z_2}\int_{r_1}^{r_2} \frac{r\sin(\phi-\phi')}{|\vec{r}-\vec{r'}|^3} dr' dz' \right]_{\phi'=\beta_j=\frac{(4n+2j-3)\pi}{N_m}} \right] \tag{4.16}$$

The field components for a transversely magnetized PM can be seen in Equation 4.17, 4.18 and 4.19 below [104]:

$$B_{r,t}(\vec{r}) = \pm\frac{\mu_o M}{4\pi}\sum_{j=1}^{2}(-1)^{j+1}\left[\left[\int_{z_1}^{z_2}\int_{\beta_1=\frac{(4n+1)\pi}{N_m}}^{\beta_2=\frac{(4n+3)\pi}{N_m}}\frac{\sin(\phi-\phi')}{|\vec{r}-\vec{r}'|^3}r'^2 d\phi' dz'\right]_{r'=r_j} + \left[\int_{r_1}^{r_2}\int_{\beta_1=\frac{(4n+1)\pi}{N_m}}^{\beta_2=\frac{(4n+3)\pi}{N_m}}\frac{(z-z')\sin(\phi-\phi')}{|\vec{r}-\vec{r}'|^3}r' dr' dz'\right]_{z'=z_j}\right] \tag{4.17}$$

$$B_{\phi,t}(\vec{r}) = \pm\frac{\mu_o M}{4\pi}\sum_{j=1}^{2}(-1)^{j+1}\left[\left[\int_{r_1}^{r_2}\int_{\beta_1=\frac{(4n+1)\pi}{N_m}}^{\beta_2=\frac{(4n+3)\pi}{N_m}}\frac{(z-z')\cos(\phi-\phi')}{|\vec{r}-\vec{r}'|^3}r' d\phi' dr'\right]_{z'=z_j} + \left[\int_{z_1}^{z_2}\int_{\beta_1=\frac{(4n+1)\pi}{N_m}}^{\beta_2=\frac{(4n+3)\pi}{N_m}}\frac{(r-r'\cos(\phi-\phi'))}{|\vec{r}-\vec{r}'|^3}r' d\phi' dz'\right]_{r'=r_j}\right] \tag{4.18}$$

$$B_{z,t}(\vec{r}) = \pm\frac{\mu_o M}{4\pi}\sum_{j=1}^{2}(-1)^{j+1}\left[\left[\int_{r_1}^{r_2}\int_{\beta_1=\frac{(4n+1)\pi}{N_m}}^{\beta_2=\frac{(4n+3)\pi}{N_m}}\frac{-r\sin(\phi-\phi')}{|\vec{r}-\vec{r}'|^3}r' d\phi' dr'\right]_{z'=z_j}\right] \tag{4.19}$$

The complete field components for an entire array can be computed by traversing the array and summing up the contribution of each sector. The expressions can be seen in (4.20), (4.21) and (4.22).

$$B_r(\vec{r}) = \frac{\mu_o M}{4\pi} \sum_{n=0}^{\frac{N_m}{2}-1} (-1)^n \sum_{j=1}^{2} (-1)^j \left[B_{r,a}(\vec{r}) + B_{r,t}(\vec{r}) \right] \tag{4.20}$$

$$B_\phi(\vec{r}) = \frac{\mu_o M}{4\pi} \sum_{n=0}^{\frac{N_m}{2}-1} (-1)^n \sum_{j=1}^{2} (-1)^j \left[B_{\phi,a}(\vec{r}) + B_{\phi,t}(\vec{r}) \right] \tag{4.21}$$

$$B_z(\vec{r}) = \frac{\mu_o M}{4\pi} \sum_{n=0}^{\frac{N_m}{2}-1} (-1)^n \sum_{j=1}^{2} (-1)^j \left[B_{z,a}(\vec{r}) + B_{z,t}(\vec{r}) \right] \tag{4.22}$$

where N_m is the number of poles and n is indexing variable for each sector.

This only satisfies the case for the typical Hablach arrangement (90^o rotation of magnetization between sectors, as you move along the array). In order to explore other cases as seen in Figure 2.5, we can employ Pythagoras' theorem (See Figure 4.8) to superimpose the axial and transverse components of each field expression ($B_r(\vec{r})$, $B_\phi(\vec{r})$ and $B_{z,a}(\vec{r})$), to obtain the desired angle. Again, this analysis assumes ideal magnets with fixed and uniform magnetization.

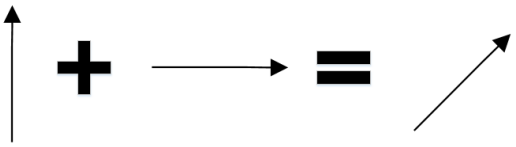

Figure 4.8: Unification of axial and transverse components

Therefore, we now have modified field expressions which are of the form:

$$B_r(\vec{r}) = \frac{\mu_o M}{4\pi} \sum_{n=0}^{\frac{N_m}{2}-1} (-1)^n \sum_{j=1}^{2} (-1)^j \left[(B_{r,a}(\vec{r}); \beta_1, \beta_2) + (B_{r,t}(\vec{r}); \beta_1, \beta_2) \right] \tag{4.23}$$

$$B_{\phi}(\vec{r}) = \frac{\mu_o M}{4\pi} \sum_{n=0}^{\frac{N_m}{2}-1} (-1)^n \sum_{j=1}^{2} (-1)^j \left[(B_{\phi,a}(\vec{r}); \beta_1, \beta_2) + (B_{\phi,t}(\vec{r}); \beta_1, \beta_2) \right] \quad (4.24)$$

$$B_{z}(\vec{r}) = \frac{\mu_o M}{4\pi} \sum_{n=0}^{\frac{N_m}{2}-1} (-1)^n \sum_{j=1}^{2} (-1)^j \left[(B_{z,a}(\vec{r}); \beta_1, \beta_2) + (B_{z,t}(\vec{r}); \beta_1, \beta_2) \right] \quad (4.25)$$

Here, β_1 and β_2 are the same for the normal and tangential components of the above expressions.

4.2.3 Modified Thompson Field Equations and Soft Magnetic Material

In a Halbach arrangement, the magnetic field is amplified on one side and cancelled on the other as stated in chapter 2. In reality, this is not the case, most of the field would be restricted to one side, but there would be some field in the reverse side of the array, which can potentially be harnessed by re-introducing a magnetic conducting material such as iron as seen in left-hand side of Figure 4.9.

This presents a new situation, the PMs are in contact with a material of a high permeability. The most common approach to resolve this problem analytically, is by employing the method of images. The method of images is a technique which was originally developed to solve electrostatic problems with high degree of symmetry, but has been shown to work well with some magnetostatic cases. It was developed to ensure the magnetic field at the interface between mediums satisfies the boundary conditions. The domain of the problem is extended by adding PM mirror images to infinity outside of the computational region in question, which accounts for the ferromagnetic region (iron) [109] [110] [111] [112] [113]. In order to solve this kind of problem analytically, the following assumptions are made [114]:

- The permeability of the back iron is infinite ($\mu_r \approx \infty$).
- The BH characteristics of the PMs is considered linear ($\mu_r \approx 1$).
- The effects of temperature are negligible.
- The magnetization of the PM is homogenous and uniform.

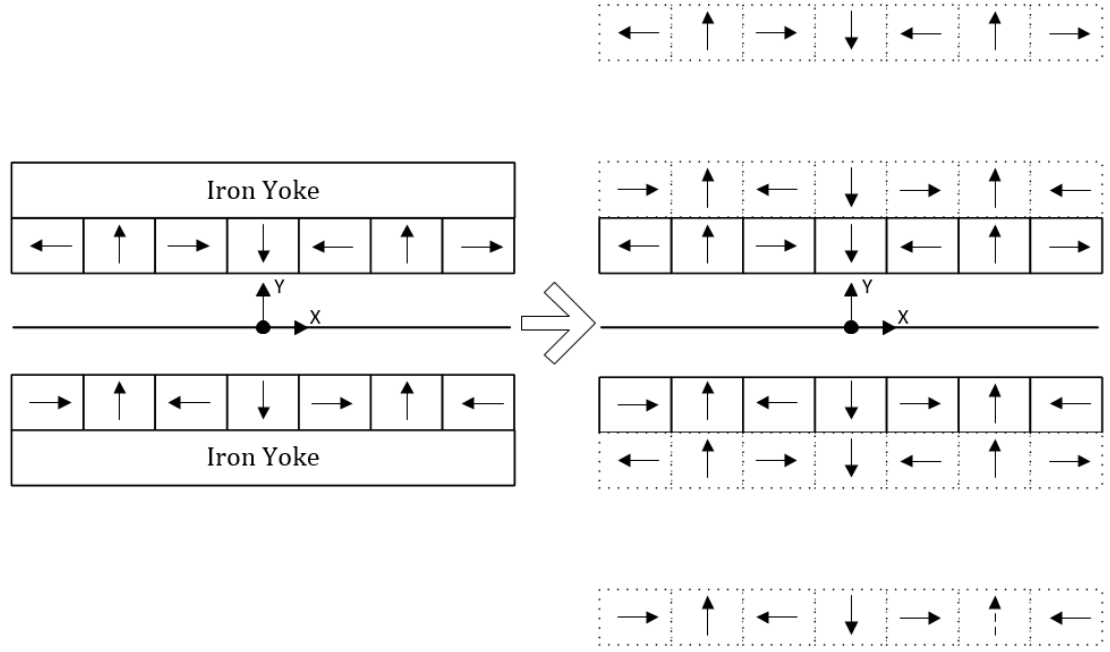

Figure 4.9: The Concept of Image Method

The total field expressions can now be computed as a superposition of the field due to original source and the image fields suspended in free space. Therefore, if we consider the image model in Figure 4.9 and (4.20), (4.21) and (4.22) which describes the field of the source field we have:

$$B_{rT}(\vec{r}) = (B_{rs}(\vec{r}); Z_1, Z_2) + (B_{r1}(\vec{r}); Z_3, Z_4) + (B_{r2}(\vec{r}); Z_5, Z_6).... \tag{4.26}$$

$$B_{\phi T}(\vec{r}) = (B_{\phi s}(\vec{r}); Z_1, Z_2) + (B_{\phi 1}(\vec{r}); Z_3, Z_4) + (B_{\phi 2}(\vec{r}); Z_5, Z_6).... \tag{4.27}$$

$$B_{zT}(\vec{r}) = (B_{zs}(\vec{r}); Z_1, Z_2) + (B_{z1}(\vec{r}); Z_3, Z_4) + (B_{z2}(\vec{r}); Z_4, Z_6).... \tag{4.28}$$

where $B_{rT}(\vec{r})$, $B_{\phi T}(\vec{r})$ and $B_{zT}(\vec{r})$ is the total field, $B_{rs}(\vec{r})$, $B_{\phi s}(\vec{r})$ and $B_{zs}(\vec{r})$ represents the field due to the source and $B_{r1}(\vec{r})$, $B_{r2}(\vec{r})$, $B_{\phi 1}(\vec{r})$, $B_{\phi 2}(\vec{r})$ and $B_{z1}(\vec{r})$, $B_{z2}(\vec{r})$ describes the first and second images. As stated earlier this continues to infinity, but in some cases it is sufficient to include only a few images with minimal error [115]. Bear in mind finite element packages such as FEMM can be used to solve the above described problem, however, an analytical method is beneficial for repetitive and optimisation processes.

4.2.4 25 kW C-GEN Halbach Case Study

Soft magnetic materials such as iron are commonly used in electrical machines, because of their flux focusing properties which greatly increases Force/Torque capabilities. Nonetheless, the inclusion of such materials leads to undesirable effects such as eddy-currents and hysteresis losses, increase in weight which need to be mitigated [114]. As a result, this section looks at static 2D analysis of a Standard 25 kW C-GEN Machine and a Halbach alternative in the absence of soft magnetic material as a first step. Static 2D analysis provides a quick and good visualisation of the field variation and enables calculation of the flux density waveforms, induced EMF, verifying the Halbach analytical formulas and checking the validity of the developed 3D approximation.

Let us consider the general purpose sizing equation for an axial flux permanent magnet (AFPM) machines established in [116]. Fixing the dimensions of the machine, the output power can be expressed as a function of the magnetic and electric loading

$$P_{out} \propto \hat{B}_g A_{RMS} \tag{4.29}$$

where P_{out} is the output power of the machine, $\hat{B}_g$ is the flux density in the air gap and A is total electrical loading. Typically, the magnetic loading is expressed as the peak value of the first harmonic, and the electric loading as an Root Mean Square (RMS) value. The product of the magnetic and electric loading define the shear stress of the machine.

High air gap shear stress within a desired geometry results in a more compact machine capable of a high torque carrying capability. It is essential to balance the effects of magnetic and electric loading for best performance. Increasing the current density, results in more generated heat due to copper losses which increases the operating temperature and a risk of PM demagnetisation. Of course, more cooling can be employed. Yet a potentially better approach can be employed. Ensuring the magnetic flux density in the air gap is as high as possible means a high magnetic loading and this can be achieved by using PMs arranged in Halbach array [51]. Hence, the following analysis focuses on the air gap flux density.

In this study, the armature windings were neglected, in order to only evaluate the

contribution of the PMs to the useful flux without interference from armature reaction. The following steps were implemented;

1. Perform 2D magnetostatic analysis on the Axial 25 kW SMART C-GEN prototype as the Standard model and assess the air-gap flux density.
2. Exclude the back iron and carry out the same analysis as in step 1.
3. Finally, whilst maintaining the core dimensions of the generator, implement a Halbach array pattern ensuring the flux direction remains the same as in step 1.

Prior to establishing the 2D FEMM Halbach models mentioned above, to better understand what angles between vectors of magnetisation of adjacent magnets is best suited to the C-GEN topology, an initial analysis was conducted using the traditional arrangements found in [51].

Gieras et al conducted a 2D Finite Element Modelling (FEM) of the magnetic field in the air gap of a coreless AFPM brushless machine. Permanent magnets of NdFeB were used with remanent flux density of 1.2 T and coercivity equals to 950 kA/m. The thickness of each PM was set to 6 mm with a coreless stator winding thickness of 10 mm and a one-sided air gap thickness equal to 1 mm. Figure 4.10 shows the various Halbach arrangements analysed and the flux contours respectively. It was found the Halbach array resulted in a high peak value over 0.6 T of the normal component of the magnetic flux density as observed in Figure 4.11. Furthermore, the 60^o and 45^o were stated to produce similar peak magnetic flux density, which was identified to be higher than that in a Standard arrangement.

Gieras went further to indicate with an optimized magnetic circuit, the peak value of the flux density can be even higher, with a better increase in flux density for a Halbach array excitation than a double-sided PM structure with a backing ferromagnetic support for large gaps.

Based on this a similar static analysis was carried out with rough magnetic parameters pertaining to the 25 kW C-GEN prototype and the results of this analysis can be seen in Figure 4.12. It appears overall from this analysis that PM's arranged in a Halbach fashion produce a higher peak flux density compared to the Standard C-GEN. However, this should be taken with little confidence as the magnetic properties of the permanent magnets used are not precise due to insufficient data at the time. It can also be noticed by employing the Halbach arrangements seen in Figure 4.10, we arrive at a less than sinusoidal shape com-

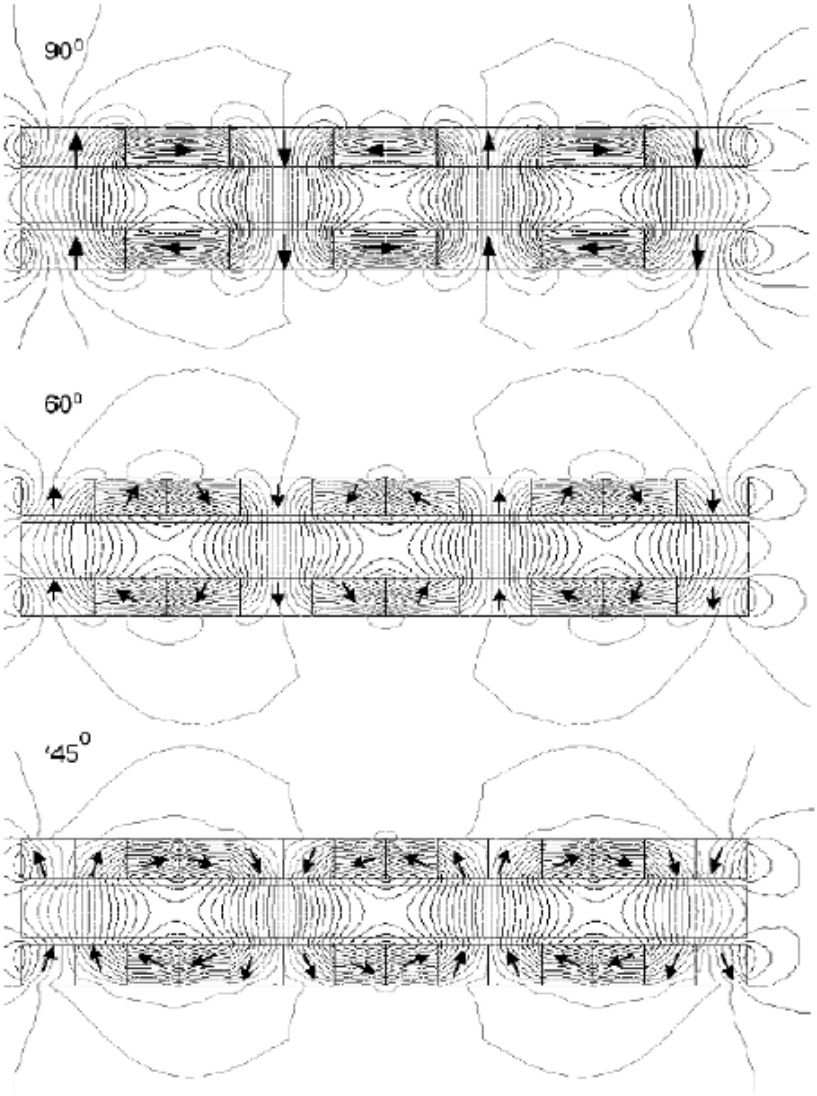

Figure 4.10: FEM Results of the twin rotor PMs in 90^{o}, 60^{o}, and 45^{o} Halbach array (Image taken from [51])

pared to Figure 4.11. This arrangement seems to work well for Gieras et al, as the magnetisation angle of rotation coupled with the machine parameters, especially the ratio of magnet height and array wavelength results in a smooth change of angle between consecutive PM segments. A better approach was identified after a review of the literature found in [38] [48], which ensures the angle of PM

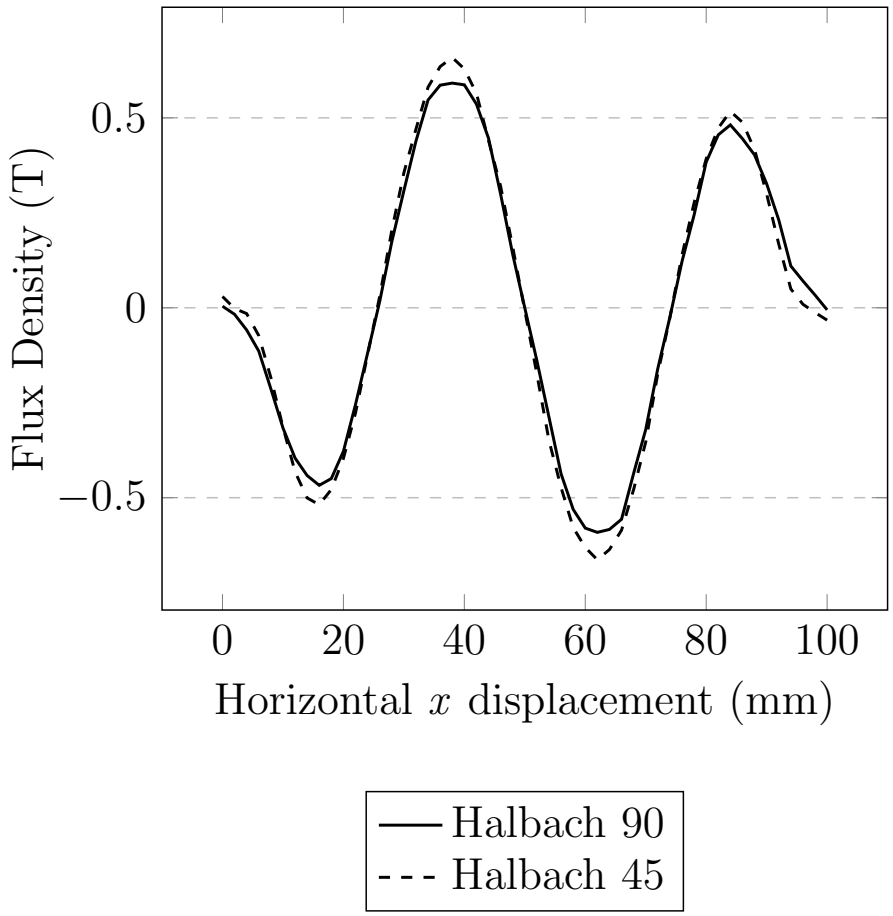

Figure 4.11: The Normal components of the magnetic flux density in the centre of the air gap of a double-sided coreless AFPM brusheless machine excited by Halbach arrays of PMs. Image extracted from [51]

magnetisation doesn't change too abruptly from one PM to the next, resulting in a more sinusoidal waveform and a reduced risk of proximity demagnetisation which can occur especially at elevated temperatures. Lastly, rather than a rotation of 45° as seen in Figure 2.5 a combination of 90 and 60 was chosen for the analysis discussed below which produced a more sinusoidal profile as opposed to a sharp peak observed in Figure 4.12. Now that we have established a starting point which is generally optimised we can proceed with a more precise analysis.

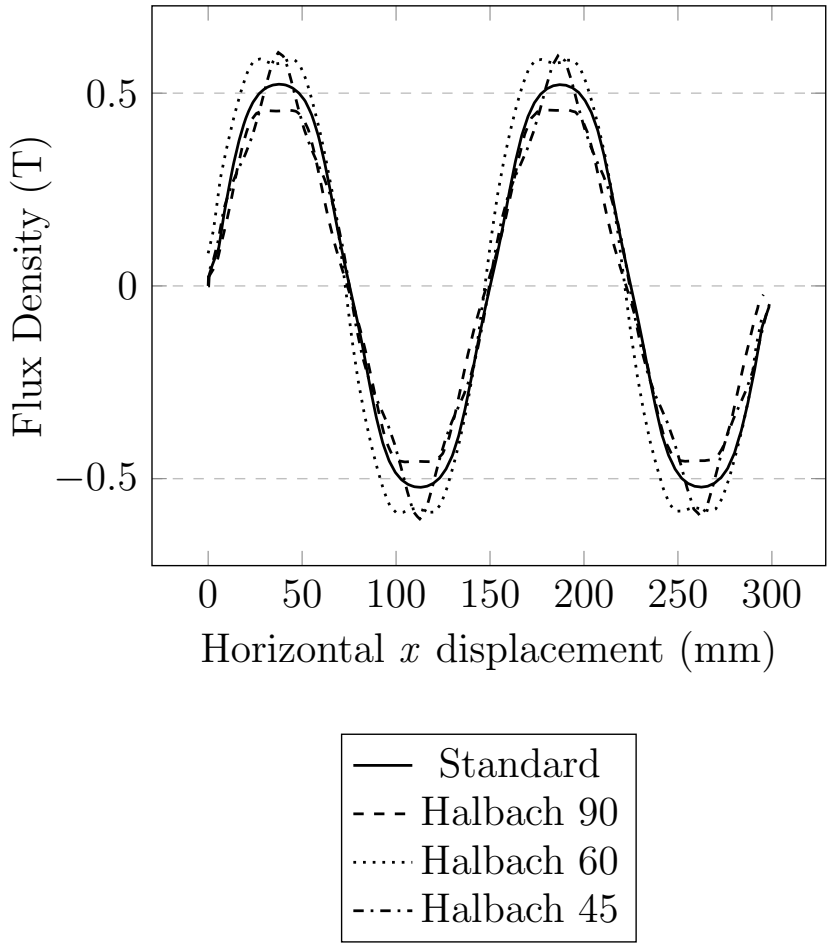

Figure 4.12: Perpendicular field values along the x axis for the 25 kW C-GEN Prototype. Image taken from [117]

Table 4.1 shows the parameters for N33H at room temperature derived from manufacturer's data [118] and Figure 4.13 shows the B/H curve of cast iron [59]. The authors believes these materials are as close as possible to the magnetic properties of the 25 kW C-GEN Prototype based on the available documentation from NGenTeC Ltd. Figure 4.14 and Figure 4.15 show a fraction of the models designed and developed in FEMM 2D. The magnetization direction of the PMs is indicated by the black arrows for visualisation reasons and each model consists of 3 stages.

	Design	Units
Remanent Field	1.17	T
Coercivity	879	kA/m
Relative Permeability	1.05	

Table 4.1: Parameters for Grade N33H NdFeBr Magnet

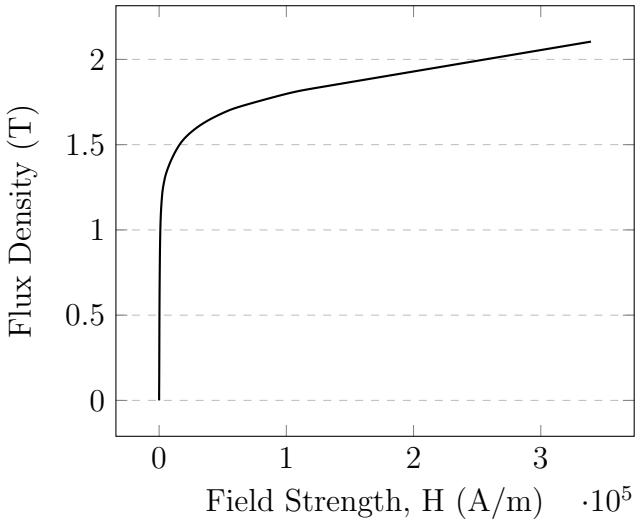

Figure 4.13: BH Curve for Cast Iron

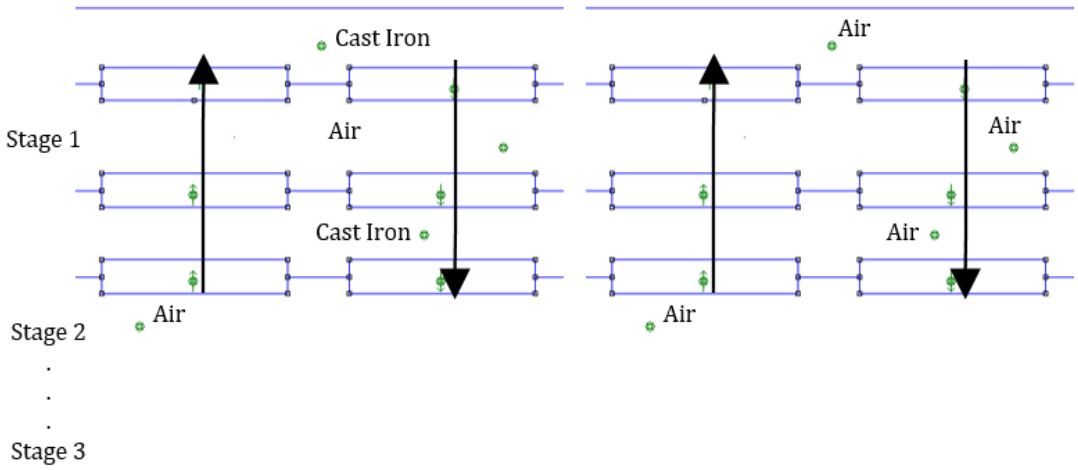

Figure 4.14: FEMM 2D Representation of C-GEN 25 kW

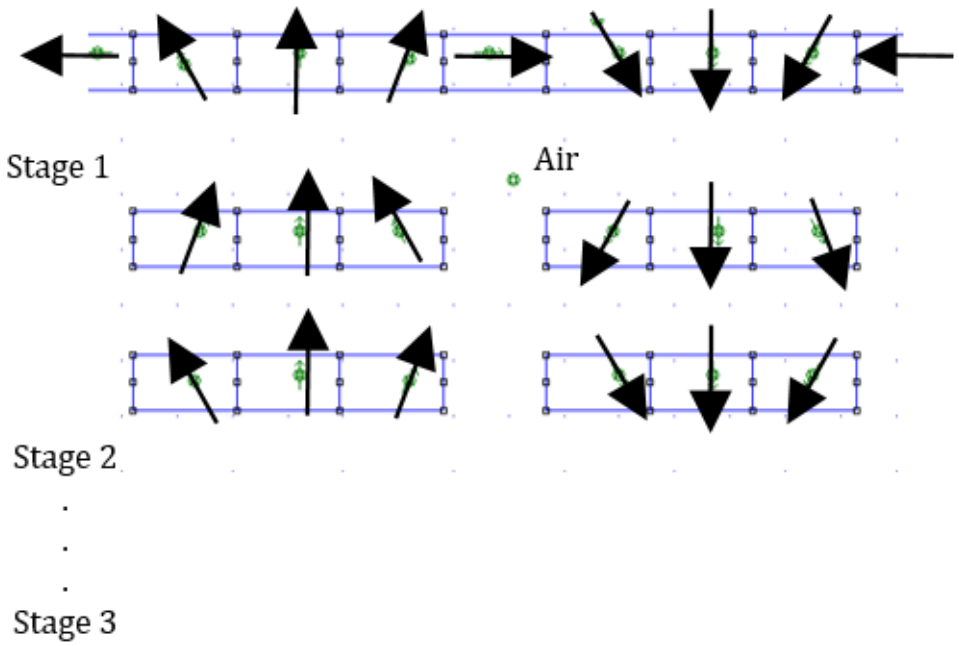

Figure 4.15: FEMM 2D Representation of C-GEN 25 kW Halbach Concept without Cast Iron

The Halbach model follows a 90 and 60 degree of rotation as seen above. The main model dimensions are kept the same in all cases and as accurate as possible. This was done in order to achieve a fair comparison between the Halbach and Standard arrangements. The north and south poles in the Halbach model includes all PMs except from the horizontally magnetized pieces, they only serve to concentrate the flux to the strong side of the array.

Figure 4.16 and Figure 4.17 show the field distribution of all models. It can be observed that omitting cast iron from the Standard model results in a significant amount of leakage flux and an increase in flux linking between adjacent PM pieces which is undesirable as it leads to a drop in the useful flux in the air gap. The leakage flux is indicated by the red circles. This is significantly circumvented by replacing each stage with a Halbach array to help focus the flux in the air gap.

However, the amplitude of the Halbach model (90 60) is 15% less than the Standard model (See Figure 4.18). A direct replacement of the Standard model in this case appears to be insufficient. Furthermore, the middle stage exhibits some subtle irregularities when compared to the exterior stages (See Figure 4.19), which could be merely a consequence of incorporating a Halbach array in a multi-stage topology, were the full array exists at the peripheral stages. It is worth noting that the Halbach 90 60, although more sinusoidal, is reduced in amplitude compared to Figure 4.10 and underperforms in comparison to the results produced by Gieras. This comes as a consequence of a larger air gap found in the 25 kW prototype and upon closer inspection, the magnetic properties used to derive the results in Figure 4.10, particularly the Halbach models, were found to be overestimated leading to a higher peak flux density.

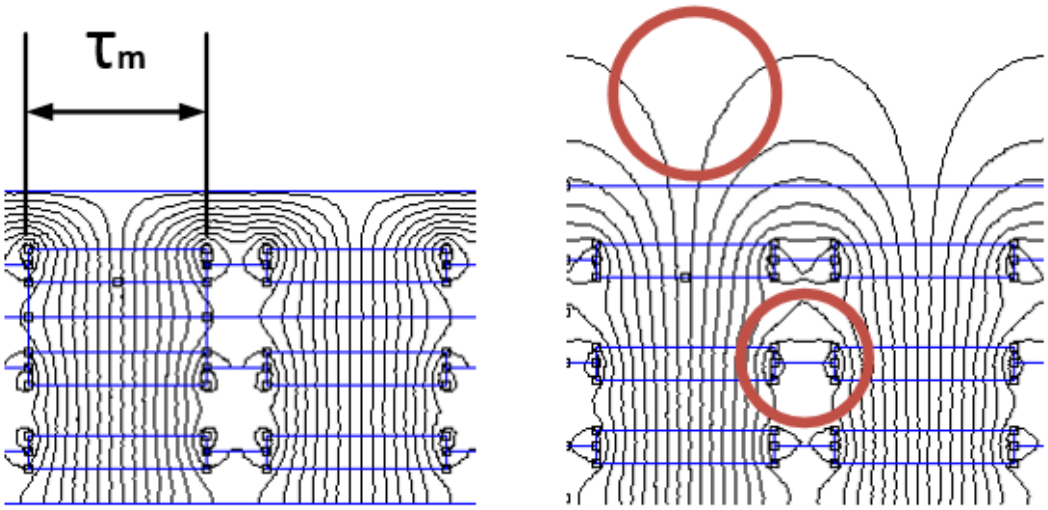

Figure 4.16: Magnetic Flux lines of a linear C-GEN 25 kW with and without Iron

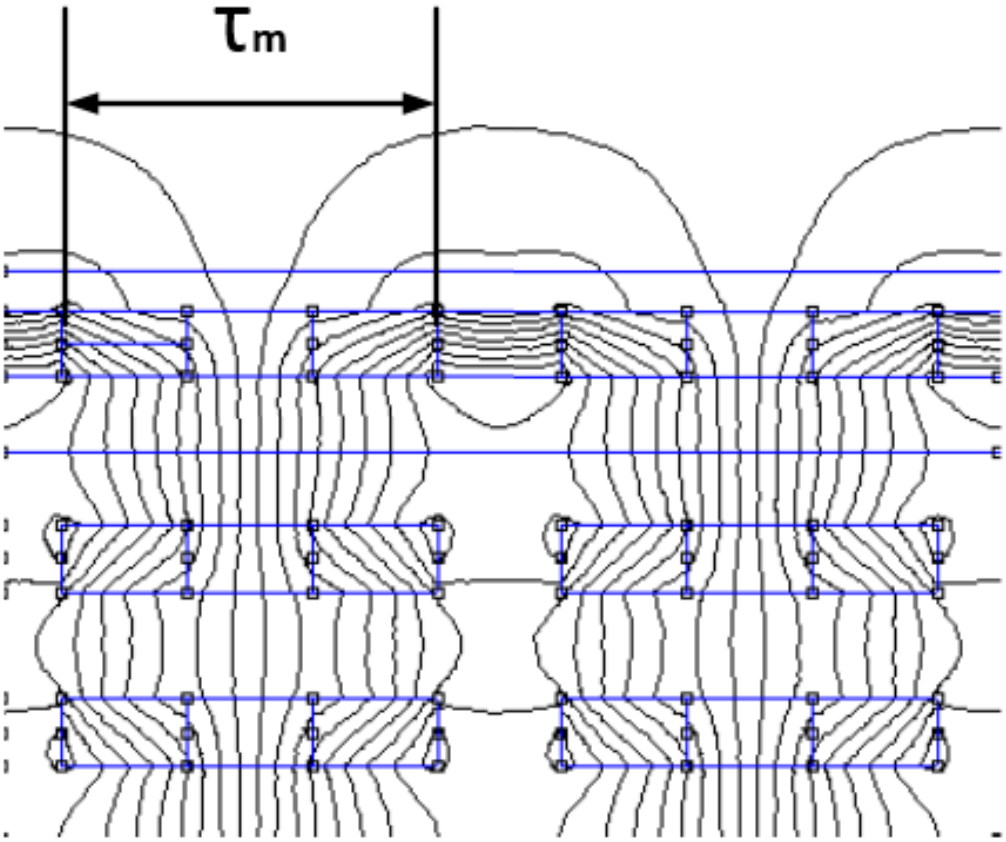

Figure 4.17: Magnetic Flux lines of a linear C-GEN 25 kW Halbach Concept

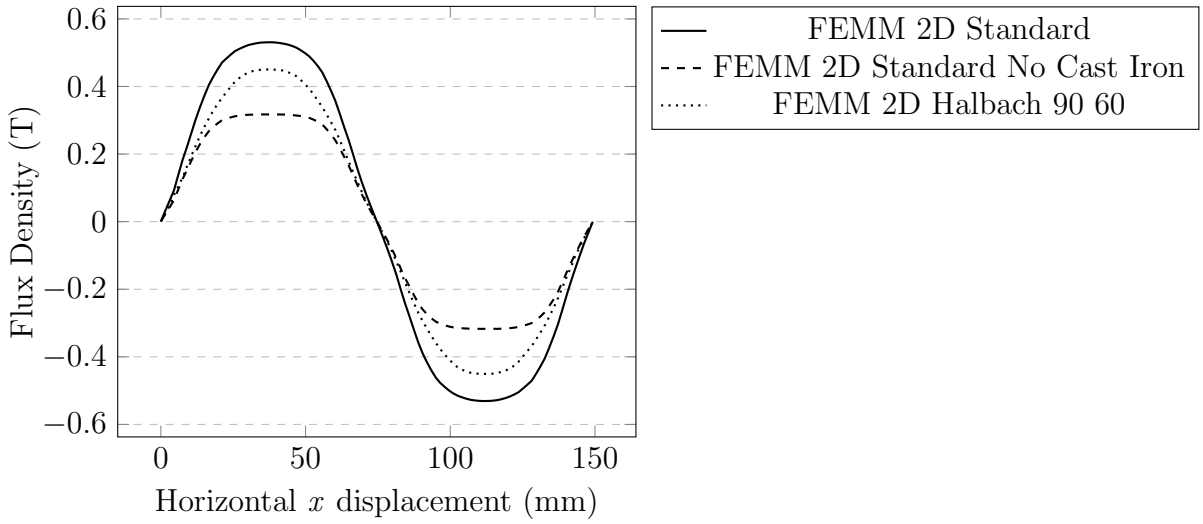

Figure 4.18: Perpendicular field values along the x axis for the Case Study Models

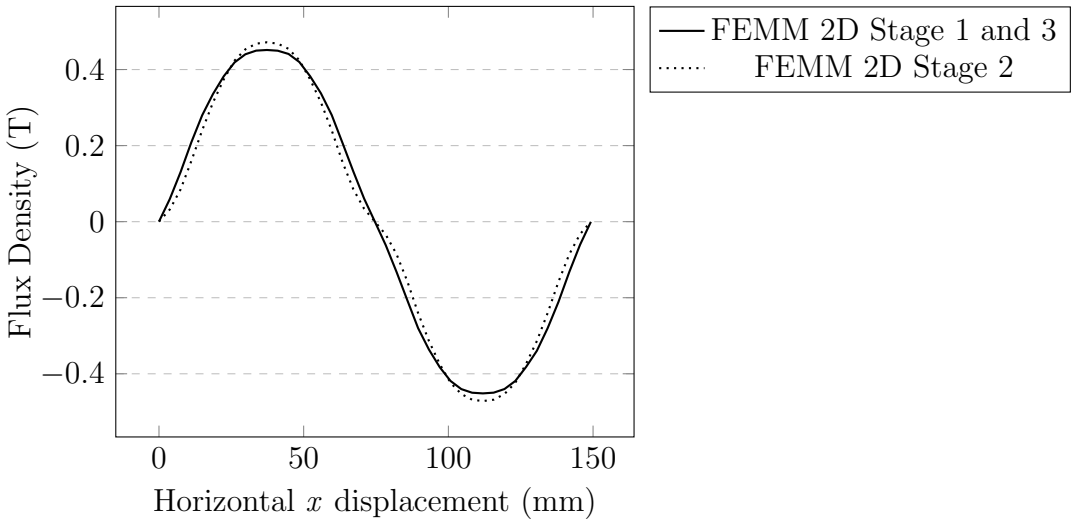

Figure 4.19: Perpendicular field values along the x axis for the Individual Stages of the Halbach Model

Figure 4.20 shows a comparison of the strong and weak-side field. The results fits in well with the literature, the field is not completely cancelled on the other side of the array. This phenomenon is well documented in[119] and it is due to the interference of the fields from the individual blocks. In this case for an $m = 8$ array at $g/2$ away from the array, the weak-side field is about 5 times less than the strong-side.

Figure 4.21 compares the perpendicular component of the analytical and FEMM Halbach models at an axial gap distance of $g/2$. The Halbach 2D curve was developed using Equation 4.12 and it is 10% over-predicted compared to the FEMM model. The double Halbach 2D equation relies on a geometry as seen in Figure 4.3, it can only be used as an approximation for each stage in a multi-stage topology. Additionally, the division of each pole into segments has resulted in more rectangular pieces than trapezoidal in the 3D analytical calculation and with the 2D FEMM analysis being carried out along the circumferential length of the pole at the active radius, this led to little or no difference between the modified 3D Thompson equation (See Equation 4.25) and the 2D FEMM model.

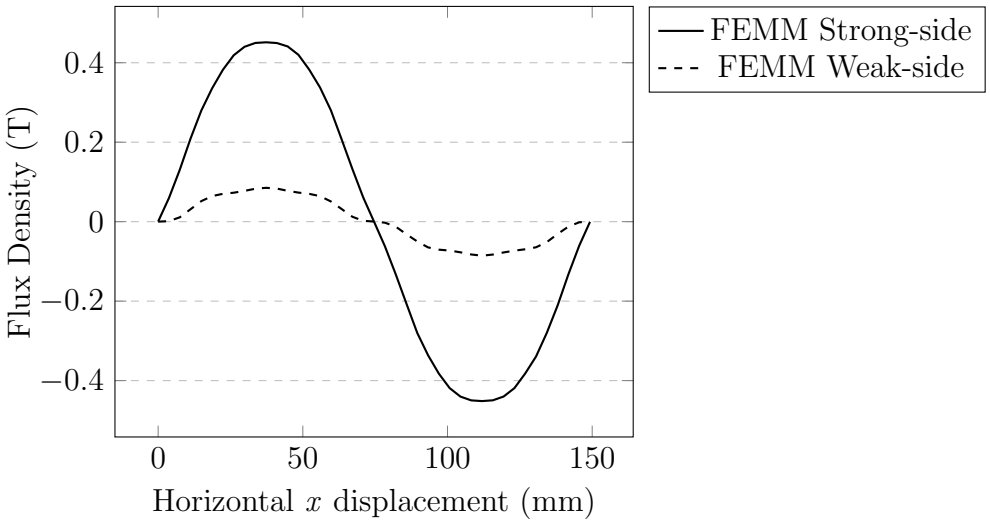

Figure 4.20: Perpendicular field values along the x axis at a distance $g/2$ from the strong-side and weak-side respectively

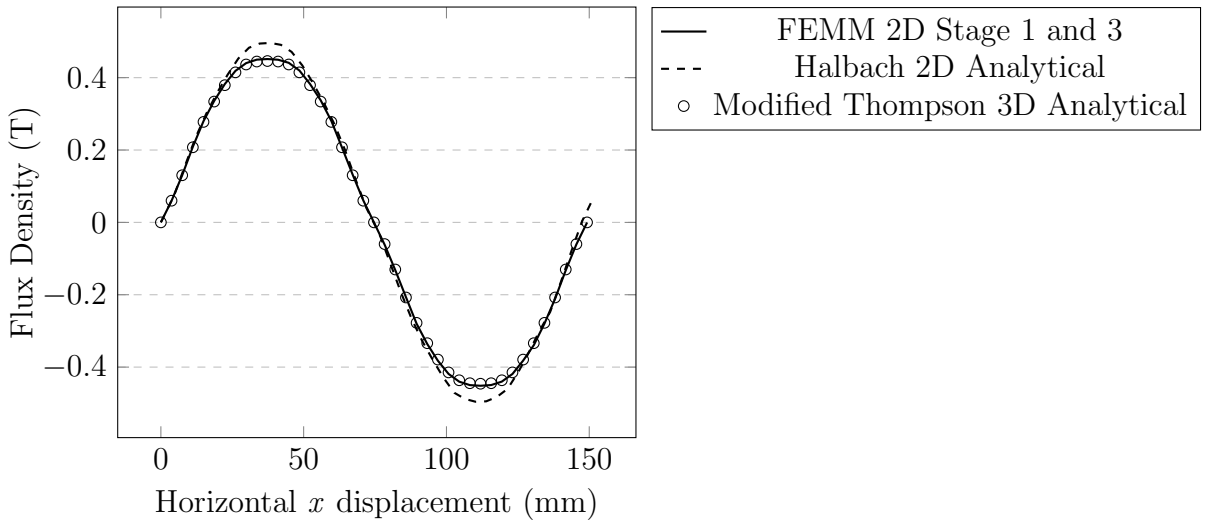

Figure 4.21: Results of the analytical expressions and equivalent FEMM models

In order to better understand the results presented above in more detail, it is worth revisiting Halbach's 2D theoretical expressions to better understand the impact of various parameters;

$$\mathbf{B}_y = 2B_r \sum_{i=0}^{\infty} \frac{\sin(n\pi/m)}{n\pi/m} \left(1 - e^{-nkh}\right) e^{-n\pi g/\lambda} \cosh(nky) \cos(nkx) \tag{4.30}$$

$$\mathbf{B}_x = 2B_r \sum_{i=0}^{\infty} \frac{\sin(n\pi/m)}{n\pi/m} \left(1 - e^{-nkh}\right) e^{-n\pi g/\lambda} \sinh(nky) \sin(nkx) \tag{4.31}$$

If we assume that only the first harmonic makes a significant contribution ($n = 1$) which is a good approximation in practice, the above equations simplifies greatly on axis to the more commonly known Halbach 2D expressions;

$$\mathbf{B}_y = 2B_r \frac{\sin(\pi/m)}{\pi/m} \left(1 - e^{-kh}\right) e^{-\pi g/\lambda} \cos(kx) \tag{4.32}$$

$$\mathbf{B}_x = 0 \tag{4.33}$$

Utilizing Equation 4.32 above, Gieras et al and Clarke were able to perform quick and reasonably accurate analysis for understanding the optimal operating

variables for a double-sided coreless Halbach AFPM machine [51] [120]. A similar analysis is done here.

The most popular choice for m is 4 due to its simplicity. Nonetheless, for the reason mentioned earlier such as increased risk of demagnetisation [48], a search for a more optimised m was conducted. It is clear from Equation 4.32 as m tends to ∞, the vertical field becomes more sinusoidal and approximately 90% of the theoretical limit is achieved. Figure 4.22 shows the relationship between the relative vertical field and m for the C-GEN 25 kW Halbach Concept. The use of an $m = 8$ array, leads to a higher peak magnetic field than the $m = 4$ and produces a more harmonic-free magnetic field as seen in the case study. Although, an $m = 8$ array would be more expensive to obtain due to the nature of polarization, but for this exercise it is deemed necessary to achieve the desired peak.

Finally, the thickness of PM, h, can be designed to be equal to half the wavelength, λ which is typical for undulators [61]. This means the air gap flux density will achieve 95% of theoretical limit (See Figure 4.23), and hence, better power and torque. However, the goal is not just to maximize the torque, but to maximize the torque density. So increasing the magnet thickness would increase the flux density, but also increase the mass. Therefore, it was decided to keep the ratio $h/\lambda \approx 0.07$ (See Figure 4.23) for the 25 kW C-GEN Halbach Concept.

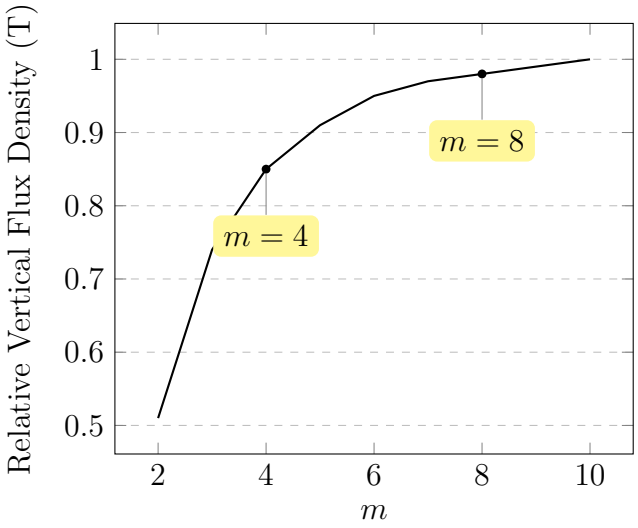

Figure 4.22: Relative Vertical Flux Density, B_y against m

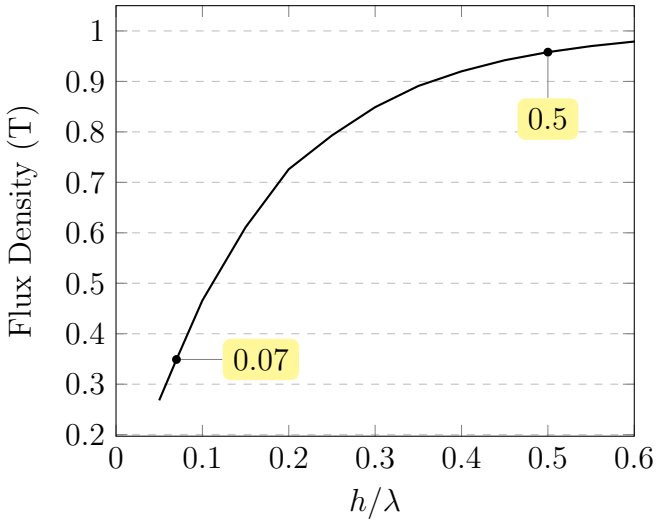

Figure 4.23: Relative Vertical Flux Density, B_y against h/λ

4.3 Conclusion

This chapter presents an overview of the relevant Maxwell equations in order to understand the following analysis. Two common techniques were presented in the development of the magnetic equation and not one more complex than the other, the choice of the technique to be used seems to be merely out of preference unless more complex structures present themselves. The expressions established by Halbach are particularly limited to rectangular magnets and they can only be used as an approximation for a multi-stage machine. Therefore, further formulas were developed via expressions established by Thompson to cover various combination of Halbach arrray as well as the trapezoidal shape found in AFPM generators. This technique wasn't found to be without fault but for the purpose of this undertaking, it is sufficient.

In the absence of cast iron, the numerical computation of the magnetic field was made easy by the integration of Biot-Savart Law. Simple Numerical Methods based on the current sheet or surface charge model were developed and the total field evaluated by the linear sum of the field produced by each block. This is particularly simple and efficient for simple shapes. However, there are limitations and assumptions to the above analysis which are detailed in the next chapters

and hence, 3D FEA commercial software such as Infolytica MagNet and Altair FLUX3D was used to validate the accuracy of the numerical methods and assess other relevant parameters including torque, power breakdown and efficiency.

Chapter 5

C-GEN 3D Finite Element Analysis and Numerical Validation

As documented in Section 2.1 of the literature review, Halbach arrays can significantly improve the performance of any PM generator with the main advantage being the improvements in torque carrying-capability and back voltage quality at the cost of the extra mass associated with the high mass density values of PM material. In order to investigate and compare the advantages and disadvantages of implementing such a technology when applied to the C-GEN machine, an investigative study is carried out.

Two machines are analysed in this chapter, a 25 kW and 1 MW Air-Cored Axial Flux C-GEN Generator. The axial topology lends itself to a great deal of modularity and stackability as outlined in Section 3.2 of C-GEN history. Furthermore, due to the availability of data and resources on these machines which is necessary for FEA modelling, they are considered the best candidates for a comparative study.

5.1 Design Methodology

In chapter 4, we looked at analytical methods and 2D FEMM models (which is basically the generator unwrapped circumferentially along the mean radius) for the computation of the magnetic field of the C-GEN axial flux machine. Notwithstanding, these techniques have limitations which are outlined below; [121] [51];

- The magnetic field solution is a function of radial position. It varies with the radius of the cylindrical cutting plane chosen for the 2-D analysis. This

needs to be taken into consideration when computing flux linkage and back EMF and current in nearby stator windings.

- The leakage flux at the inner and outer radius cannot be accounted for. In practice, there is a considerable reduction of the effective flux. Therefore, if high computational accuracy and a rigorous analysis is demanded, a 3D FEM analysis is needed.
- 2-D analysis can be limited when there are changes in material properties in different areas. For example in situations where you have PM's, Coils and Iron.

5.1.1 FEA Geometric Description

The boundary condition, choice of solver, total number of elements, and computational accuracy should be considered in FEA modelling, more on this will be discussed later. A typical flowchart of the tasks undertaken when modelling electrical machines is presented in Figure 5.1. A geometrical model is assigned excitation and boundary conditions where possible. After the model is solved, field plots and numerical results can then be viewed. The mesh can be modified after the initial meshing process to improve the solution accuracy. The general arrangement of the multi-stage flux topology is shown in Figure 5.2. There are separate stator windings (brown) sandwiched between magnets of opposing polarity. The permanent magnets are mounted on the surface of the rotor plates either in cast sized pockets to accept and locate the magnet pieces or held in places with glue or non-conductive materials added to the sides of the magnets via screws (not shown in diagram). The entire rotor structure can be cast as in the 25 kW generator or each rotor plate constructed individually and separated by spacers which was adopted in the 1 MW. Each stator plate consists of air-cored non-overlapping concentrated windings which are encapsulated in epoxy resin for mechanical strength and is secured together by means of a stator coil support. Some of the benefits of having non-overlapping concentrated windings include shorter end turns, simpler winding, higher packing factor and modularity in stator structure making it suitable for AFPM machines, especially ones with large pole numbers [122] [123].

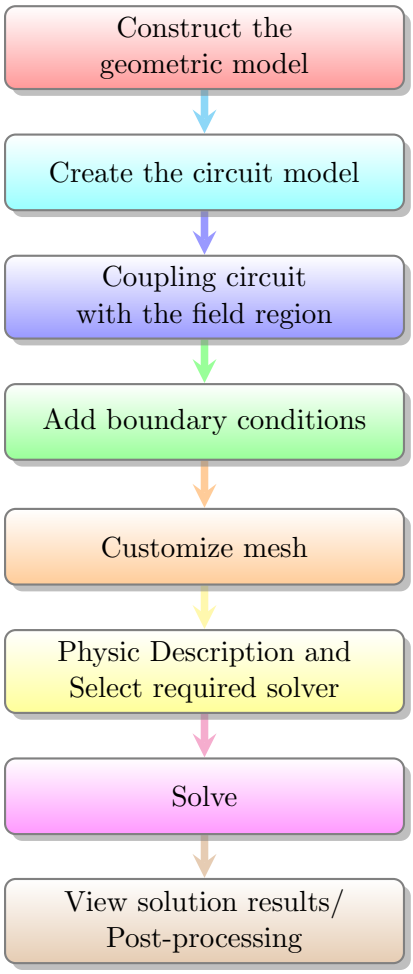

Figure 5.1: Typical Modelling Flowchart for Electrical Machines

Figure 5.2 is a simplified model used for the FEA analysis, very accurate representation of the geometry of the prototypes is complicated. In reality the rotor is made up of a number of mechanical support features such as spacers, bolts, ribs which can be taken into consideration in a more detailed study. A realistic view of the 25 kW and 1 MW C-GEN generators with technical drawings was provided by NGenTec Ltd and these can be seen in Appendix A.1, A.2 and B.1, B.2 respectively. Nevertheless, the principal flux components (highlighted by Paths A and B) that determine the machine performance are handled, along with the limitations of the analytical methods which were detailed earlier.

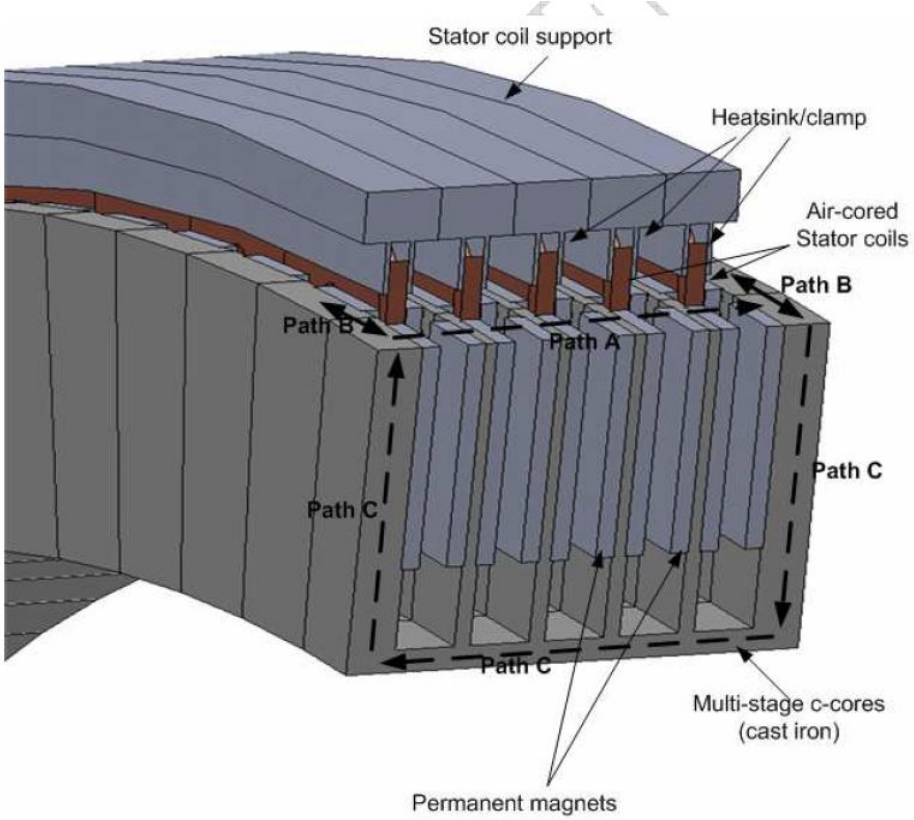

Figure 5.2: Structure of multi-stage axial C-GEN (Image modified from [88])

5.1.2 What is an appropriate Mesh?

Due to the multi-physics nature of the C-GEN prototypes, three core disciplines were identified; Electromagnetic, Thermal and Structural. Under these, various calculations are possible such as electromagnetic characteristics, temperature distribution, structural stress, vibration noise and coupled performances of electrical machines [124]. A typical electromagnetic-thermal flow chart process can be seen in Figure 5.3 and with the advent of 3D Computer-Aided Engineering (CAE) software, key parameters including back EMF, efficiency, torque and losses can be accurately determined. A great deal of emphasis is placed on the electromagnetic-thermal analysis, as this is where the author makes most of the improvements discussed in the following sections.

A slew of FE models were developed in-house either by NGenTec engineers or in collaboration with external companies such as Motor Design Ltd and Motor Engineer during the development of the 25 kW and 1MW prototype [126] [127]. This involved detailed 3D structural and CFD modelling and utilising results

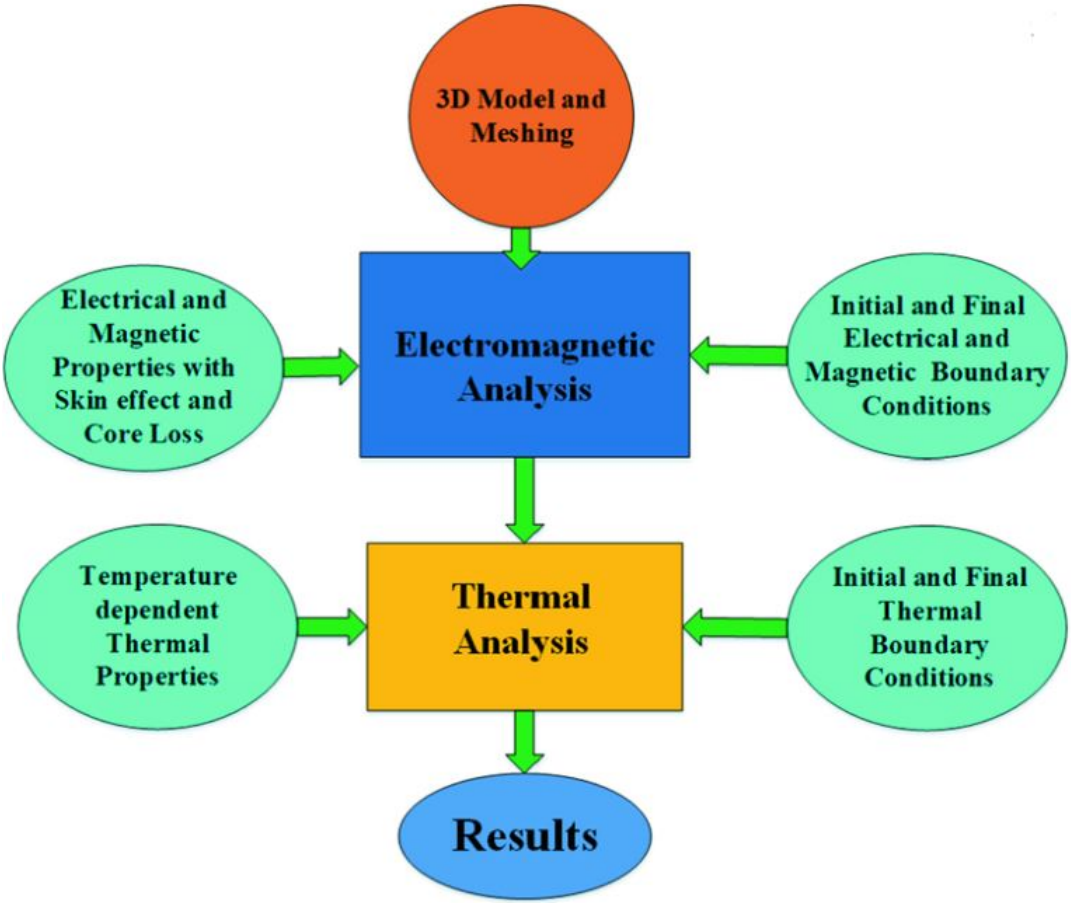

Figure 5.3: Electromagnetic Transient-Thermal Modelling Flow Chart (Image taken from [125])

of loss distribution and fault torques from detailed electromagnetic modelling to build up confidence in the overall design before committing to manufacturing [87].

It is a desire to achieve high levels of accuracy when using FEA software to predict the real-world behaviour of electrical machines. A good understanding of the physics of the system such as required material properties, boundaries and applied loads is necessary [128]. The results of FEA model is highly dependent on the quality of the finite element mesh that is used. Using finer elements will improve the accuracy of the simulation results by capturing areas in greater detail. At the same time fine meshes are more computationally expensive requiring increase memory and CPU time. The goal is to strike a balance between accuracy and computing time.

Typically, when solving simple problems with known analytical solutions, FEA

analysis can be conducted by varying mesh density and comparing the results to the known solution to arrive at some error value. Unfortunately, in reality at times we are dealing with complicated engineering problems and the solution can be quite unknown [128]. Usually, what happens in such cases is the result is approximated by varying the mesh density of the FEA model based on three best practices;

1. Carry out desired analysis with coarse mesh and solve.
2. If the results change within a certain percentage, the mesh is converged, otherwise, repeat. Often there can be mesh irregularities in certain regions especially when dealing with complicated geometry, it is worth adjusting the mesh in those areas and solving again.
3. At each stage of meshing, a collection of data is gathered. Asides from the results, the number of nodes, element size and computational time are noted, which is then used to inform the subsequent mesh process.

It can be tricky balancing accuracy and computational time when dealing with finite element meshing. An intermediary practice to obtain useful results without sacrificing heavily on computational time involves defining a finer mesh in regions that are of more interest, whilst accepting a higher error in locations of less importance. This technique can be quite handy especially when time and computational resources are limited but a good understanding of the problem and experience is necessary.

The approach detailed above was employed in the 3D FEA modelling of the Standard C-GEN 25 kW and 1 MW prototype by NGenTec Ltd. It was found that the numerical modelling and experimental results were in close agreement providing confidence in the detailed electromagnetic, structural and CFD work done. Therefore, it was these FE models the author relied upon to provide a baseline for the mesh development in the proposed Halbach models. This is discussed further in the next section.

5.2 3D C-GEN 25 kW Models

The geometry and the mesh and also the physical description of the 25 kW models are presented. As mentioned earlier to improve accuracy of the results and reduce computational time, only $1/8^{th}$ of the machine is modelled. Therefore, in the case of a 4 stage and 32 pole and 24 coil C-GEN generator, only 3 coils and 4 poles are represented per stage. The detailed figures and dimensions that supported the modelling process can be seen in Appendix E.1.

Figure 5.4(a) shows the Standard 3D finite element model developed by Echenique [129] using commercial software, Vector Fields Cobham. Below this we have the Halbach 90 60 model designed by the author using an alternate package, Infolytica MagNet (Mentor Graphics). MagNet was chosen as the software of choice in this case due to past user experience and better mesh controllability. Siemens Mentor Graphics offer a suite of resources and support which was relied upon for the effective 3D FEA modelling [130].

The complete field area for the 3D Halbach 90 60 model can be seen in Figure 5.5. It includes the rotor permanent magnets, air regions, coils, air boxes and an even periodic boundary condition assigned to the faces of the air boxes and regions in the direction of rotation. Even periodic boundary condition is suitable for modelling machines that have an even number of poles. The mesh nodes on one side of symmetry are matched up to the mesh nodes on the other side.

The armature windings consist of several wound turns, and hence a stranded coil type is used for the modelling of the coils. This implies a uniform distribution of turns over the cross-section of the coil block profile, in series and insulated from each other. It also precludes the calculation of induced eddy currents. Nevertheless, the eddy current losses in the windings at the rated speed (100 rpm) were found to be very low [98]. Furthermore, coils can be represented in the finite elements domain as meshed (Figure 5.4(b)) or non-meshed coils (Figure 5.4(a)). The latter is simply superposed to the mesh at post-processing with each coil block represented inside and outside the study domain and the magnetic field created by the distribution of current is computed analytically by Biot Savart formula. The main advantage of this is a significant reduction of the number of nodes. Typically, if the flux is concentrated in the air gap, it is necessary to improve the mesh around the non-meshed coils. Otherwise, it is suggested to use meshed coils [131]. It was chosen to use meshed coils for overall mesh controllability.

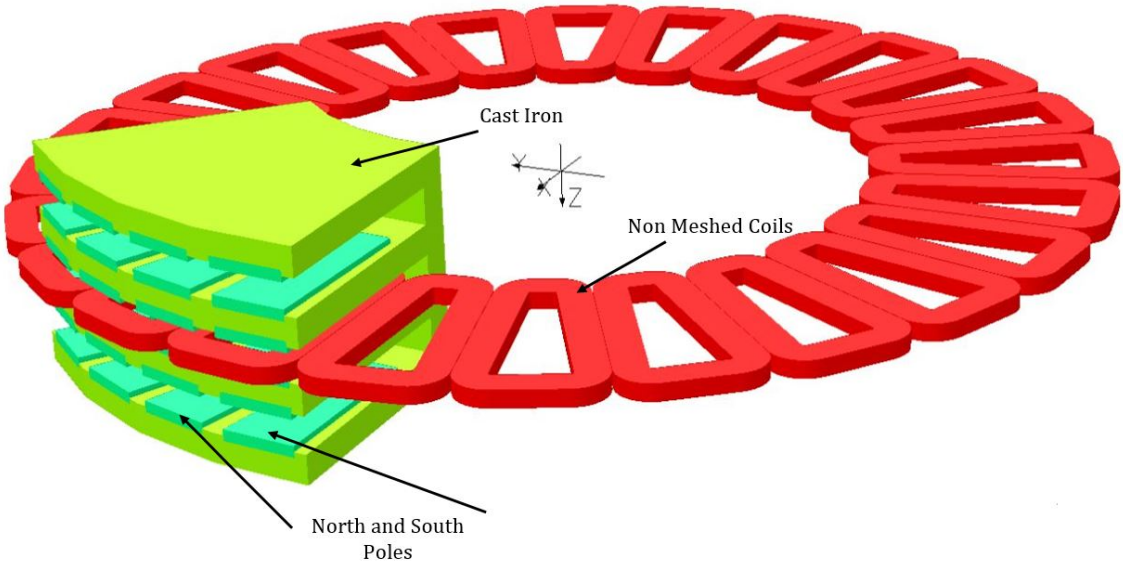

(a) Standard (Opera) (Image modified from [129])

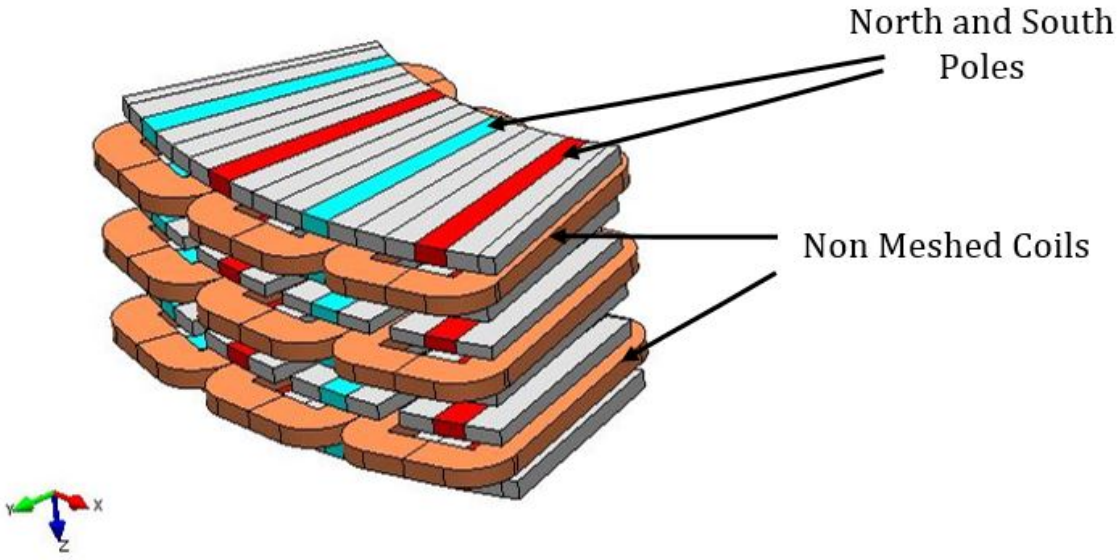

(b) Halbach 90 60 (MagNet)

Figure 5.4: Geometrical Models for the 25 kW C-GEN Prototype

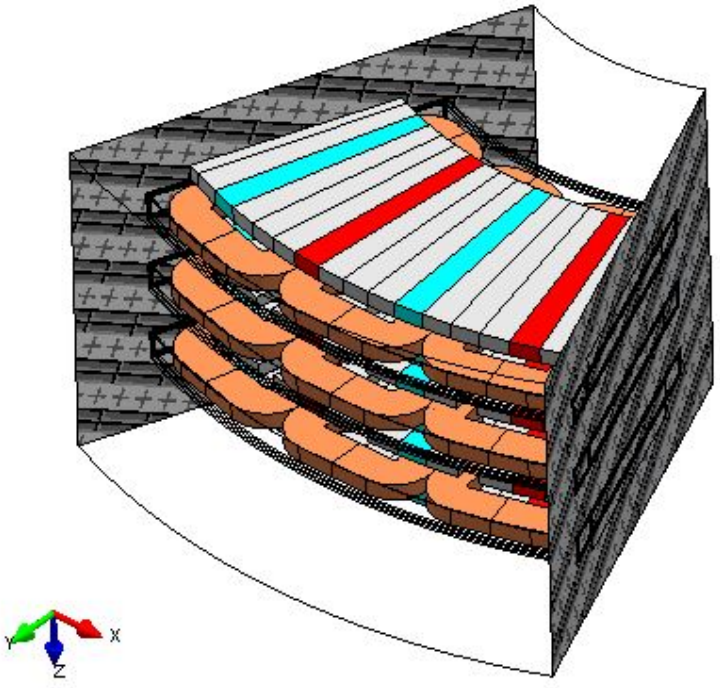

Figure 5.5: The Complete Field Region of the Halbach 90 60 Model

The 3D transient motion solver with an external circuit coupling was used for assessing the magnetic and kinematics aspects of the problem. The movable part of the device is driven at an imposed constant angular velocity with respect to the stationary part. It allows the study of the phenomena created by the time variable magnetic field generated by the permanent magnets. The principal results that can be obtained from such an analysis includes electromagnetic torque, Joules losses and induced eddy currents in conducting regions.

The 3D finite element MagNet model is comprised of tetrahedralshaped elements which are made up of nodes with four vertices. It is within these elements we find the vector fields represented by a polynomial with unknown coefficients. The finite element analysis is the solution of the set of equations for the unknown coefficients [130]. It is well established the accuracy of the solution is tied in with the nature of the field and the size of mesh elements. Therefore, regions where the magnitude and direction of field change rapidly require a refined mesh [132]. It is on this principle the air gap of the model is designed.

There are three requirements in the treatment of the air gap region for accurate machine analysis and calculations in MagNet, and these are detailed below [133];

- The air gap region between the stationary and moving parts must be split into two volumes which are further divided to form re-mesh regions as shown in Figure 5.6) culminating in four layers.
- The layers closest to the stator and rotor are assigned “VIRTUAL AIR”.
- The other two layers are assigned “AIR”.

This is necessary to have a sufficiently refined mesh in these regions for accurate computation of force and torque. As long as these steps are followed, MagNet will evaluate the field in the layer of “AIR” rather than the field near sharp corners which can be prone to error [133]. Figure 5.7 shows the mesh for the air gap of the Halbach model which can be considered to be well defined.

Figure 5.8(a) and (b) shows a comparison of the overall 3D mesh of the Standard and Halbach 90 60 model. The Standard C-GEN model was modelled with $1/16^{th}$ symmetry to enable a high concentration of mesh for the prediction of rotor losses. This model comprised of 1,516,822 elements and 432,882 nodes [129], whilst the Halbach 90 60 model albeit $1/8^{th}$ of symmetry consisted of 6,725,016 and 1,152,173 respectively which is considerably more. It is important to note, an AC steady-state analysis was conducted on the Standard C-GEN model [129], whilst this type of analysis is able take into account phenomena such as induced eddy currents, the transient with motion solver provides a more accurate analysis [130]. On an Intel(R) Xeon(R) CPU W3670 @ 3.20GHz 64 bits Processor Memory 24 GB, it took approximately 3 days for a transient analysis with motion for a given resistive load.

Figure 5.9 shows the flux density distribution of the Halbach 90 60 model with the direction vectors displayed via MagNet Modelling toolbox. A more close up view of the flux density distribution can be observed in Appendix D.1.

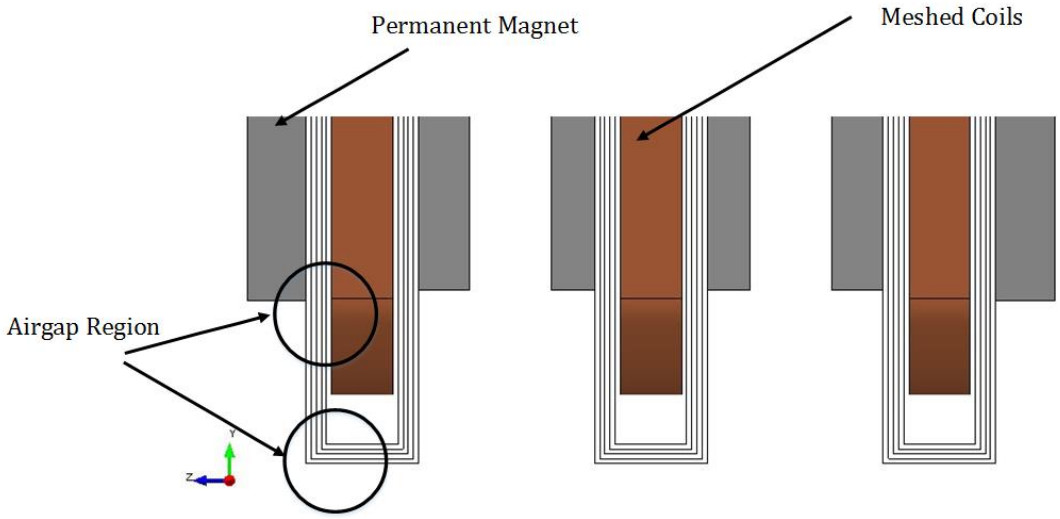

Figure 5.6: A close up view of the Air gap region of the Halbach 90 60 Model

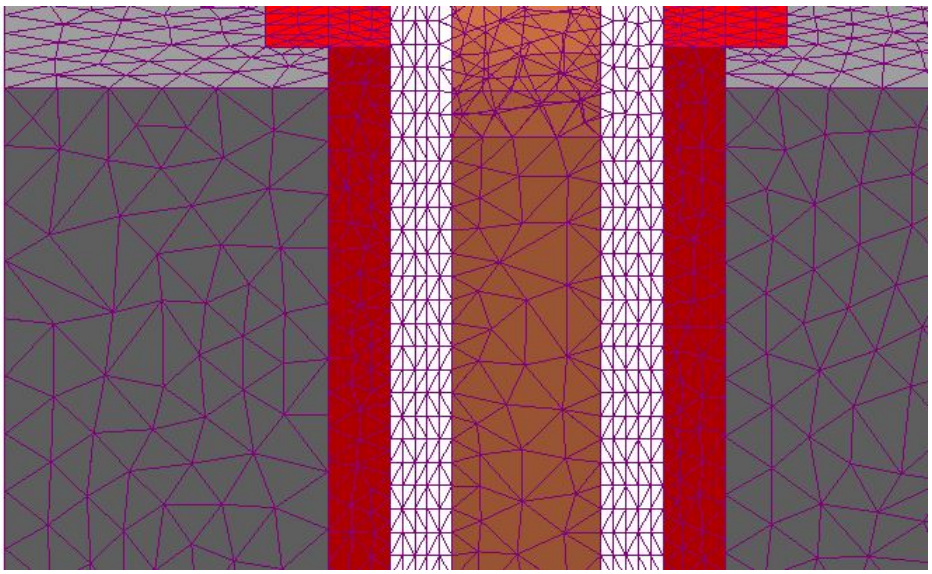

Figure 5.7: A close up view of the air gap mesh

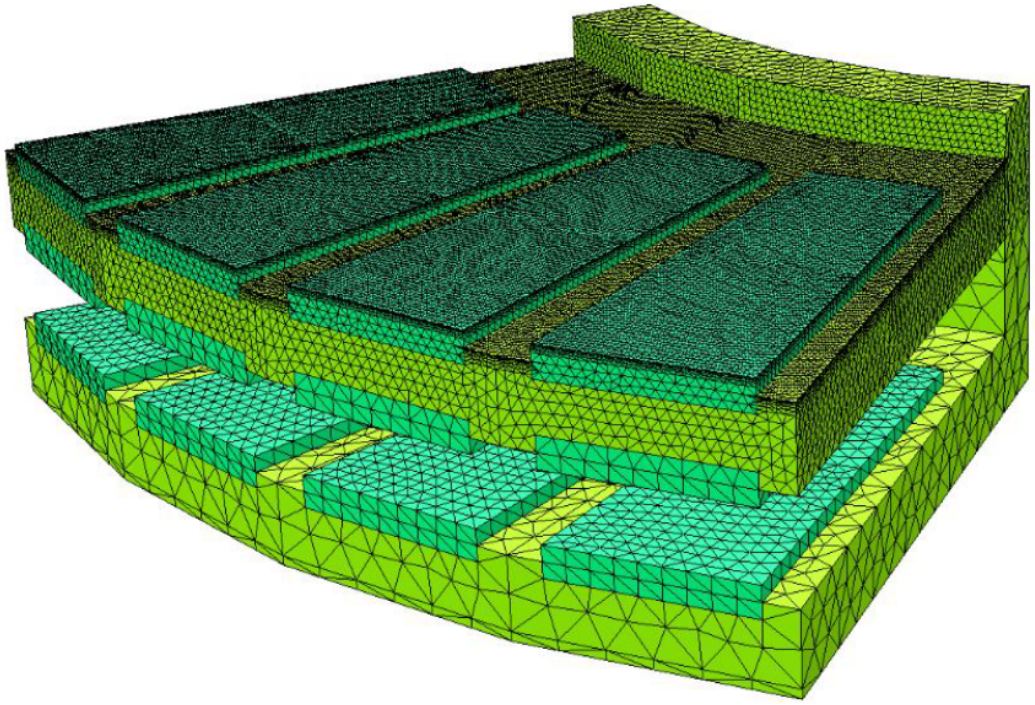

(a) Standard (Opera) (Image taken from [129])

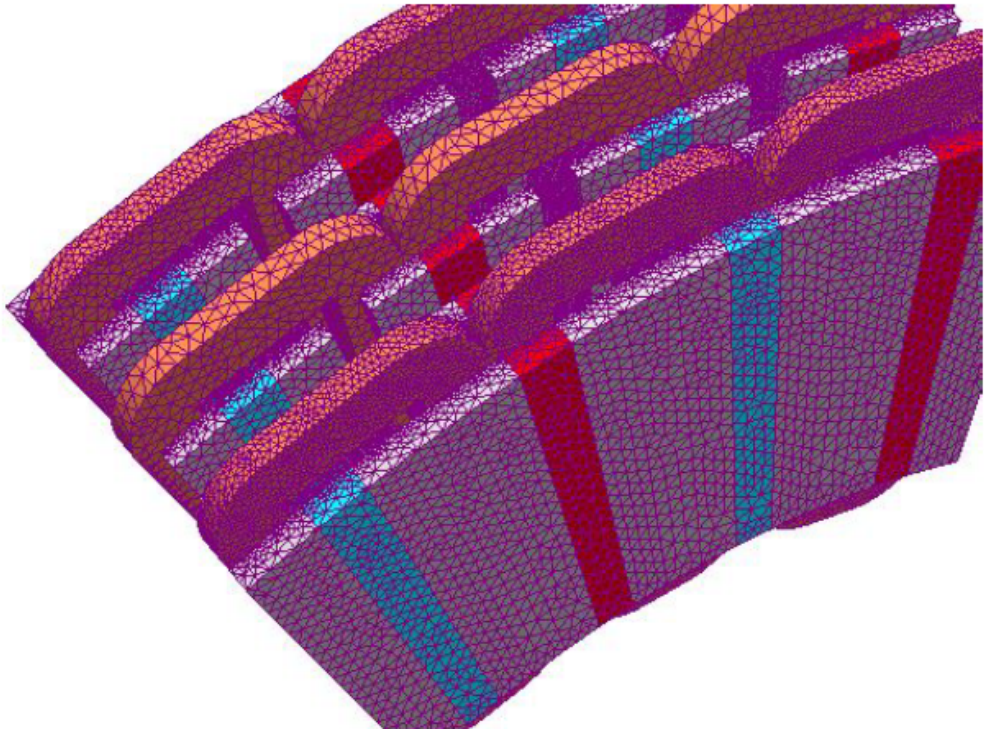

(b) Halbach 90 60 (MagNet)

Figure 5.8: A mesh comparison between the Standard C-GEN Model (Opera) and Halbach 90 60 (MagNet)

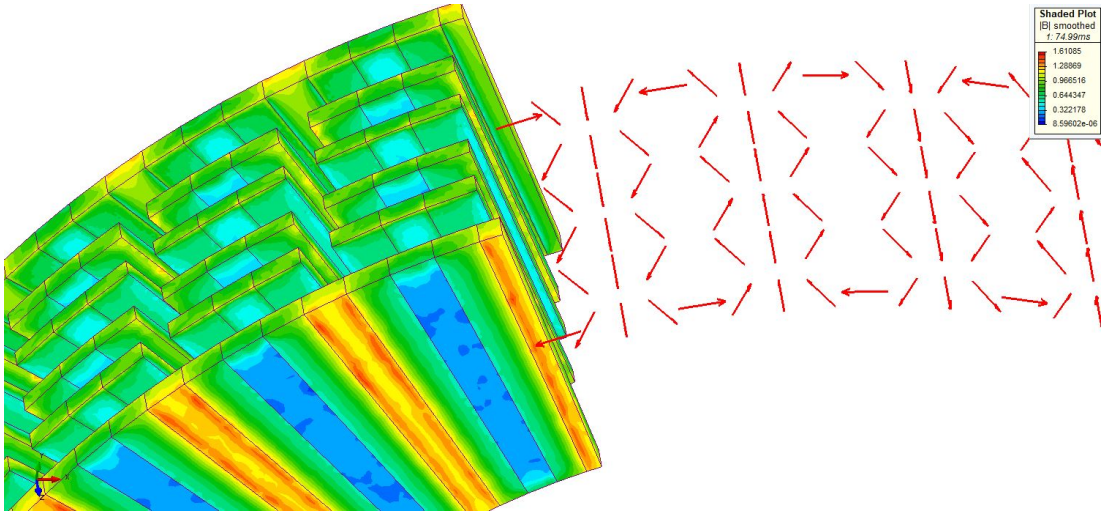

Figure 5.9: Flux Contours and Direction of PM Magnetisation of the Halbach 90 60 (MagNet)

5.2.1 3D C-GEN 25 kW Models Results and Discussion

The air gap flux density is a quantity of significant interest in the design of any electrical machine, both as a function of position and in terms of its harmonic content. Therefore, the following analysis starts off with this. A combination of the investigations carried out in [104] [48] was performed here. They were identified as the appropriate measures to ascertain the developed 3D analytical expressions and the performance of the Halbach [1] model.

A 3D Magnetostatic computation of the air gap flux density is carried out with only the PMs just as in the 2D FEA. This is sufficient as the armature reaction effect is expected to be weak since the C-GEN has a large effective air gap [134]. The field is probed at the mean plane of the stator windings (that is $z = 11mm$) in all cases and about the mean radius unless otherwise stated.

The modified 3D analytical expressions discussed in Chapter 4 were coded in Matlab and compared against the 3D FEA results. The distribution of B_z in Figure 5.10(c) determines primarily the generated back EMF, hence, the assessment of the air gap flux density is the main focus here.

The field components B_ϕ and B_r are responsible for eddy-circulating current in the windings and eddy current loss in the end-windings caused by end-winding flux linkages respectively [135] [136]. This is not accounted for in the present analysis, due to the choice of a stranded coil model, but can be included in a separate analysis. However, at the rated speed, the eddy current losses were found to be very low [98].

The plots presented in Figure 5.10 show a good agreement between the numerical and equivalent 3D FEA modelling of within 10 %, validating the Modified 3D Thompson Equation. It can be observed that the variation of B_z is larger when computed using 3D FEA (See Figure 5.10a and c), this is an unwanted side effect of the subtle changes made to the magnet dimensions to rectify the irregularities noticed in Figure 4.19. Asides from this, the results agree well with the literature;

- The dominant harmonic on the weak-side is the seventh, which is expected to decay away from the magnet surface [137].
- The field component B_z is a function of radial position [104].
- An $m = 8$ array results in a highly sinusoidal field as opposed to an $m = 4$ [48].

1. The word "Halbach" is used in place of "Halbach 90 60" from this point onwards for simplicity

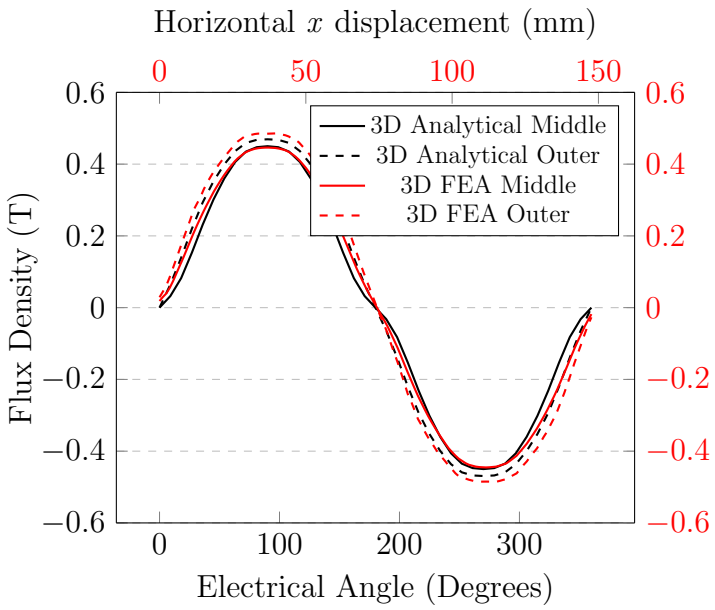

(a) Strong-side Airgap Flux Density

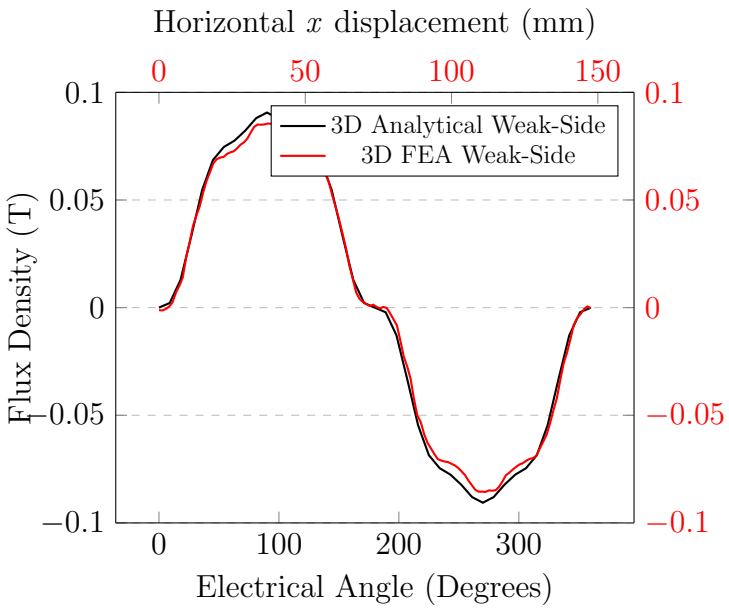

(b) Weak-side Airgap Flux Density

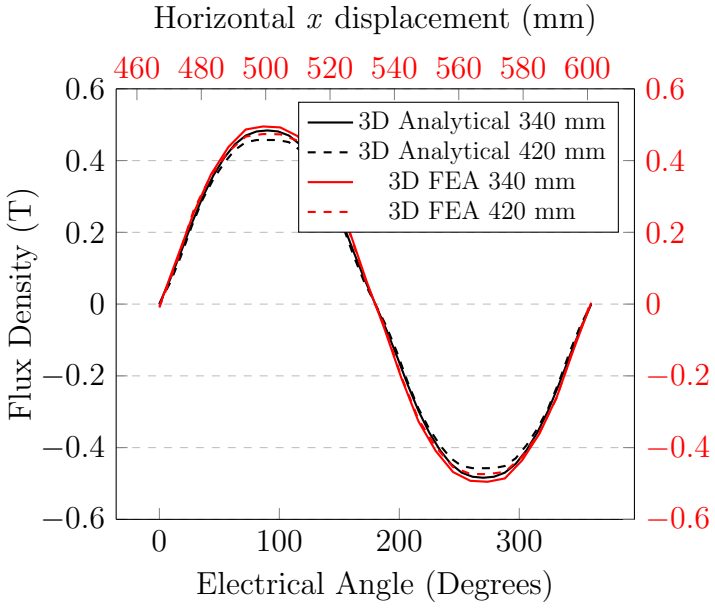

(c) Angular Dependence of B_z at the Outer Stage

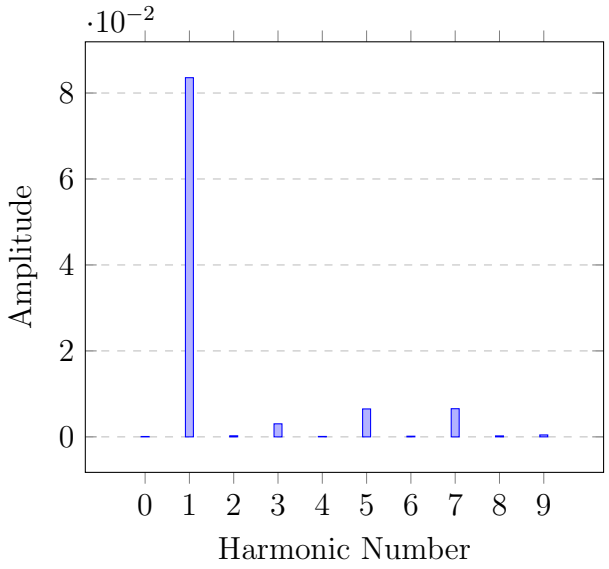

(b) FFT of Airgap Flux Density

Figure 5.10: Comparison of 3D FEA and Analytical Results of the air gap flux density

Following on from this, the performance of the generator supplying an isolated, three-phase star connected resistive load was computed with a time-stepped analysis and a coupled field-circuit. The Standard C-GEN was remodelled by the author in MagNet and the same analysis performed to arrive at a suitable resistive load for a 25 kW Output Power. The mesh description and main results from this analysis can be seen in Appendix C.1, C.2 and C.3 and additional results for the Halbach model are provided in Appendix D.2 and D.3.

Table 5.1 shows the magnetic and thermal properties used in the 3D FEA modelling. At elevated temperatures, the various properties of the materials will change based on the coefficients and thus the performance of the generator will be affected. Since I^2R loss is the dominant loss in this machine, more emphasis is placed on this. Some information is provided below regarding the losses in the PMs and copper but for a more thorough power distribution see [129], [98].

The power balance inside the C-GEN is described by;

$$P_M - P_E = P_{LOSS} \tag{5.1}$$

where P_M is the input mechanical power, P_E is the output electrical power and P_{LOSS} is the power loss.

Therefore, if we ignore mechanical losses (bearing and windage) which is a reasonable assumption for low speed direct-drive topologies, the breakdown of losses in a Halbach air-cored machine with a non-ferromagnetic backing plate can be expressed as;

$$P_{LOSS} = P_{CU} + P_{PM} \tag{5.2}$$

where P_{PM} is the induced eddy current losses from the asynchronous space harmonics in the air gap MMF distribution caused by the non-overlapped windings [138].

In 3D FEA analysis, I^2R losses are readily computed by Joule effect in the coils, whilst the resistive losses of the induced eddy currents can be evaluated by a 3D direct computation of the electric current density in the volume as shown below [139];

$$P_{PM} = \frac{1}{\sigma} \int_{vol} J^2 \cdot dV \tag{5.3}$$

where J is the electric current density and σ is the electrical conductivity of the material of the body.

This technique has been shown to yield the most reliable results, even when computing eddy current losses in the rotor compared to traditional methods [139]. Bearing in mind a finer mesh is required in regions with skin effect, typically, 2-3 mesh layers based on experience.

	Copper	Magnet	Units
Electrical Resistivity, ρ (@ 20 °C)	1.72 e-8	1.40 e-8	Ohm.m
Temperature Coefficient, α (@ 20 °C)	0.0039	-0.0011	/°C
Remanent Flux Density (@ 20 °C)		1.21	T
Temperature rise above ambient on Load	56	30	°C

Table 5.1: Infolytica MagNet Key Material Parameters for Transient Analysis

Figure 5.11 shows a comparison of the Standard and Halbach models in terms of the air gap flux density, load voltage and electromagnetic torque. The computed air gap flux density and load voltage in the individual stages of the Halbach model underperform when compared to that of the Standard model and this is further translated in its torque carrying capabilities. An FFT analysis of the air gap flux density shows a considerable drop of approximately 16% of the fundamental harmonic in the middle stage. Other harmonics are negligible owing to the large physical air gap.

Table 5.1 summarizes the main performance parameters of the two models. The use of a non-ferromagnetic core in the Halbach model has reduced the overall active mass of the generator by 44.5%, although the total PM mass is increased by approximately 15%. The torque requirement of $2.5kNm$ is shown to be unachievable by the Halbach model within the constraints of the geometry and thermal conditions. However, there are positive factors which could warrant further investigation as a slight improvement of the quality of the air gap flux density (more sinusoidal) which results in a better mean torque and low ripple compared to the Standard model is noticed. The latter was a similar observation made by Galea.

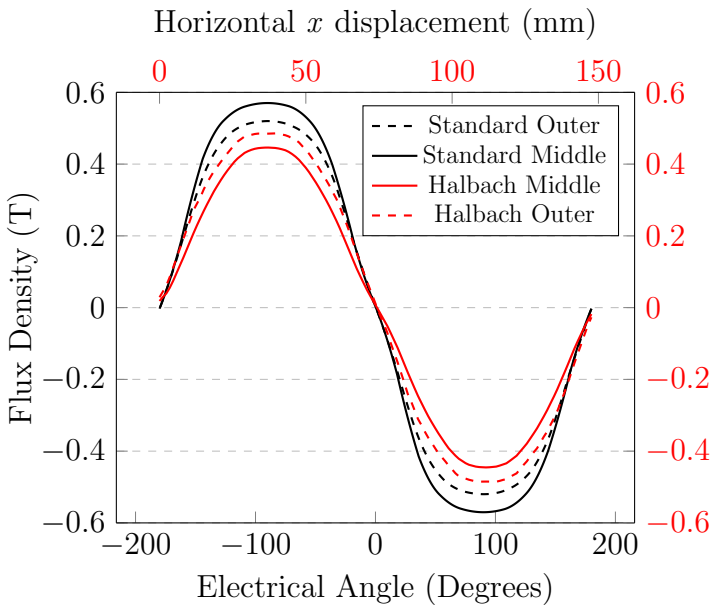

(a) Airgap Flux Density

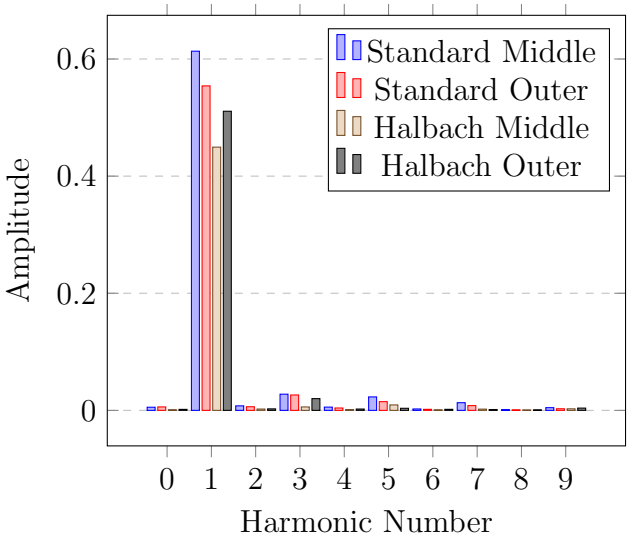

(b) FFT of Airgap Flux Density

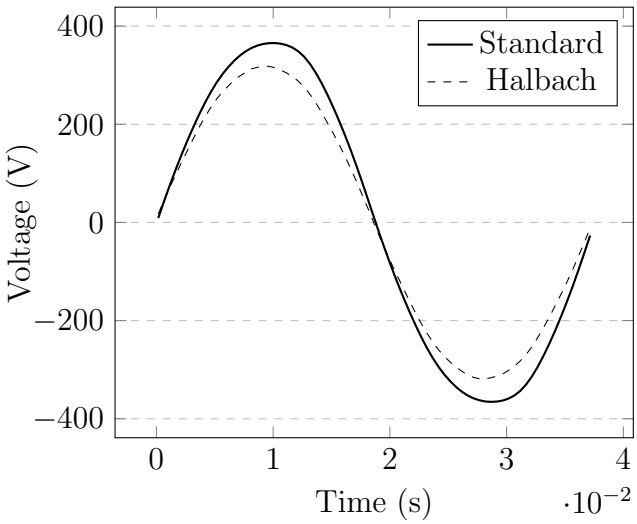

(c) Load Voltage

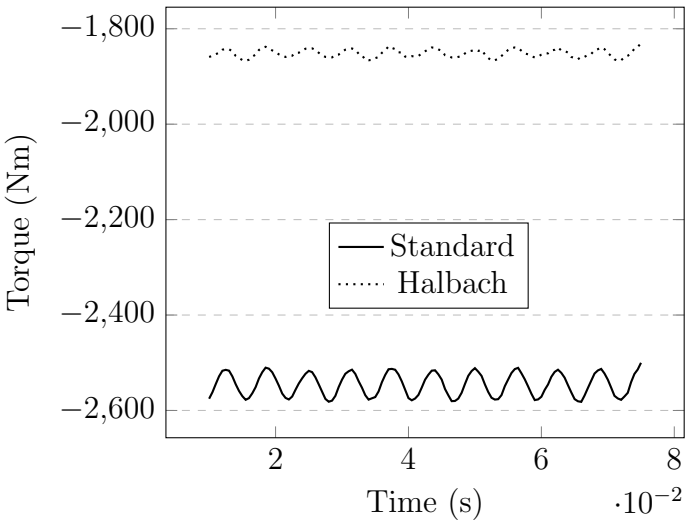

(d) Torque

Figure 5.11: Standard vs. Halbach performance Comparison

	Standard	Halbach	Units
Copper Loss	2	1.5	kW
Rotor Loss	100	25	W
PM Mass	129	152.8	kg
Overall Mass (Active Materials)	673.28	373.68	kg
Torque Density (Active Materials)	3.78	4.96	Nm/kg
Output Power	24.4	17.8	kW

Table 5.2: Standard vs. Halbach Key Comparisons

5.3 Demagnetisation Analysis

This section looks at the increased risk of demagnetization detailed in the literature, that is synonymous with the use of a Halbach array. It bears close resemblance to a study conducted by Galea [54], but applied to an axial flux multi-stage topology.

There are two types of rare-earth materials commonly used in electrical machines; Neodymium Iron Boron (NdFeB) and Samarium Cobalt (SmCo). A summary of the key properties can be seen in Table 5.3.

	SmCo	NdFeB
Remanent Field	0.5 to 0.85 T	1.1 to 1.5 T
Coercivity	600 to 800 kA/m	750 to 1000 kA/m
Relative Permeability	1.01 parallel, 1.04	1.05, 1.15
Temperature Coefficient	-0.04 /%°C	-0.11 /%°C
Max Energy Density	150 to 200 kJ/m^3	200 to 350 kJ/m^3
Max operating temperature	≈ 300°C	≈ 100°C
Comment	Brittle, easily damaged, better intrinsic radiation resistance, expensive	Less brittle but still liable to chip, easier to machine, expensive

Table 5.3: Comparison of characteristics of SmCo and NdFeB Magnets. Table taken from [120]

NdFeB magnets are generally preferred over SmCo because of their significant performance benefits. Its high $(BH)_{max}$ and B_r have allowed for the development of compact, torque and power dense electrical machines. Nonetheless, they are less brittle and are defined by a relatively low working temperature compared to

SmCo, the latter of which is the biggest concern especially at elevated temperature due to the risk of irreversible demagnetization. Permanent magnet materials are characterized by their demagnetization curves, such as those found in Figure 5.12. The operating point of the permanent magnet is defined by B_{PM} and H_{PM}. These quantities define a point on the demagnetization curve which is at the intersection of the magnet characteristics and the load-line establishing the working point of the magnet. If the working point in any part of the permanent magnet falls below the knee of the demagnetization curve, that part of the permanent magnet will be irreversibly demagnetized. Below are a list of some risky conditions [140];

- Over-temperature due to over load conditions or inadequate cooling.
- Inappropriate operating conditions such as three-phase short-circuit currents or even normal operation such as line starting.

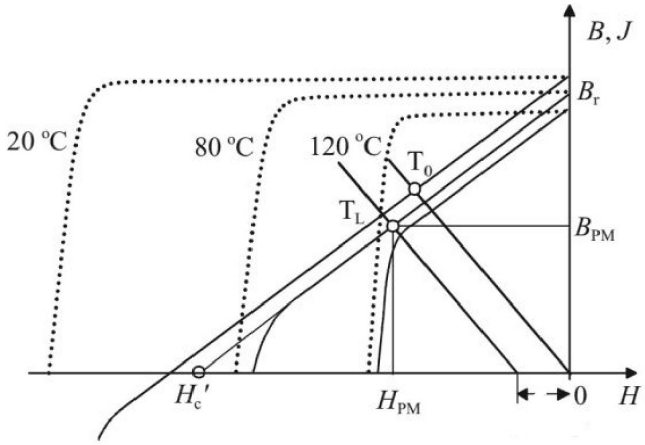

Figure 5.12: Typical Demagnetisation Curves of Rare-Earth Materials (Adapted from [140])

As detailed in the literature review, the proximity of a segment to another in a Halbach array, can lead to reverse fields which act by demagnetizing parts of the permanent magnets, even at no load. This can be made even worse under the conditions listed above [48]. In order to evaluate the risk of demagnetization solely due to segment proximity at elevated temperatures, a no-load analysis is carried out.

In [54] we see the manner at which we can reliably predict the extent of demagnetization and this is described in the expression below;

$$B_{prox} = B_{demag} - \underline{\boldsymbol{B}} \cdot \frac{\boldsymbol{M}}{M} \tag{5.4}$$

Where B_{prox} is the demagnetization prediction field, B_{demag} is the PM demagnetization value equivalent to the knee point on the curve, $\underline{\boldsymbol{M}}$ is the magnetisation vector and M is the norm of the vector $\underline{\boldsymbol{M}}$.

It then follows that the second term in the expression which is the total resulting magnetic field in the direction of magnetization, if it is greater than B_{demag}, then there is no risk of demagnetization resulting in a negative B_{prox}. Therefore, the more positive B_{prox} gets the greater the risk of demagnetization.

Figure 5.13 shows the demagnetization characteristics of the N35H used for a 3D demagnetization analysis of the Hablach model in Siemens MagNet, by employing a simple technique [141]. If B_{prox} is less than or equal to 0, indicating no risk of demagnetization, the demagnetization prediction is set 0 while if B_{prox} exceeds 0 then there is a risk of demagnetization and this region is set to 1 and highlighted in red. Figure 5.14 shows the demagnetization prediction for 80°C, 100°C and 120°C temperatures from left to right. It is observed that this arrangement does perform reasonably well against proximity demagnetization, it is only when you approach relatively high temperatures it begins to suffer significantly, mostly around the axial PMs at the end stages emphasizing the importance of adequate safety measures and redundancies against the risky conditions highlighted earlier.

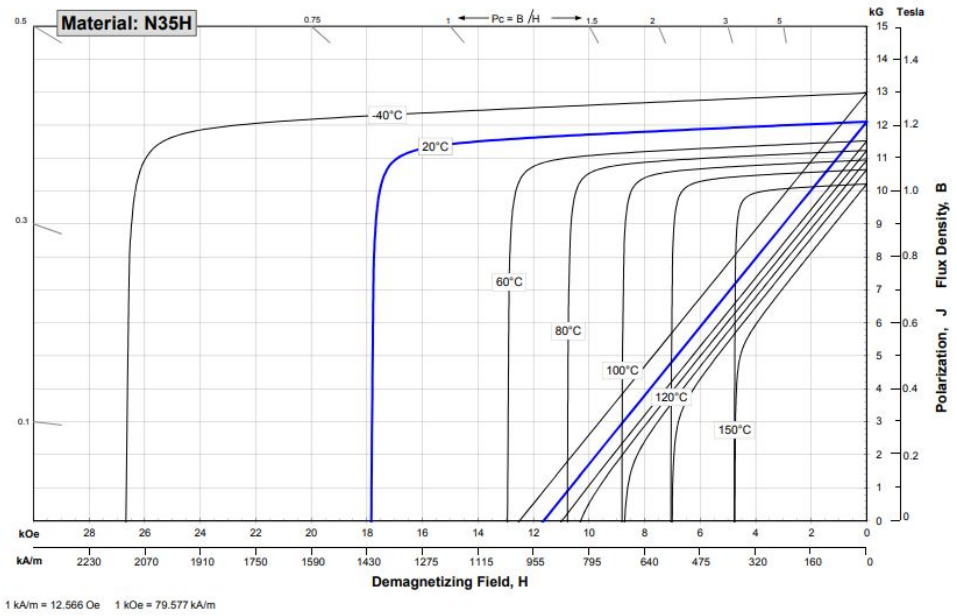

Figure 5.13: N35H Demagnetisation Curves (Image taken from Arnold Magnetic Technologies)

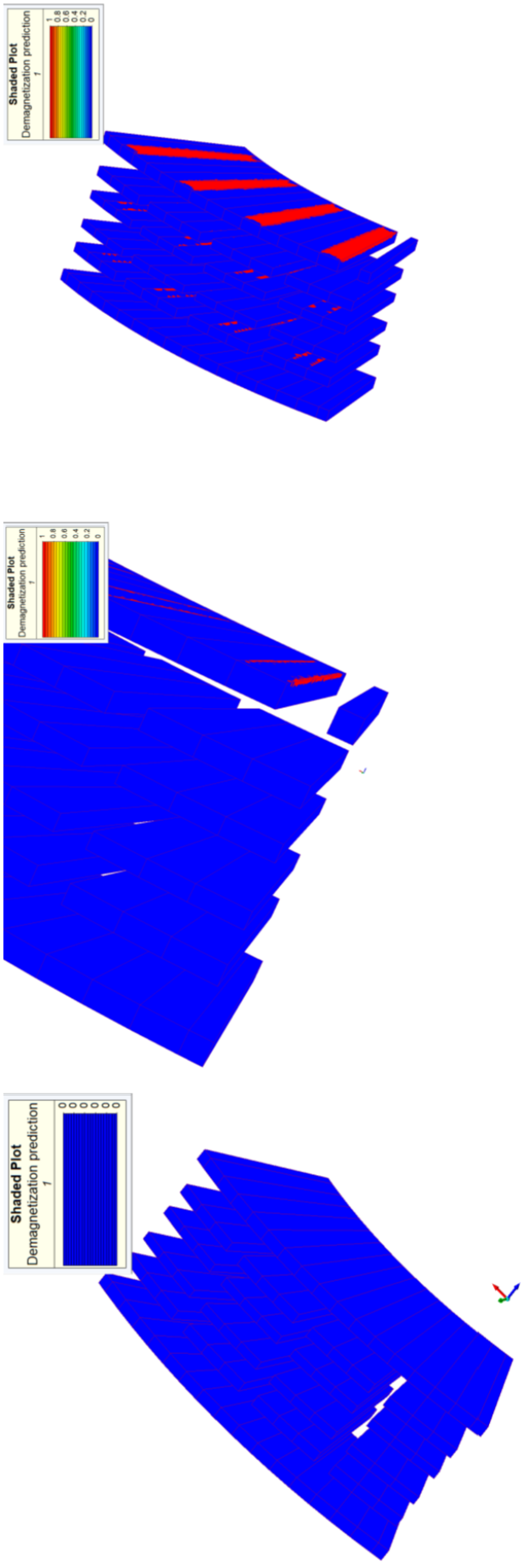

Figure 5.14: No-load demagnetization prediction at $80°C$, $100°C$ and $120°C$ respectively.

5.4 3D C-GEN 1 MW Models

5.4.1 3D C-GEN 1 MW Models Results and Discussion

A similar geometrical and meshing process as in the 25 kW is conducted here with some exceptions which will be detailed shortly. The final 1 MW prototype is a 4 stage, 176 pole and 44 coil C-GEN generator. The detailed figures and dimensions that supported the modelling process can be seen in Appendix E.1.

As mentioned earlier NGenTec collaborated with Motor Engineer to provide 3D FEA electromagnetic modelling using FLUX 3D to verify the in-house analytical design tool. Subsequently, experimental investigations were performed, which were found to be in good agreement with the analytical and FEA study conducted by Motor Engineer. Therefore, for the purpose of this undertaking it was decided to use the same 3D FEA models with some alterations to implement a 1 MW Halbach C-GEN version. This was identified by the author as a way of simplifying some of the rigorous meshing process detailed in Section 5.1.2 and to provide better confidence in the results.

Asides for the MW scale of this analysis, there are some points worth highlighting about the study conducted here;

- Each PM is of the same dimension unlike that of the 25 kW where adjustments were made to make the air gap flux density in the various stages more alike. Therefore, its is expected to have the same balance of voltage between the middle and end stages compared to the Standard 1 MW.
- Modelling of the stator plate: At the time of running the simulations for the 25 kW, not much was known regarding the materials properties of the stator plate and with the assumption that most of the flux is concentrated in the air gap, it was considered inconsequential to the electromagnetic study. For the sake of a thorough analysis the stator plate was included here.

The meshing process conducted by Motor Engineer for a five stage machine is illustrated in Appendix F.1, F.2 and F.3. The vector magnetic potential is computed at each node, therefore, the denser the mesh the more reliable the results which is why rather than representing the five stages in the finite domain, only a single stage is modelled with an improved mesh allowing for a better balance between accuracy and computational time. As the specifications and features of the 1 MW C-GEN changed during the course of the DECC project, a parametrized meshing process was employed by Motor Engineer using NetGen/NGSolve tools.

Due to the inconsistencies in the air gap flux density between the various stages noticed in 2D Halbach analysis, it was decided to model all four stages for the Halbach model with the mesh accuracy and detail used in the single stage Standard 1 MW done by Motor Engineer. In the absence of the final parametrized model, manual meshing techniques were adopted and the computational resources of Google Compute Engine was utilized to manage the increased demand for CPU processing power. See Appendix F.4 for the geometrical models, mesh description and flux contour plots.

The materials properties and mesh statistics of both models can be seen in Table 5.4 and 5.5 respectively. Unfortunately, the Halbach 4 Stages Model failed to meet the high expectation of mesh accuracy found in the Standard single stage model which may indicate unreliable results. A summary of the performance of both models can be seen in Table 5.6 and a comparison of the electromagnetic torque for different mesh description can be seen in Figure 5.15. Below are a few noteworthy statements;

- The single stage modelling applied in the Standard model resulted in fewer ripples due to numerical errors.
- The rotor losses (P_{PM}) in the Halbach model (not shown in the Table 5.6) were over-estimated. The high percentage of the number of mesh elements not evaluated (poorly connected elements) and the overall poor mesh statistics compared to the Standard single stage model could be a reason for this discrepancy.
- A better mean torque and low ripple is perceived in the Halbach model compared to the Standard which was also observed in the 25 kW Halbach analysis.

	Copper	Magnet	Aluminium	Units
Electrical Resistivity, ρ (@ 20°C)	1.72 e-8	1.40 e-8	2.65 e-8	Ohm.m
Temperature Coefficient, α (@ 20°C)	0.0039	-0.0011	0.004	°C
Remanent Flux Density (@ 20°C)		1.26		T
Temperature rise above ambient on Load	41.9	25.6	40.4	°C

Table 5.4: Altair Flux Key Material Parameters for Transient Analysis

Volume Elements :	Standard Single Stage	Halbach 4 Stages
Number of elements not evaluated	37.28 %	85.91 %
Number of excellent quality elements	31.8 %	7.85 %
Number of good quality elements	24.84 %	5.18 %
Number of average quality elements	5.85 %	0.97 %
Number of poor quality elements	0.24 %	0.09 %
Number of nodes	327556	840662
Number of line elements	19654	134538
Number of surface elements	334188	1165680
Number of volume elements	1105695	1750338
Mesh order	1st Order	1st Order

Table 5.5: Flux 3D Mesh Statistics

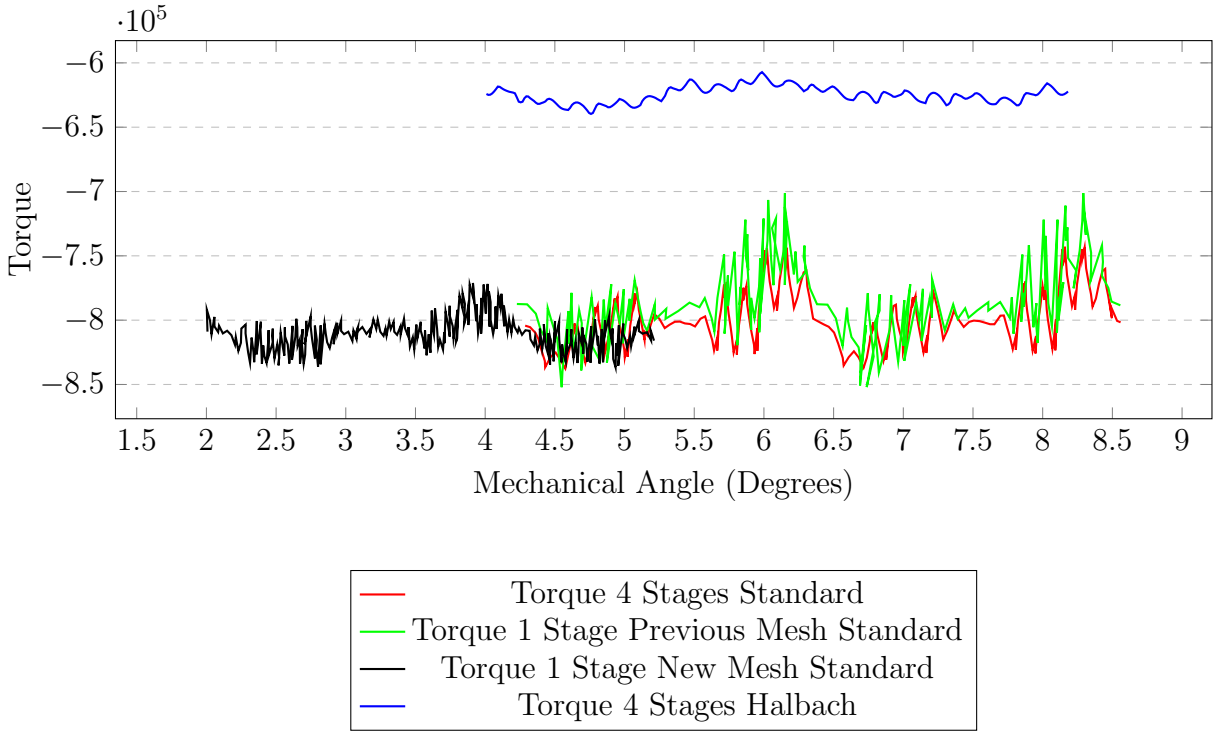

Figure 5.15: Comparison of Torque for different mesh size

	Standard	Halbach	Units
Rotor Eddy Current Loss	3.2	N/A	kW
Stator Plate Eddy Current Loss	460	528	W
Joule Loss	64.1	44	kW
Torque	846	624	kNm
Output Power	994	720	kW

Table 5.6: Standard vs. Halbach Key Comparisons

Chapter 6

Conclusion and Discussion

To improve the torque carrying capability of the standard C-GEN direct-drive generator, the thesis examined the benefits of a Halbach array proposing a new design which has some potential for wind turbines. In the first chapter, the global status of wind energy is presented and possible drive-train options are reviewed. Then, the aim of the thesis is stated as:

> "*The main aim of this thesis is to improve the torque density performance of the C-GEN air-cored axial flux permanent magnet generator by using the state-of-the-art Halbach technology.*"

In the following sections, the main outcomes of the thesis are explained, and the major contributions to knowledge and proposed future work are summarised.

6.1 General Conclusions

The Halbach model design performs well in terms of the quality of torque and torque-to-mass capability, whilst still embodying some of the unique selling points of the C-GEN technology such as modularity and redundancy. However, with the geometry constraints and parameters its inability to achieve the specified levels of torque required coupled with the complexity and potential manufacturing difficulties as each piece tries to repel the next, along with the perceived increased cost of this special design, it would require further development to justify its benefits. Based on the above, a high level comparison between the two topologies can be displayed using the same criteria as found in [48] Table 6.1.

	Standard	Halbach
Torque Smoothness	+ +	+ + +
Torque Density	+ +	+ + +
Complexity	+ + +	+
Active Mass Material	+ +	+ + +
Cost	+ + +	+

Table 6.1: General Comparison of the Standard and Halbach

6.2 Major Contribution to Knowledge

The major contributions to research developed during the course of this undertaking can be listed as follows;

1. Accurate and simplified 3D analytical expressions are developed for predicting the air gap flux density in a multi-stage Halbach array generator. This is based upon the 3D expressions established by William Thompson but extended by the principle of linear superposition to include more angles of rotation. They allow for rapid parametrization and optimisation of a Halbach topology.
2. A new approach to the implementation of C-GEN multi-stage axial flux generator is presented. Using a Halbach array in a flux focusing manner offers overall reduced mass and increased torque density. This study indicated some promising results which points towards the possibility of discovering a second generation generator with an improved overall performance.
3. A comprehensive review on the Halbach array and the accompanied full 2D equations which account for the harmonic content of the air gap flux density, is presented by offering more clarity and restoring the utility in these equations for assessing the use of a Halbach array.

6.3 Further Work

The work covered in this thesis provides the basis for further developments and this section makes suggestions for recommended work;

1. Throughout the thesis, electromagnetic modelling was at the centre of the design process, but the structural and thermal aspects of the use of materials such as carbon fibre also require further consideration. Whilst

carbon fibre offers many attractive features it is important to carry out these investigations to validate its suitability.

2. A comprehensive cost analysis is required to assess if the additional complexity associated with the use of a Halbach array and the incorporation of high profile materials as discussed above, completely outweighs the benefits.
3. Investigations of alternative designs in an effort to further improve torque density is needed. Two interesting C-GEN options have been identified which could be used individually or as a combined solution;
   (a) Combination of ferromagnetic (Cast Iron Middle Stages) and non-ferromagnetic (Carbon Fibre End Stages): In the standard axial flux multi-stage topology where the magnetic flux passes through all stages before being directed back, it may be argued since each magnet contributes to the overall flux, there might be merit in retaining cast iron in the middle stage of the Halbach model to aid in channelling the flux. Thereby hopefully improving the torque density by increasing the magnetic loading whilst still having a reduced mass compared to the Standard model.
   (b) Modular Permanent Magnet Poles (MPMP): In this arrangement, a pole is made up of a combination of low quality PM on the outside with a weaker magnetization and high quality PM with a stronger magnetization in the middle as shown in Figure 6.1. In an optimized design, this has been shown to reduce ripples in torque and EMF harmonics [142]. This manner of combining different grades of PM materials can be cost effective.

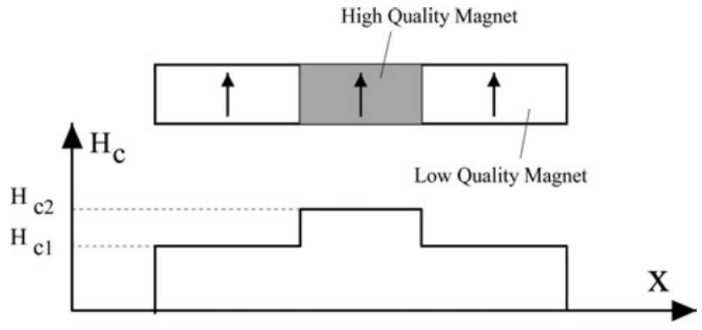

Figure 6.1: MPMP with different quality of magnets (Image adapted from [142])

4. The 3D modified equations presented here can be used in developing expressions for flux, EMF, current and force Calculations which were found

to be in good agreement with FEA predictions [81]. Further work should be carried out to realise these quantities which will allow for rapid and reliable calculations in the absence of FEA.

Appendix A

25 kW Axial C-GEN Prototype

A.1 Machine Assembly Pictures

A.2 Technical Drawings

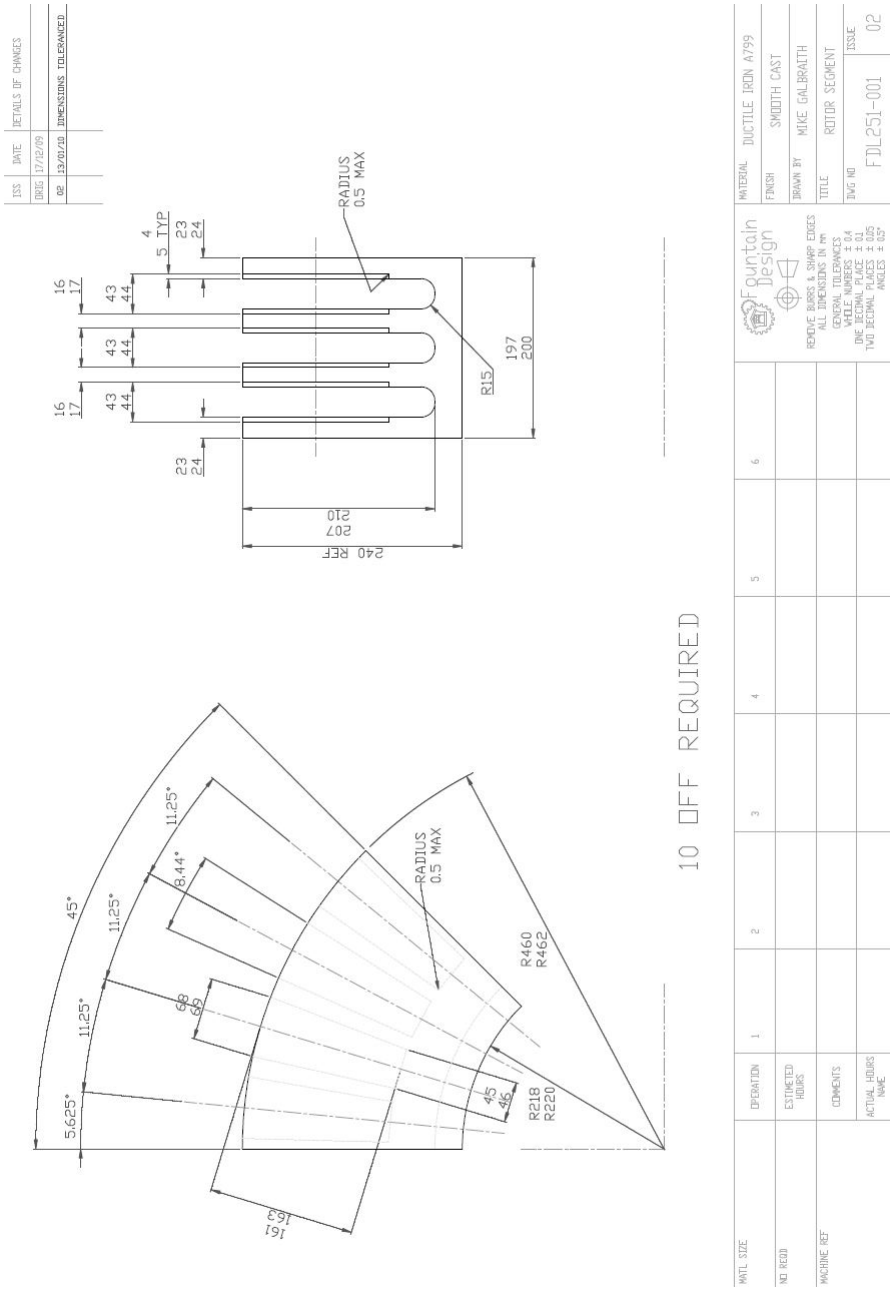
ISS
DATE
DETAILS OF CHANGES
DRG
17/12/09
02
13/01/10
DIMENSIONS TOLERANCED
RADIUS
0.5 MAX
4
5 TYP
23
24
16
17
43
44
R15
197
200
240 REF
207
210
45°
11.25°
8.44°
5.625°
68
69
45
46
R460
R462
R218
R220
161
163
10 OFF REQUIRED
MATL SIZE
WO REQD
MACHINE REF
OPERATION
ESTIMATED HOURS
COMMENTS
ACTUAL HOURS MADE
MATERIAL
DUCTILE IRON A799
FINISH
SMOOTH CAST
DRAWN BY
MIKE GALBRAITH
TITLE
ROTOR SEGMENT
DWG NO
FDL251-001
ISSUE
02
Fountain Design
REMOVE BURRS & SHARP EDGES
ALL DIMENSIONS IN mm
GENERAL TOLERANCES
WHOLE NUMBERS ± 0.4
ONE DECIMAL PLACE ± 0.1
TWO DECIMAL PLACES ± 0.05
ANGLES ± 0.5°

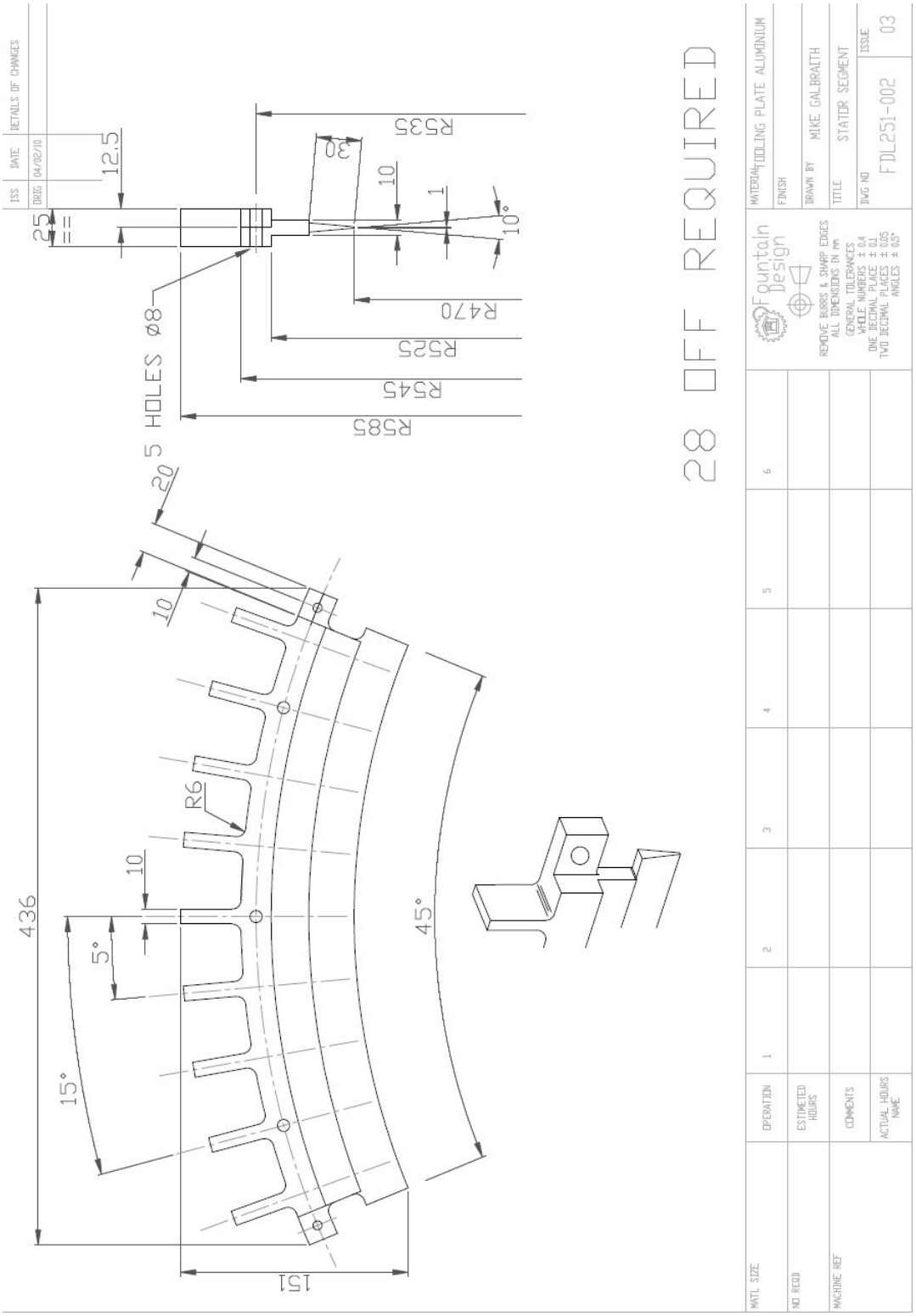
28 OFF REQUIRED
5 HOLES ø8
R585
R545
R525
R470
R535
30
10
1
10°
12.5
25
20
10
R6
436
10
5°
15°
45°
151
ISS
DRIG
DATE
04/02/10
DETAILS OF CHANGES
MATERIAL TOOLING PLATE ALUMINIUM
FINISH
DRAWN BY MIKE GALBRAITH
TITLE STATOR SEGMENT
DWG NO FDL251-002
ISSUE 03
Fountain Design
REMOVE BURRS & SHARP EDGES
ALL DIMENSIONS IN mm
GENERAL TOLERANCES
WHOLE NUMBERS ± 0.4
ONE DECIMAL PLACE ± 0.1
TWO DECIMAL PLACES ± 0.05
ANGLES ± 0.5°
MATL SIZE
NO REQD
MACHINE REF
OPERATION
ESTIMETED HOURS
COMMENTS
ACTUAL HOURS
NAME

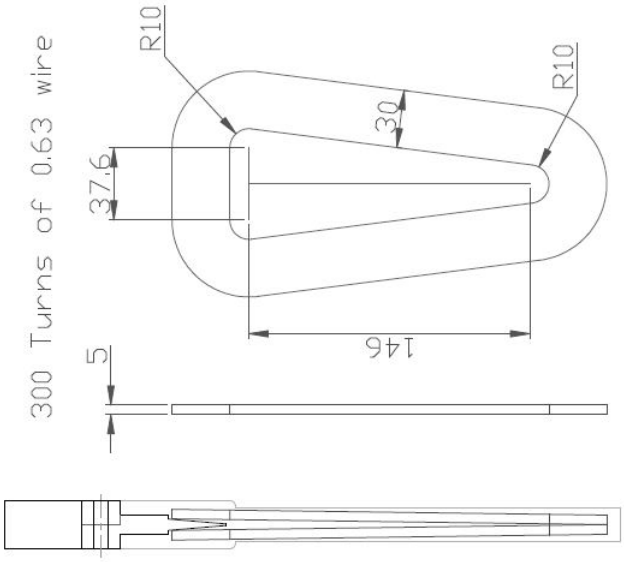
300 Turns of 0.63 wire
R10
R10
30
37.6
146
5

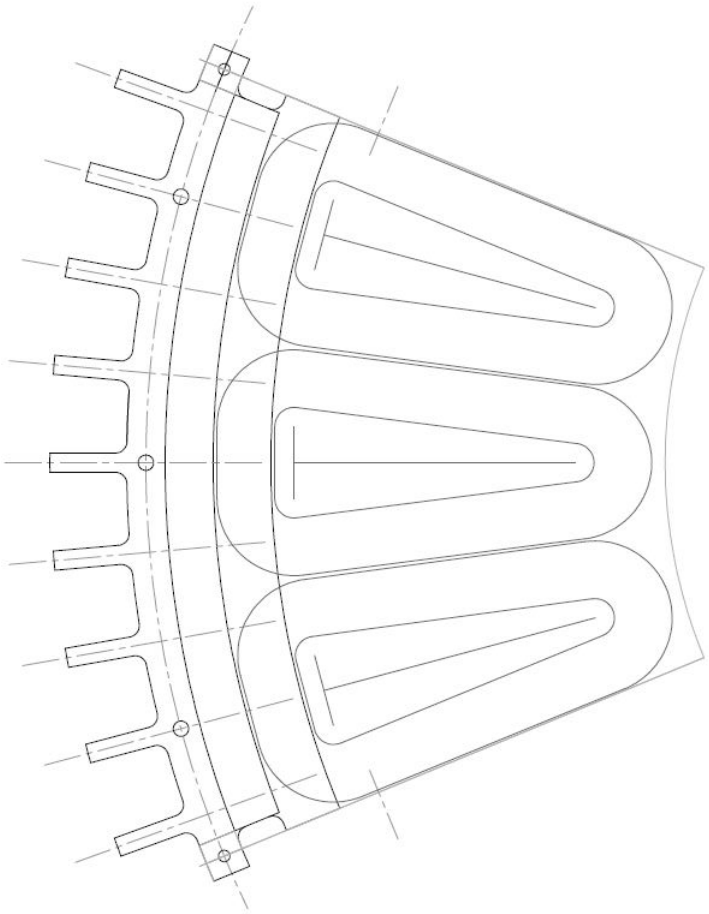

Appendix B

1 MW Axial C-GEN Demonstrator

B.1 Machine Assembly Picture

B.2 Technical Drawings

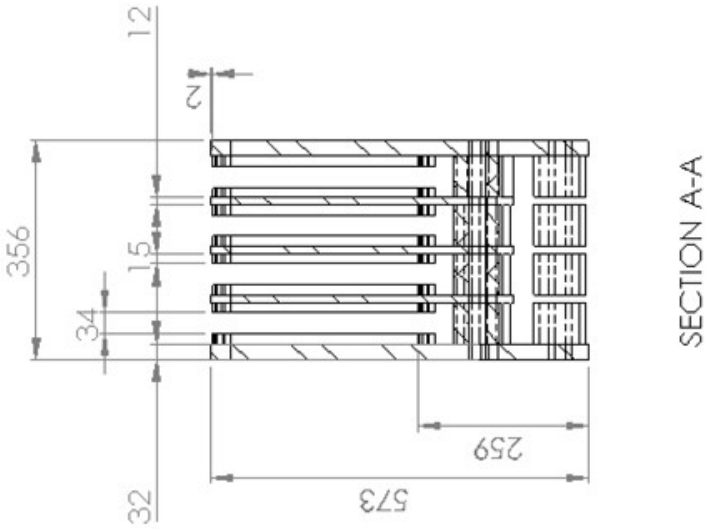
12
2
356
15
34
32
259
573
SECTION A-A

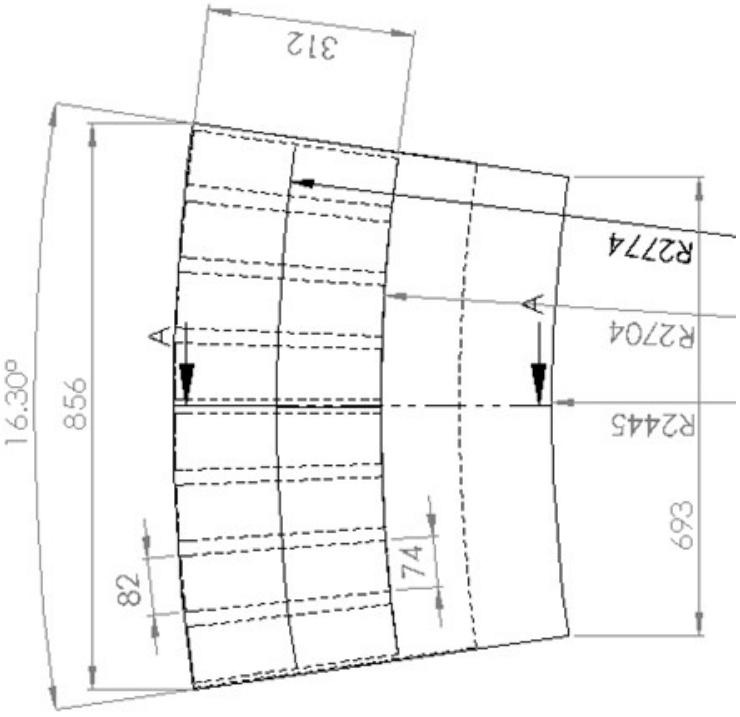
312
R2774
R2704
R2445
A
A
16.30°
856
82
74
693

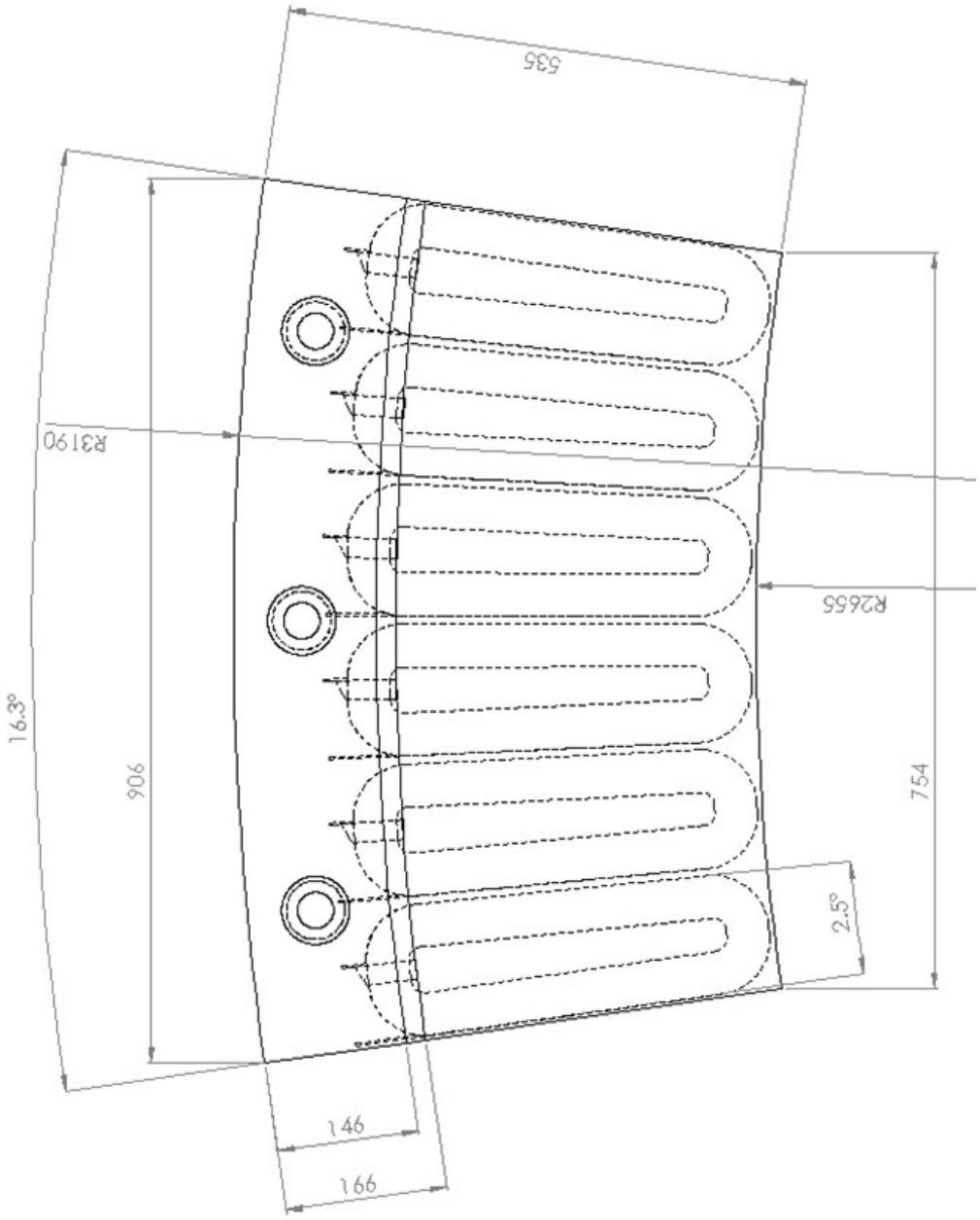
535
R3190
R2655
16.3°
906
754
2.5°
146
166

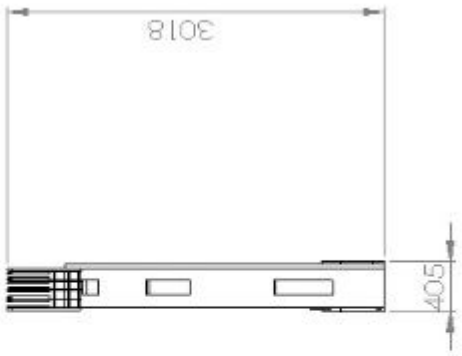
3018
405

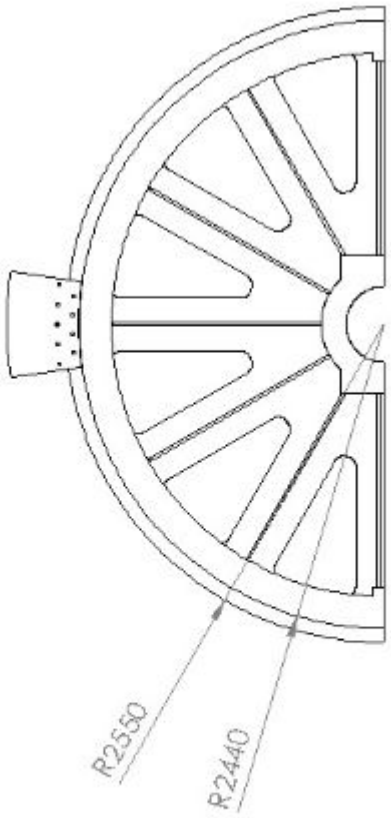
R2550
R2440

Appendix C

25 kW Standard 3D MagNet Model and Result

C.1 Geometrical Model

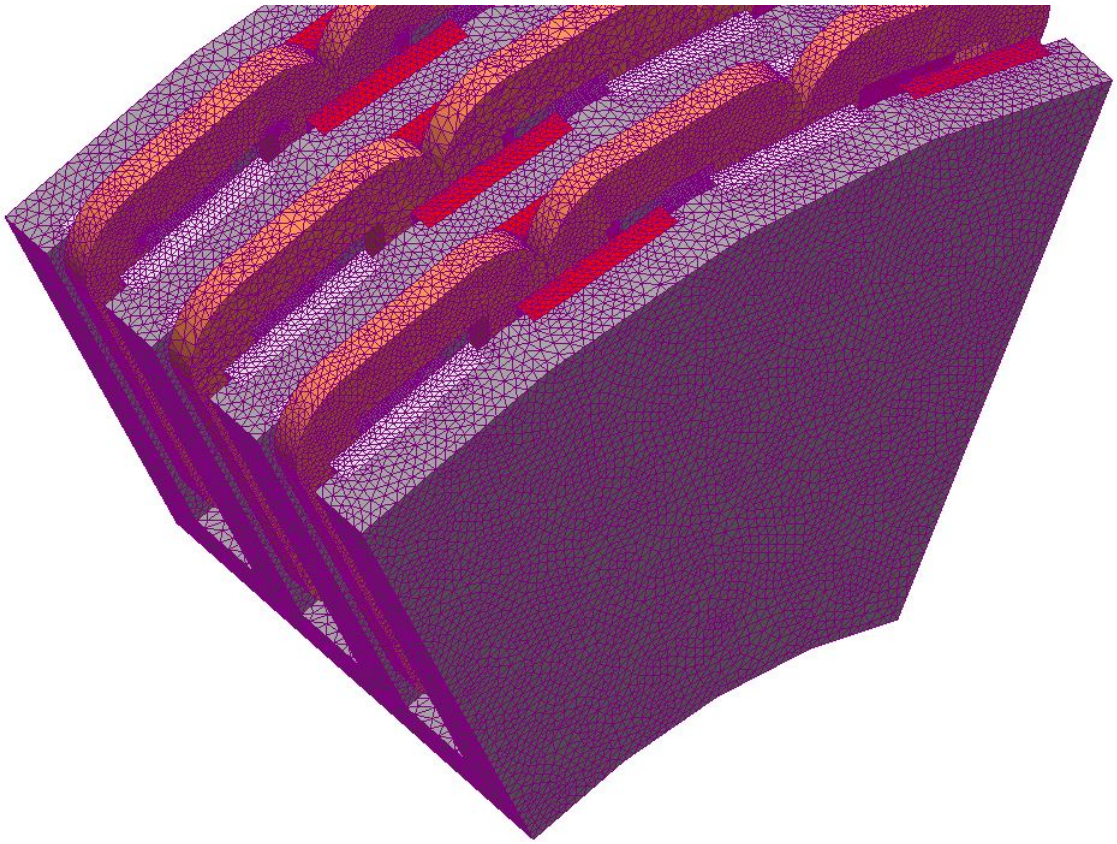

C.2 Flux Density Shaded Plot

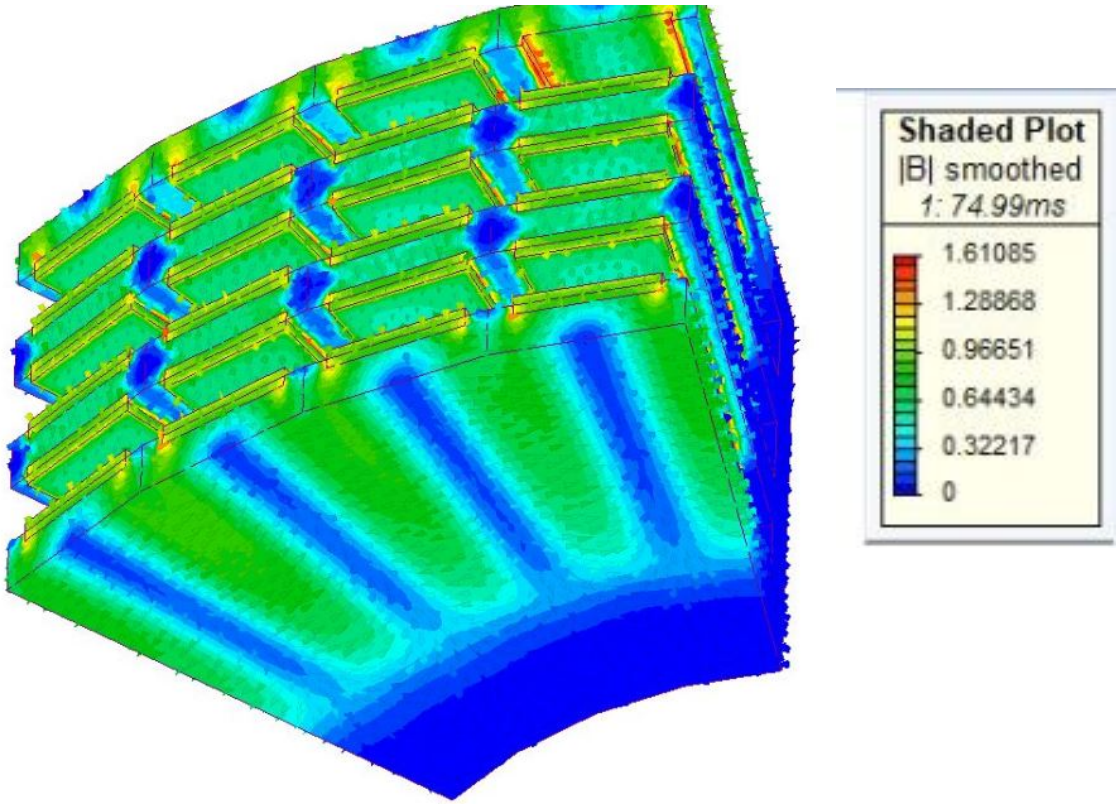

C.3 Phase Voltage Vs. Time

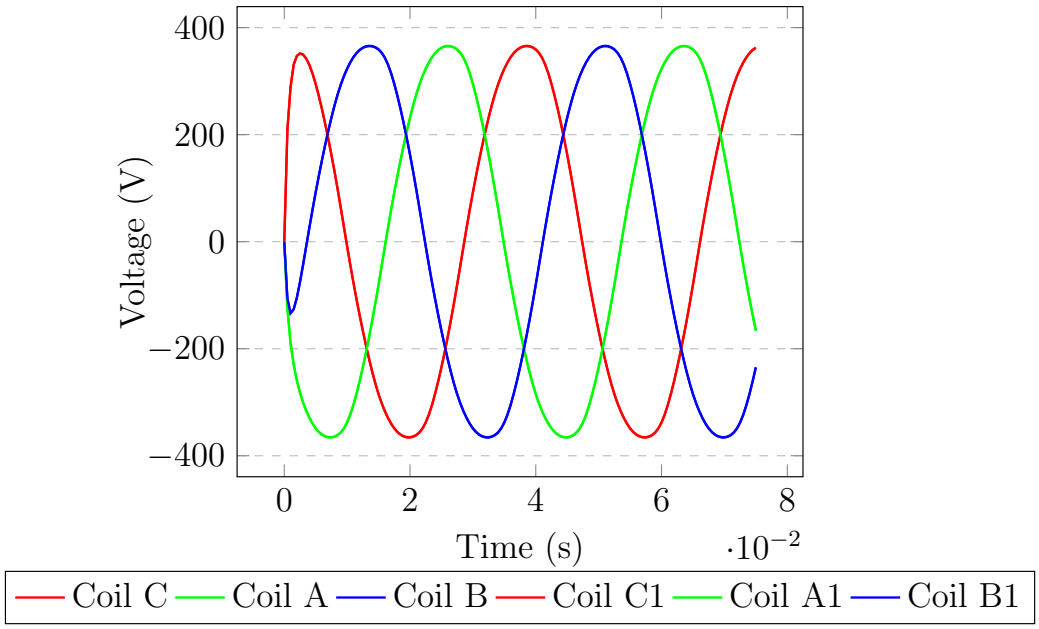

C.4 Phase Currents Vs. Time

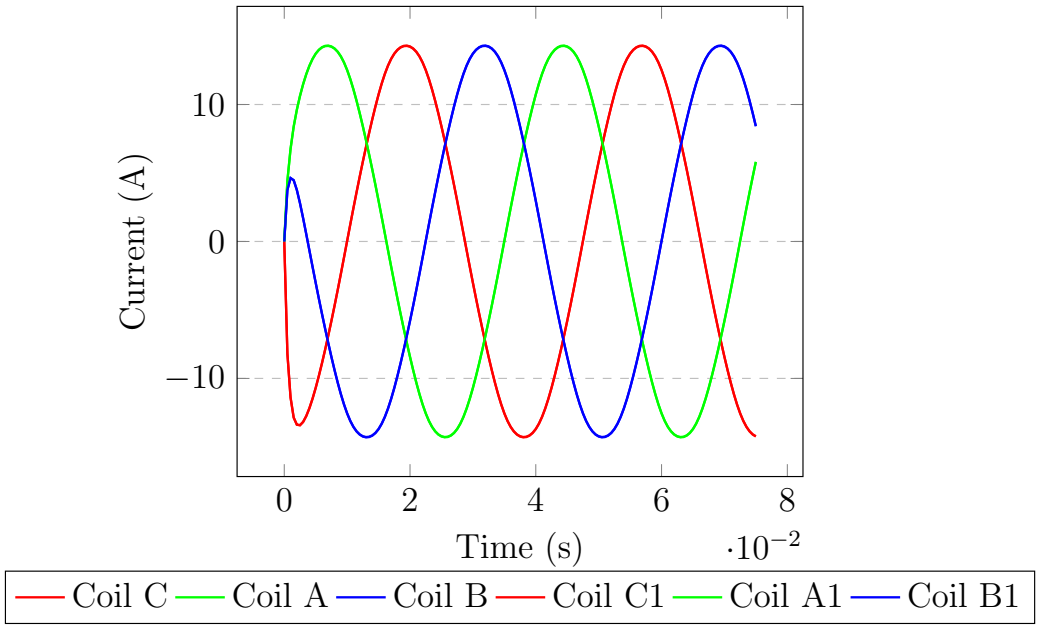

Appendix D

25 kW Halbach 3D MagNet Additional Results

D.1 A Close-Up View of the Magnetic Flux Density Distribution in the Halbach Model

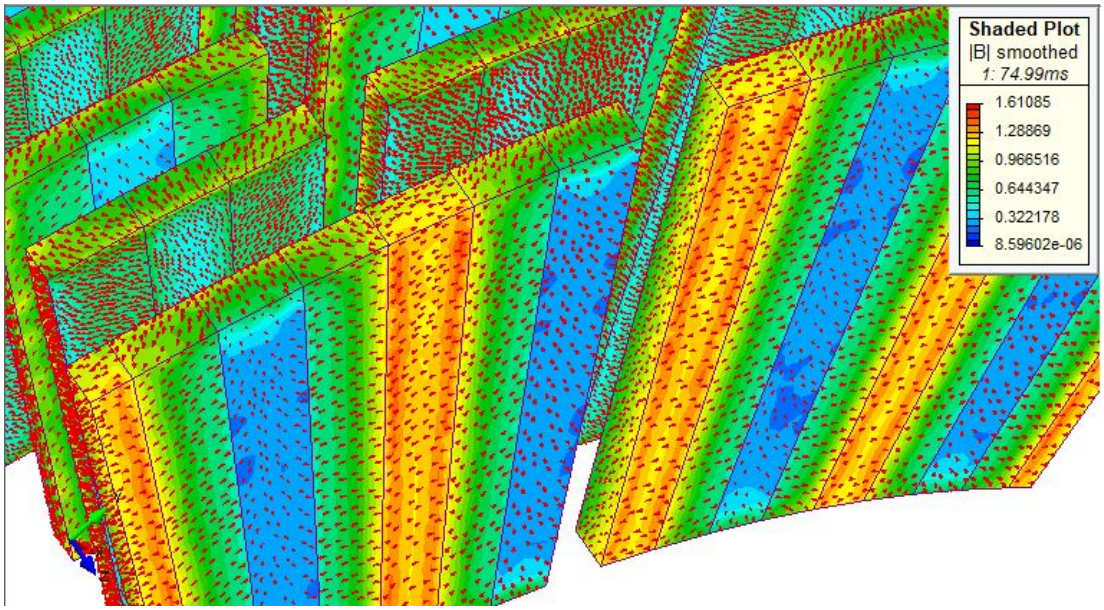

D.2 Phase Voltage Vs. Time

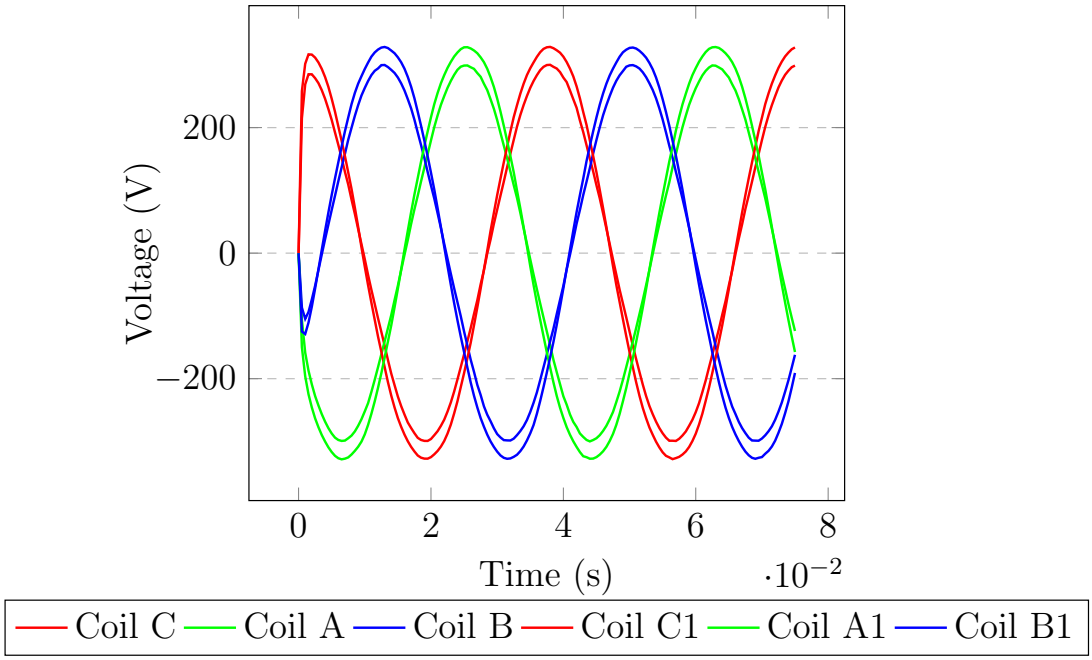

D.3 Phase Currents Vs. Time

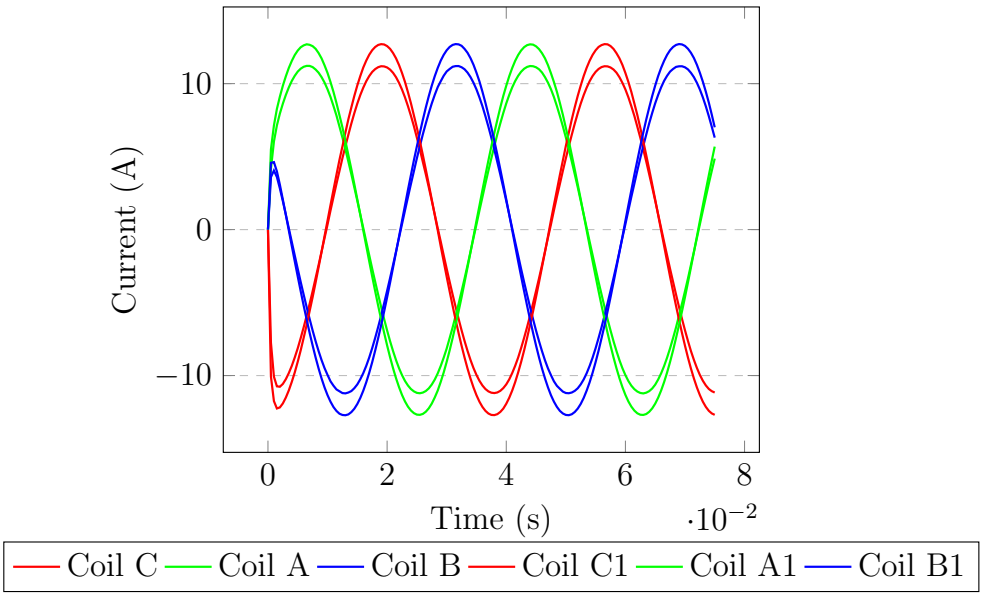

Appendix E

Electromagnetic Modelling Dimensions

E.1 C-GEN Multi-Stage Illustrative Figures

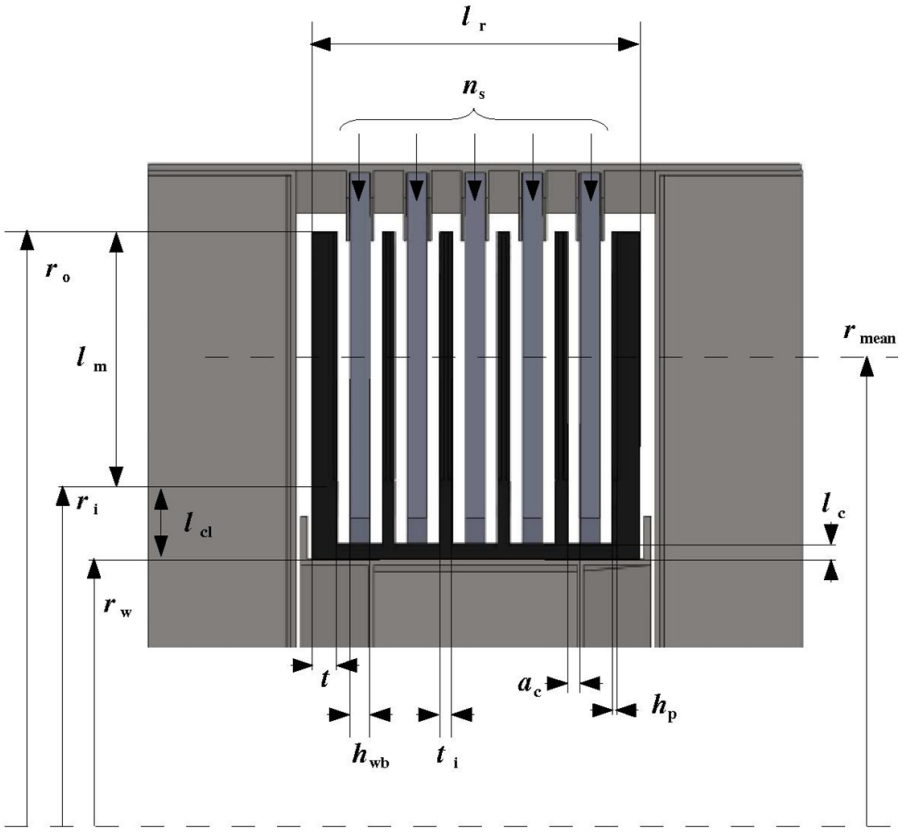

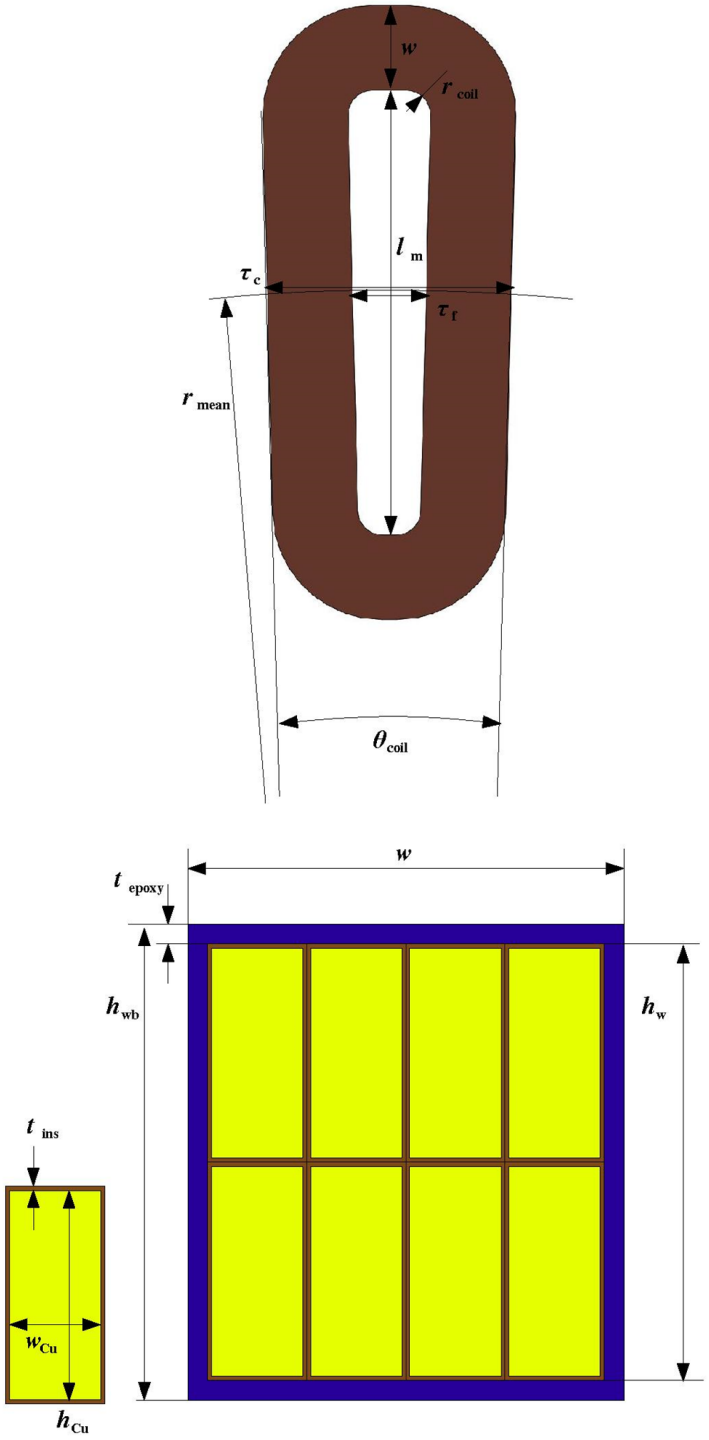
w
r coil
l m
τ c
τ t
r mean
θ coil
w
t epoxy
h wb
h w
t ins
w Cu
h Cu

Full name	Symbol	25 kW	1 MW	Unit
Mean active radius	r_{mean}	380	2860	mm
Magnet outer radius	r_o	460	3016	mm
Magnet inner radius	r_i	300	2704	mm
Web radius	r_w	220	2585	mm
Radial length of magnet	l_m	160	312	mm
Outer limb thickness	t	23	20	mm
Inner limb thickness	t_i	26	12	mm
Steel web thickness	l_c	30	20	mm
Magnet pocket height	h_p	5	0	mm
Physical air gap clearance	a_c	3.5	5	mm
Magnet height	h_m	10	15	mm
Winding block height	h_{wb}	13	24	mm
Coil height	h_w	12	22	mm
Epoxy thickness of coil block	t_{epoxy}	0.5	1	mm
Width of coil side	w	32	45	mm
Mean pole pitch	τ_p	75	102	mm
Mean coil pitch	τ_c	96	133	mm
Mean former pitch	τ_f	12	42	mm
Mean magnet width	w_m	56	76	mm
Radial clearance between magnet and web	l_{cl}	80	119	mm
Overall axial length of rotor unit	l_r	240	332	mm
Wire copper width	w_{C_u}	0	1.96	mm
Wire copper height	h_{C_u}	0	21.78	mm
Equivalent circular wire diameter	θ_d	0.63		mm
Wire copper area	A_{C_u}	0.312	42.7	mm^2
Enamel insulation thickness	t_{ins}	0.015	0.11	mm
Copper to total fill factor	k_{fill}	0.50	0.77	
Copper to wire fill factor	k_{fill}, C_u/W	0.91	0.89	
Wire to total fill factor	k_{fill}, W/T	0.55	0.86	
Former radii	r_{coil}	10	13	mm
Pole angle (mechanical)	θ_p	11.25	2.05	°
Magnet angle (mechanical)	θ_m	8.44	1.51	°
Coil angle (mechanical)	θ_{coil}	15	2.73	°
Number of turns per coil	N_t	600	20	
Number of poles per stage	N_p	32	176	
Number of stages	n_s	3	4	
Number of coils per stage	N_c	24	132	
Number of phases per stage	m	3	3	
Number of parallel branches per phase	N_{branch}	8	1	
Number of coils in series per branch	$Nseries$	1	44	
Number of coils per phase per stage	N_c/m	8	44	
Width of coil side/mean coil pitch ratio	w/τ_c	0.33	0.334	
Magnet width/pole pitch ratio	w_m/τ_p	0.75	0.74	
Magnet Grade		N35H	N38M	

25 kW and 1 MW C-GEN Standard Generator Details

Appendix F

1 MW Standard Flux 3D Mesh Results

F.1 5 Stage Mesh

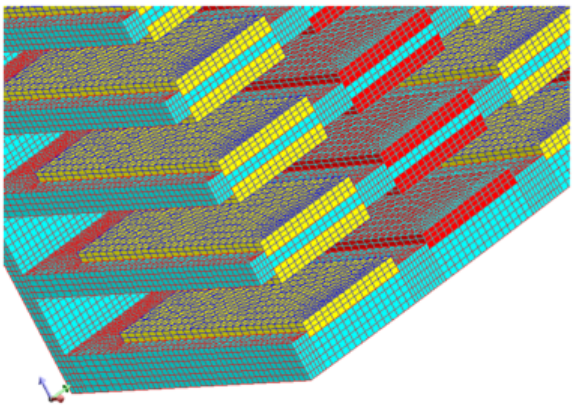

Number of nodes : 314734
Number of line elements : 59706
Number of surface elements : 486876
Number of volume elements : 681036
Mesh order : 1st order

F.2 1 Stage Modelling Previous Mesh

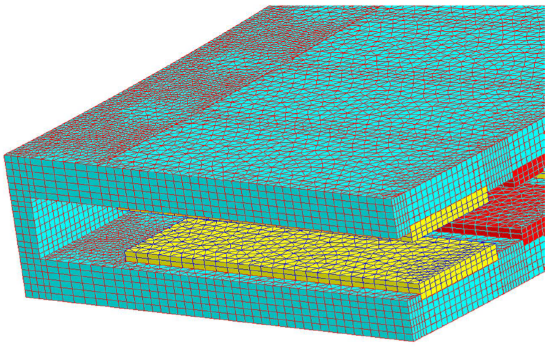

Number of nodes : 105104
Number of line elements : 17655
Number of surface elements : 147518
Number of volume elements : 223681
Mesh order : 1st order

F.3 1 Stage Modelling New Mesh

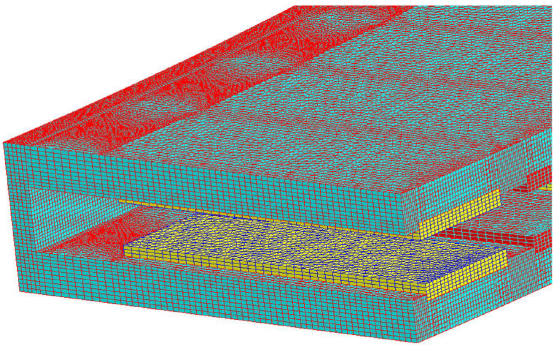

Number of nodes : 435591
Number of line elements : 28249
Number of surface elements : 374886
Number of volume elements : 966320
Mesh order : 1st order

F.4 Standard Vs. Halbach Models, Mesh and Flux Contour

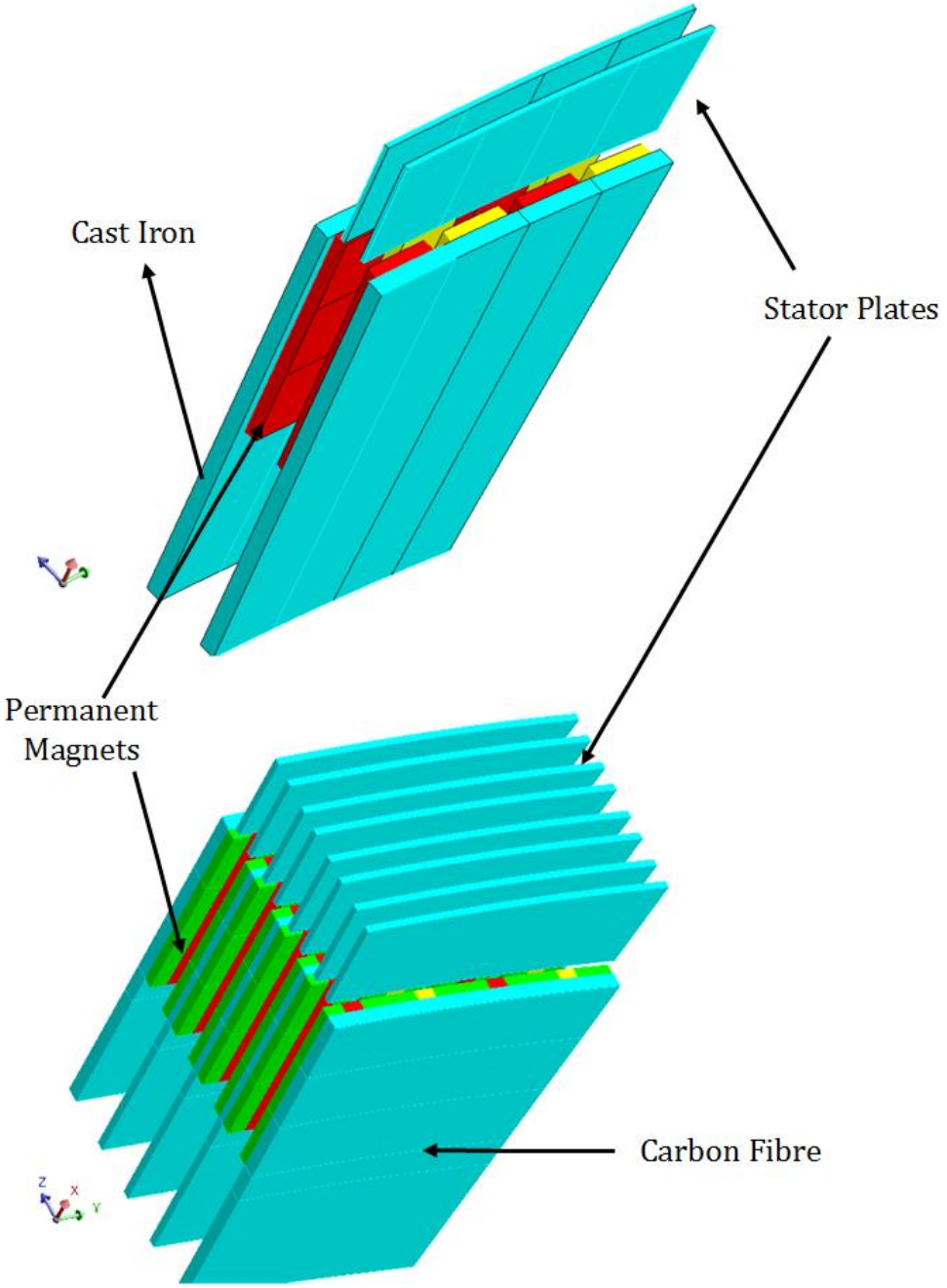

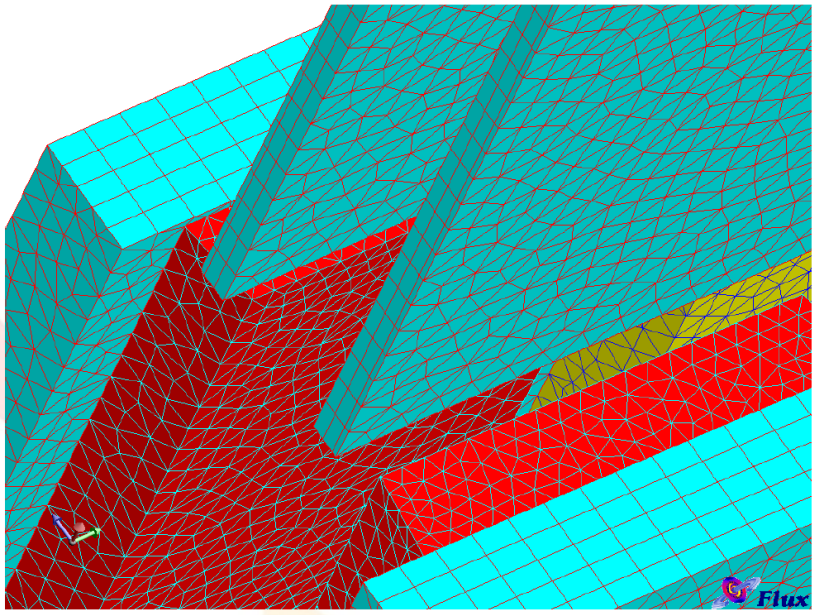
Flux

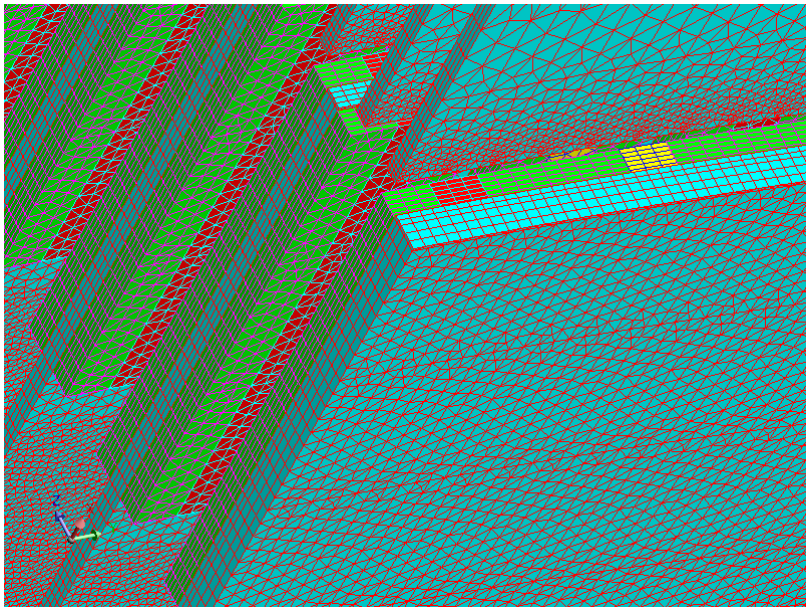

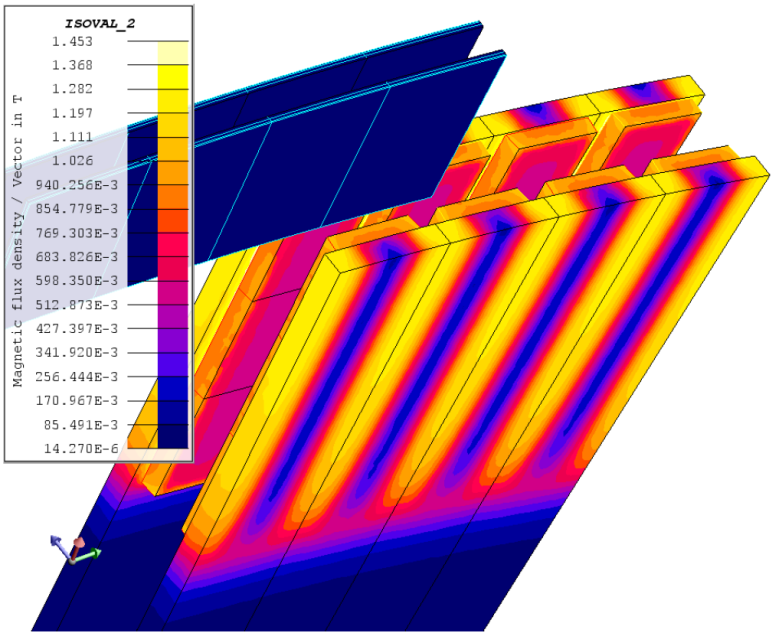
ISOVAL_2
1.453
1.368
1.282
1.197
1.111
1.026
940.256E-3
854.779E-3
769.303E-3
683.826E-3
598.350E-3
512.873E-3
427.397E-3
341.920E-3
256.444E-3
170.967E-3
85.491E-3
14.270E-6
Magnetic flux density / Vector in T

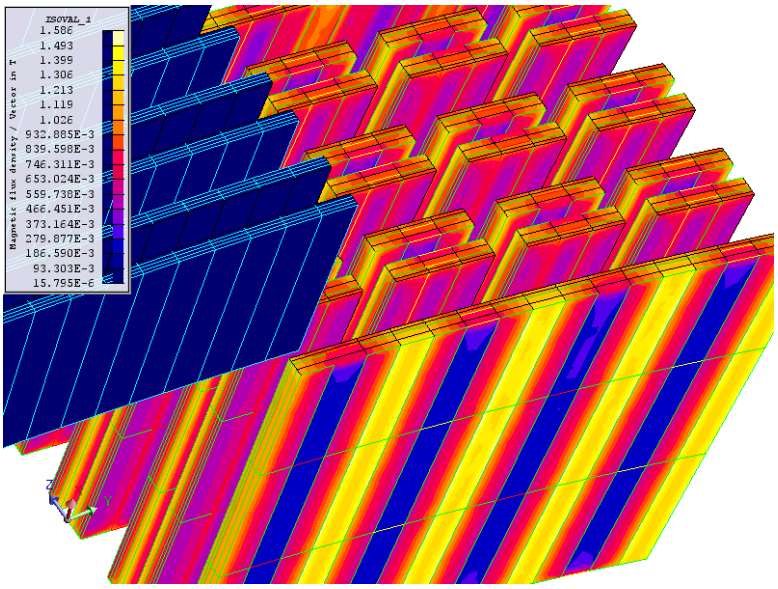
ISOVAL_1
1.586
1.493
1.399
1.306
1.213
1.119
1.026
932.885E-3
839.598E-3
746.311E-3
653.024E-3
559.738E-3
466.451E-3
373.164E-3
279.877E-3
186.590E-3
93.303E-3
15.795E-6
Magnetic flux density / Vector in T

Bibliography

[1] Global Wind Energy Council. Global Wind Report - Annual Market Update 2017. Technical report, 2018. URL https://www.researchgate.net/publication/324966225_GLOBAL_WIND_REPORT_-_Annual_Market_Update_2017.

[2] Iván Pineda and WindEurope Pierre Tardieu. Annual combined onshore and offshore wind energy statistics. 2018. ISSN 22107789. doi: 10.1016/j.preghy.2016.08.046. URL https://windeurope.org/wp-content/uploads/files/about-wind/statistics/WindEurope-Annual-Statistics-2017.pdf.

[3] UpWind. Design Limits and Solutions for Very Large Wind Turbines - EU 6th Frame Project. Technical report, 2011. URL http://www.ewea.org/our-activities/eu-funded-projects/completed-projects/upwind/.

[4] The International Energy Agency (IEA). Wind Energy in France. URL https://community.ieawind.org/about/member-activities/france.

[5] Anmar Frangoul. From China to Brazil, these are the world titans of wind power, 2018. URL https://www.cnbc.com/2018/06/04/from-china-to-brazil-these-are-the-world-titans-of-wind-power.html.

[6] Anastasia Smolentseva. Wind Energy in Canada, 2017. URL https://canwea.ca/wind-energy/installed-capacity/wind-energy-in-canada-2/.

[7] Kaswar Mostafa. *Direct Drive Wind Turbines: The Effect of Unbalanced Magnetic Pull on Permanent Magnet Generators and Bearing Arrangements*. PhD thesis, University of Ediburgh, 2017. URL https://era.ed.ac.uk/handle/1842/31360.

[8] D Bang, H Polinder, Ghanshyam Shrestha, and Jan Abraham Ferreira. Review of generator systems for direct-drive wind turbines. *European Wind Energy Conference and Exhibition*, pages 1–11, 2008. ISSN 1161-0301. doi: 10.1063/1.1841896. URL http://www.mojaladja.com/upload/elmotor/ReviewofGeneratorSystemsforDirect-DriveWindTurbines.pdf.

[9] Troy A. Rule. *Solar, Wind and Land Conflicts in Renewable Energy Development*. Routledge, sep 2014. ISBN 9781315770079. doi: 10.4324/9781315770079. URL https://www.taylorfrancis.com/books/9781315770079.

[10] National Renewable Energy Laboratory. Simple Levelized Cost of Energy (LCOE) Calculator Documentation. URL https://www.nrel.gov/analysis/tech-lcoe-documentation.html.

[11] Robert Norris. Offshore wind on target to become lowest-cost, large scale clean energy source, 2017. URL https://www.renewableuk.com/news/327446/Offshore-wind-on-target-to-become-lowest-cost-large-scale-clean-energy-source.htm.

[12] Pilita Clark. Energy groups in pledge to slash cost of offshore wind farms, 2016. URL https://www.ft.com/content/c0b56810-29b9-11e6-8b18-91555f2f4fde.

[13] F. Spinato, P.J. Tavner, G.J.W. van Bussel, and E. Koutoulakos. Reliability of wind turbine subassemblies. *IET Renewable Power Generation*, 3(4):387, 2009. ISSN 17521416. doi: 10.1109/RTC.2016.7543074. URL http://digital-library.theiet.org/content/journals/10.1049/iet-rpg.2008.0060.

[14] Daan Moreels. This New Generation of Direct-Drive Electric Machines will Power our Future, 2017. URL https://www.magnax.com/magnax-blog/axial-flux-vs-radial-flux-for-direct-drive-generators.

[15] Ozan Keysan. *Superconducting Generators for Large Offshore Wind Turbines Doctor of Philosophy*. PhD thesis, University of Edinburgh, 2014. URL https://era.ed.ac.uk/handle/1842/8841.

[16] Khalil Touimi, Mohamed Benbouzid, and Peter Tavner. A Review-based Comparison of Drivetrain Options for Tidal Turbines. In *2018 IEEE International Power Electronics and Application Conference and Exposition (PEAC)*, pages 1–6. IEEE, nov 2018. ISBN 978-1-5386-6054-6. doi: 10.1109/PEAC.2018.8590460. URL https://ieeexplore.ieee.org/document/8590460/.

[17] National Renewable Energy Laboratory. Report on Wind Turbine Subsystem Reliability, A Survey of Various Databases. Technical report, jun 2013. URL https://www.nrel.gov/docs/fy13osti/59111.pdf.

[18] Alasdair S Mcdonald. *Structural analysis of low speed, high torque electrical generators for direct drive renewable energy converters*. PhD thesis, University of Edinburgh, 2008. URL https://era.ed.ac.uk/handle/1842/12608.

[19] Markus A. Mueller and Alasdair S. McDonald. A lightweight low-speed permanent magnet electrical generator for direct-drive wind turbines. *Wind Energy*, 12(8):768–780, nov 2009. ISSN 10954244. doi: 10.1002/we.333. URL http://doi.wiley.com/10.1002/we.333.

[20] Jan Dodd. Rethinking the use of rare-earth elements, 2018. URL https://www.windpowermonthly.com/article/1519221/rethinking-use-rare-earth-elements.

[21] Aysel Akgemci and Reza Zeinali. Minimization of EMF Harmonics and Cogging Torque for a Medium Speed RFPM Wind Turbine Generator. *2018 7th International Conference on Renewable Energy Research and Applications (ICRERA)*, 5:342–347, 2018. doi: 10.1109/ICRERA.2018.8566734. URL https://ieeexplore.ieee.org/document/8566734.

[22] Hui Li, Zhe Chen, and Henk Polinder. Optimization of multibrid permanent-magnet wind generator systems. *IEEE Transactions on Energy Conversion*, 24(1):82–92, 2009. ISSN 08858969. doi: 10.1109/TEC.2008.2005279. URL https://ieeexplore.ieee.org/document/4783055.

[23] Ivan G Piña Rodriguez. *Hydraulic Drivetrains for Wind Turbines*. PhD thesis, Delft University of Technology, 2012. URL https://pdfs.semanticscholar.org/d9f6/a743a5c28fb6ee324817ce289b865b09d2bc.pdf.

[24] Ben McGilton, Richard Crozier, Alasdair McDonald, and Markus Mueller. Review of magnetic gear technologies and their applications in marine energy. *IET Renewable Power Generation*, 12(2):174–181, 2018. ISSN 1752-1416. doi: 10.1049/iet-rpg.2017.0210. URL http://digital-library.theiet.org/content/journals/10.1049/iet-rpg.2017.0210.

[25] P. M. Tlali, R-J. Wang, and S. Gerber. Magnetic gear technologies: A review. In *2014 International Conference on Electrical Machines (ICEM)*, pages 544–550. IEEE, sep 2014. ISBN 978-1-4799-4389-0. doi: 10.1109/ICELMACH.2014.6960233. URL http://ieeexplore.ieee.org/document/6960233/.

[26] Kais Atallah, Jiabin Wang, Smail Mezani, and David Howe. A Novel High-Performance Linear Magnetic Gear. *IEEJ Transactions on Industry Applications*, 126(10):1352–1356, 2006. ISSN 0913-6339. doi: 10.1541/ieejias.126.1352. URL https://www.jstage.jst.go.jp/article/ieejias/126/10/126_10_1352/_pdf.

[27] J. Mallinson. One-sided fluxes – A magnetic curiosity? *IEEE Transactions on Magnetics*, 9(4):678–682, dec 1973. ISSN 0018-9464. doi: 10.1109/TMAG.1973.1067714. URL http://ieeexplore.ieee.org/document/1067714/.

[28] E. D. Daniel. Tape Noise in Audio Recording. *Journal of the Audio Engineering Society*, 20(2):92–99, 1972. ISSN 00047554. URL http://www.aes.org/e-lib/browse.cfm?elib=2095.

[29] James U. Lemke. An isotropic particulate medium with additive Hilbert and Fourier field components. *Journal of Applied Physics*, 53(3):2561–2566, mar 1982. ISSN 0021-8979. doi: 10.1063/1.330908. URL https://aip.scitation.org/doi/10.1063/1.330908http://aip.scitation.org/doi/10.1063/1.330908.

[30] H. Neal Bertram. *Theory of Magnetic Recording*. Cambridge University Press, 1994. ISBN 0521449731. doi: 10.1017/CBO9780511623066. URL https://books.google.com/books?id=PZCpT6JegdgC&pgis=1.

[31] P. J. Flanders. Experimental demonstration of one-sided flux in magnetic recording tape. *Journal of Applied Physics*, 61(8):4007–4009, apr 1987. ISSN 0021-8979. doi: 10.1063/1.338561. URL http://aip.scitation.org/doi/10.1063/1.338561.

[32] H.A. Shute, J.C. Mallinson, D.T. Wilton, and D.J. Mapps. One-sided fluxes in planar, cylindrical, and spherical magnetized structures. *IEEE Transactions on Magnetics*, 36(2):440–451, mar 2000. ISSN 00189464.

doi: 10.1109/20.825805. URL http://ieeexplore.ieee.org/document/825805/.

[33] K. Halbach. Design of permanent multipole magnets with oriented rare earth cobalt material. *Nuclear Instruments and Methods*, 169(1):1–10, 1980. ISSN 0029554X. doi: 10.1016/0029-554X(80)90094-4. URL https://www.sciencedirect.com/science/article/pii/0029554X80900944.

[34] Klaus Halbach. Application of permanent magnets in accelerators and electron storage rings (invited). *Journal of Applied Physics*, 57(8):3605–3608, 1985. ISSN 00218979. doi: 10.1063/1.335021. URL https://aip.scitation.org/doi/10.1063/1.335021.

[35] J. Mallinson. On the properties of two-dimensional dipoles and magnetized bodies. *IEEE Transactions on Magnetics*, 17(5):2453–2460, sep 1981. ISSN 0018-9464. doi: 10.1109/TMAG.1981.1061400. URL http://ieeexplore.ieee.org/document/1061400/.

[36] Ross. Schlueter and Soren Prestemon. Advanced insertion devices - practices and concepts, 2010. URL https://portal.slac.stanford.edu/sites/ad_public/events/FLS2010/Lists/FLS2010WorkshopProgram/Attachments/45/Schlueter_FLS_2010-advanced_insertion_devices-practices_and_concepts_v4_03-March-2010_0750(2).pdf.

[37] J. Ofori-Tenkorrang and J.H. Lang. A comparative analysis of torque production in Halbach and conventional surface-mounted permanent-magnet synchronous motors. In *IAS '95. Conference Record of the 1995 IEEE Industry Applications Conference Thirtieth IAS Annual Meeting*, volume 1, pages 657–663. IEEE, 2005. ISBN 0-7803-3008-0. doi: 10.1109/IAS.1995.530362. URL http://ieeexplore.ieee.org/document/530362/.

[38] Will Robertson. *Modelling and design of magnetic levitation systems for vibration isolation*. PhD thesis, 2013. URL http://data.mecheng.adelaide.edu.au/avc/publications/thesis/2013/Robertson_Thesis_2014.pdf.

[39] Z.Q. Zhu, Z.P. Xia, Y.F. Shi, D. Howe, A. Pride, and X.J. Chen. Performance of Halbach magnetised brushless ac motor. In *Digest of INTERMAG 2003. International Magnetics Conference (Cat. No.03CH37401)*, pages

GQ–03. IEEE, 2003. ISBN 0-7803-7647-1. doi: 10.1109/INTMAG.2003.1230840. URL http://ieeexplore.ieee.org/document/1230840/.

[40] B.C. Mecrow, A.G. Jack, D.J. Atkinson, S. Green, G.J. Atkinson, A. King, and B. Green. Design and testing of a 4 phase fault tolerant permanent magnet machine for an engine fuel pump. In *IEEE International Electric Machines and Drives Conference, 2003. IEMDC'03.*, volume 2, pages 1301–1307. IEEE, 2003. ISBN 0-7803-7817-2. doi: 10.1109/IEMDC.2003.1210407. URL http://ieeexplore.ieee.org/document/1210407/.

[41] Phil H. Mellor and Rafal Wrobel. Optimization of a Multipolar Permanent-Magnet Rotor Comprising Two Arc Segments per Pole. *IEEE Transactions on Industry Applications*, 43(4):942–951, 2007. ISSN 0093-9994. doi: 10.1109/TIA.2007.900479. URL http://ieeexplore.ieee.org/document/4276859/.

[42] Changliang Xia, Hongfeng Li, and Tingna Shi. 3-D Magnetic Field and Torque Analysis of a Novel Halbach Array Permanent-Magnet Spherical Motor. *IEEE Transactions on Magnetics*, 44(8):2016–2020, aug 2008. ISSN 0018-9464. doi: 10.1109/TMAG.2008.922782. URL http://ieeexplore.ieee.org/document/4618670/.

[43] Z.Q. Zhu and D. Howe. Halbach permanent magnet machines and applications: a review. *IEE Proceedings - Electric Power Applications*, 148(4):299, 2001. ISSN 13502352. doi: 10.1049/ip-epa:20010479. URL https://digital-library.theiet.org/content/journals/10.1049/ip-epa_20010479.

[44] Z.Q. Zhu, Z.P. Xia, K. Atallah, G.W. Jewell, and D. Howe. Novel permanent magnet machines using Halbach cylinders. In *Proceedings IPEMC 2000. Third International Power Electronics and Motion Control Conference (IEEE Cat. No.00EX435)*, volume 2, pages 903–908. Int. Acad. Publishers, 2000. ISBN 7-80003-464-X. doi: 10.1109/IPEMC.2000.884630. URL http://ieeexplore.ieee.org/document/884630/.

[45] Jiabin Wang and David Howe. Tubular modular permanent-magnet machines equipped with quasi-Halbach magnetized magnets-part II: armature reaction and design optimization. *IEEE Transactions on Magnetics*, 41(9):2479–2489, sep 2005. ISSN 0018-9464. doi: 10.1109/TMAG.2005.854327. URL http://ieeexplore.ieee.org/document/1506918/.

[46] Suman Dwari, Leila Parsa, and Kamiar J. Karimi. Design and analysis of halbach array permanent magnet motor for high acceleration applications. *2009 IEEE International Electric Machines and Drives Conference, IEMDC '09*, 2(c):1100–1104, 2009. doi: 10.1109/IEMDC.2009.5075341. URL https://ieeexplore.ieee.org/document/5075341.

[47] Suman Dwari and Leila Parsa. Design of halbach-array-based permanent-magnet motors with high acceleration. *IEEE Transactions on Industrial Electronics*, 58(9):3768–3775, 2011. ISSN 02780046. doi: 10.1109/TIE.2011.2112315. URL https://ieeexplore.ieee.org/document/5709981.

[48] Michael Galea. *High performance , Direct Drive machines for Aerospace Applications*. PhD thesis, University of Nottingham, 2013. URL http://eprints.nottingham.ac.uk/id/eprint/14431.

[49] Dura Magnetics Inc. Benefits and Drawbacks to Using Halbach Arrays. URL https://www.duramag.com/techtalk/halbach-arrays/benefits-and-drawbacks-to-using-halbach-arrays/.

[50] Jiabin Wang, Weiya Wang, and Kais Atallah. A Linear Permanent-Magnet Motor for Active Vehicle Suspension. *IEEE Transactions on Vehicular Technology*, 60(1):55–63, jan 2011. ISSN 0018-9545. doi: 10.1109/TVT.2010.2089546. URL http://ieeexplore.ieee.org/document/5608522/.

[51] Jacek F. Gieras, Rong-Jie Wang, and Maarten J. Kamper. *Axial Flux Permanent Magnet Brushless Machines*. Springer Netherlands, Dordrecht, 2008. ISBN 978-1-4020-6993-2. doi: 10.1007/978-1-4020-8227-6. URL http://link.springer.com/10.1007/978-1-4020-8227-6.

[52] Tsarafidy Raminosoa, Tahar Hamiti, Michael Galea, and Chris Gerada. Feasibility and electromagnetic design of direct drive wheel actuator for green taxiing. In *2011 IEEE Energy Conversion Congress and Exposition*, pages 2798–2804. IEEE, sep 2011. ISBN 978-1-4577-0542-7. doi: 10.1109/ECCE.2011.6064145. URL http://ieeexplore.ieee.org/document/6064145/.

[53] J. Wang, W Wang, K Atallah, and D Howe. Demagnetization Assessment for Three-Phase Tubular Brushless Permanent-Magnet Machines. *IEEE Transactions on Magnetics*, 44(9):2195–2203, sep 2008. ISSN 0018-9464. doi: 10.1109/TMAG.2008.2001074. URL http://ieeexplore.ieee.org/document/4604779/.

[54] Michael Galea, Luca Papini, He Zhang, Chris Gerada, and Tahar Hamiti. Demagnetization Analysis for Halbach Array Configurations in Electrical Machines. *IEEE Transactions on Magnetics*, 51(9), 2015. ISSN 00189464. doi: 10.1109/TMAG.2015.2429645. URL https://ieeexplore.ieee.org/abstract/document/7101830.

[55] Songlin Wu, Shaopeng Wu, Weiduo Zhao, and Shumei Cui. Demagnetization Research on PMs in the Halbach Magnetized Pulsed Alternator. *China Electrotechnical Society Transactions on Electrical Machines and Systems*, 3(2):170–177, jun 2019. ISSN 20963564. doi: 10.30941/CESTEMS.2019.00023. URL http://www.cestems.org/uploads/20190625/15614293702094.pdf.

[56] Z Q Zhu. Recent Development of Halbach Permanent Magnet Machines and Applications. In *2007 Power Conversion Conference - Nagoya*, pages K–9–K–16. IEEE, apr 2007. ISBN 1-4244-0843-1. doi: 10.1109/PCCON.2007.372911. URL http://ieeexplore.ieee.org/document/4239126/.

[57] Ask the Van. Q & A: refrigerator magnets, 2011. URL https://van.physics.illinois.edu/qa/listing.php?id=363.

[58] John Elfick. Magnetism. URL http://www.uq.edu.au/_School_Science_Lessons/UNPh29.html.

[59] QuickField. Fridge magnets. URL https://quickfield.com/advanced/fridge_magnet.htm.

[60] Klaus Halbach. Physical and optical properties of rare earth cobalt magnets. *Nuclear Instruments and Methods*, 187(1):109–117, 1981. ISSN 0029554X. doi: 10.1016/0029-554X(81)90477-8. URL https://www.sciencedirect.com/science/article/pii/0029554X81904778.

[61] N A Vinokurov and E B Levichev. Undulators and wigglers for the production of radiation and other applications. *Physics-Uspekhi*, 58 (9):850–871, 2015. ISSN 1063-7869. doi: 10.3367/UFNe.0185.201509b.0917. URL http://stacks.iop.org/1063-7869/58/i=9/a=850?key=crossref.750b225f9f4ac3152e3736949d40d063.

[62] H. Motz. Applications of the Radiation from Fast Electron Beams. *Journal of Applied Physics*, 22(5):527–535, may 1951. ISSN 0021-8979. doi: 10.1063/1.1700002. URL http://aip.scitation.org/doi/10.1063/1.1700002.

[63] Felicia Bolter. Components of a Synchrotron, 2015. URL http://slideplayer.com/slide/2408254/.

[64] C Segre. Wigglers and Undulators, 2010. URL http://www.csrri.iit.edu/$\sim$segre/phys570/10F/lecture_06.pdf.

[65] Riccardo Bartolini. Synchrotron Radiation (John Adams Institute for Accelerator Science, University of Oxford and Diamond Light Source), 2015. URL https://indico.cern.ch/event/356897/contributions/1769130/attachments/709978/974605/JUAS_2015_RB_synchrotron_radiation_III.pdf.

[66] Professor David Attwood. Intro to Synchrotron Radiation, Bending Magnet Radiation, 2007. URL https://people.eecs.berkeley.edu/$\sim$attwood/srms/2007/Lec08.pdf.

[67] Jim Clarke. Insertion Devices Lecture 1 Introduction to Synchrotron Radiation. pages 1–46, 2010. URL https://www.cockcroft.ac.uk/wp-content/uploads/2014/12/Clarke-Lecture-1.pdf.

[68] Marek Stankiewicz. Solaris: New Light for Polish Science, 2015. URL https://indico.cern.ch/event/361988/contributions/1775703/attachments/1166535/1682074/SOLARIS-CAS-NCBJ_F_2015-10-05_.pdf.

[69] Andy Watts, Andrew Vallance, Andrew Whitehead, Chris Hilton, and Al Fraser. The Technology and Economics of In-Wheel Motors. *SAE International Journal of Passenger Cars - Electronic and Electrical Systems*, 3(2):2010–01–2307, 2010. ISSN 1946-4622. doi: 10.4271/2010-01-2307. URL http://papers.sae.org/2010-01-2307/.

[70] Ian Hooper. *Development of in-Wheel Motor Systems for Formula Sae Electric Vehicles*. PhD thesis, The University of Western Australia, 2011. URL http://robotics.ee.uwa.edu.au/theses/2012-REV-InWheelMotor-Hooper-ME.pdf.

[71] H.C. Lovatt, V.S. Ramsden, and B.C. Mecrow. Design of an in-wheel motor for a solar-powered electric vehicle. In *Eighth International Conference on Electrical Machines and Drives*, volume 1997, pages 234–238. IEE, 1997. ISBN 0 85296 696 2. doi: 10.1049/cp:19971074. URL https://digital-library.theiet.org/content/conferences/10.1049/cp_19971074.

[72] R.F. Post, T.K. Fowler, and S.F. Post. A high-efficiency electromechanical battery. *Proceedings of the IEEE*, 81(3):462–474, mar 1993. ISSN 00189219. doi: 10.1109/5.241483. URL http://ieeexplore.ieee.org/document/241483/.

[73] R.F. Post. A new look at an old idea - The electromechanical battery. *Science and Technology Review*, (April 1):12–19, 1996. URL https://www.osti.gov/biblio/394101-new-look-old-idea-electromechanical-battery.

[74] Brad Paden, Nelson Groom, and James F. Antaki. Design Formulas for Permanent-Magnet Bearings. *Journal of Mechanical Design*, 125(4):734–738, dec 2003. ISSN 1050-0472. doi: 10.1115/1.1625402. URL https://asmedigitalcollection.asme.org/mechanicaldesign/article/125/4/734/463910/Design-Formulas-for-PermanentMagnet-Bearings.

[75] Mark Siebert, Ben Ebihara, and Ralph Jansen. A Passive Magnetic Bearing Flywheel. (February 2002), 2002. URL https://ntrs.nasa.gov/archive/nasa/casi.ntrs.nasa.gov/20020038851.pdf.

[76] Wilfredo Morales, Robert Fusaro, and Albert Kascak. Permanent Magnetic Bearing for Spacecraft Applications. *Tribology Transactions*, 46(3):460–464, jan 2003. ISSN 1040-2004. doi: 10.1080/10402000308982651. URL http://www.tandfonline.com/doi/abs/10.1080/10402000308982651.

[77] Christopher A. Gallo. Halbach Magnetic Rotor Development. *NASA Technical Information Service*, (February):23, 2008. URL http://ntrs.nasa.gov/search.jsp?R=20080013147.

[78] Young-Man Choi, Moon G. Lee, Dae-Gab Gweon, and Jaehwa Jeong. A new magnetic bearing using Halbach magnet arrays for a magnetic levitation stage. *Review of Scientific Instruments*, 80(4):045106, apr 2009. ISSN 0034-6748. doi: 10.1063/1.3116482. URL http://aip.scitation.org/doi/10.1063/1.3116482.

[79] John H. Glenn Research Center. Axial Halbach Magnetic Bearings, 2008. URL https://www.techbriefs.com/component/content/article/tb/techbriefs/mechanics-and-machinery/2954.

[80] John H. Glenn Research Center. Radial Halbach Magnetic Bearing, 2009. URL https://www.techbriefs.com/component/content/article/tb/techbriefs/mechanics-and-machinery/5424.

[81] Dennis J Eichenberg, Christopher A Gallo, and William K Thompson. Development and Testing of an Axial Halbach Magnetic Bearing. (July), 2006. URL https://ntrs.nasa.gov/archive/nasa/casi.ntrs.nasa.gov/20060028452.pdf.

[82] Dennis J Eichenberg, Christopher A Gallo, and William K Thompson. Development and Testing of a Radial Halbach Magnetic Bearing. *NASA STI Program*, (December):1–23, 2006. URL https://ntrs.nasa.gov/archive/nasa/casi.ntrs.nasa.gov/20070006849.pdf.

[83] University of Edinburgh. WES Project Neptune, 2017. URL https://www.cgen.eng.ed.ac.uk/wes-project-neptune.

[84] A.S. McDonald, M. Benatmane, and M.A. Mueller. A multi-stage axial flux permanent magnet machine for direct drive wind turbines. In *IET Conference on Renewable Power Generation (RPG 2011)*, volume 2011, pages 15–15. IET, 2011. ISBN 978-1-84919-536-2. doi: 10.1049/cp.2011.0105. URL https://digital-library.theiet.org/content/conferences/10.1049/cp.2011.0105.

[85] Neil Hodgins, Ozan Keysan, Alasdair McDonald, and Markus Mueller. Linear generator for direct drive wave energy applications. *19th International Conference on Electrical Machines, ICEM 2010*, pages 1–6, 2010. doi: 10.1109/ICELMACH.2010.5607840. URL https://ieeexplore.ieee.org/document/5607840.

[86] University of Edinburgh. C-GEN Technology. URL https://www.cgen.eng.ed.ac.uk/c-gen-technology.

[87] A.S. McDonald, N. Al-Khayat, D. Belshaw, M. Ravilious, A. Kumaraperumal, A.M. Benatamane, M. Galbraith, D. Staton, K. Benoit, and M. Mueller. 1MW multi-stage air-cored permanent magnet generator for wind turbines. In *6th IET International Conference on Power Electronics, Machines and Drives (PEMD 2012)*, volume 2012, pages D11–D11. IET, 2012. ISBN 978-1-84919-616-1. doi: 10.1049/

cp.2012.0319. URL https://digital-library.theiet.org/content/conferences/10.1049/cp.2012.0319.

[88] Markus Mueller. C-GEN Direct Drive Generator [Power Point Presentation], 2017. URL https://www.cgen.eng.ed.ac.uk/sites/cgen.eng.ed.ac.uk/files/attachments/C-GENShortpresentation.pdf.

[89] University of Edinburgh. Professor Markus Mueller awarded £2.5m by Wave Energy Scotland, 2017. URL https://www.eng.ed.ac.uk/about/news/20170316/professor-markus-mueller-awarded-{\protect\T1\textsterling}25m-wave-energy-scotland.

[90] Neil Hodgins, A.S. McDonald, J. Shek, Ozan Keysan, and Markus Mueller. Current and Future Developments of the C-GEN Lightweight Direct Drive Generator for Wave & Tidal Energy. *Proceedings of the 8th European Wave and Tidal Energy Conference*, pages 352–359, 2009. URL https://www.research.ed.ac.uk/portal/en/publications/current-and-future-developments-of-the-cgen-lightweight-direct-drive-generator-for-wave--tidal-energy(18bac957-c813-4c85-9dbe-4910fcebfe4a).html.

[91] Markus A. Mueller, Joseph Burchell, Yew Chuan Chong, Ozan Keysan, Alasdair McDonald, Mike Galbraith, and Estanislao J.P. Echenique Subiabre. Improving the thermal performance of rotary and linear air-cored permanent magnet machines for direct drive wind and wave energy applications. *IEEE Transactions on Energy Conversion*, 34 (2):773–781, 2019. ISSN 08858969. doi: 10.1109/TEC.2018.2881340. URL https://strathprints.strath.ac.uk/66192/1/Mueller_etal_IEEE_TEC_2018_Improving_the_thermal_performance_of_rotary_and_linear_air_cored_permanent_magnet_machine.pdf.

[92] Offshore Wind. NGenTec Limited Secures GBP 2 Million in Funding (UK), 2010. URL https://www.offshorewind.biz/2010/12/16/ngentec-limited-secures-gbp-2-million-in-funding-uk/.

[93] Offshore Wind. NGenTec Announces Industrial Partnership for Innovative Generator Technology with David Brown (UK), 2011. URL https://www.offshorewind.biz/2011/02/16/ngentec-announces-industrial-partnership-for-innovative-generator-technology-with-david-brown-uk/.

[94] Neil Hodgins, Ozan Keysan, Alasdair S. McDonald, and Markus A. Mueller. Design and Testing of a Linear Generator for Wave-Energy Applications. *IEEE Transactions on Industrial Electronics*, 59(5):2094–2103, may 2012. ISSN 0278-0046. doi: 10.1109/TIE.2011.2141103. URL http://ieeexplore.ieee.org/document/5746524/.

[95] UK Research and Innovation. WindSurf- A self-starting, active-pitch, vertical-axis wind turbine, 2016. URL https://gtr.ukri.org/projects?ref=EP%2FP51147X%2F1.

[96] Wave Energy Scotland. Mocean WEC: Blue Horizon, 2015. URL https://www.waveenergyscotland.co.uk/programmes/details/novel-wave-energy-converter/mocean-wave-energy-converter/.

[97] Mocean Energy. Mocean Energy selects C-GEN technology for wave power take-off, 2019. URL https://www.mocean.energy/mocean-energy-selects-c-gen-technology-for-wave-power-take-off/.

[98] Yew Chuan Chong, Estanislao J.P. Echenique Subiabre, Markus A. Mueller, John Chick, David A. Staton, and Alasdair S. McDonald. The ventilation effect on stator convective heat transfer of an axial-flux permanent-magnet machine. *IEEE Transactions on Industrial Electronics*, 61(8):4392–4403, 2014. ISSN 02780046. doi: 10.1109/TIE.2013.2284151. URL https://www.research.ed.ac.uk/portal/files/17202978/06616617.pdf.

[99] E. P. Furlani. A three-dimensional field solution for axially-polarized multipole disks. *Journal of Magnetism and Magnetic Materials*, 135 (2):205–214, 1994. ISSN 03048853. doi: 10.1016/0304-8853(94)90347-6. URL https://www.sciencedirect.com/science/article/abs/pii/0304885394903476.

[100] J L G Janssen, J J H Paulides, and E A Lomonova. The Developments in the Analytical Expressions of the Interaction Force Between Cuboidal Permanent Magnets. *Electrimacs 2011*, 1(June):6–8, 2011. URL https://www.researchgate.net/publication/305317978_The_developments_in_the_analytical_expressions_of_the_interaction_force_between_cuboidal_permanent_magnets.

[101] Edward P. Furlani. *Permanent Magnet and Electromechanical Devices*, volume 53. Elsevier, 2001. ISBN 9780122699511. doi: 10.1016/B978-

0-12-269951-1.X5000-1. URL https://www.sciencedirect.com/book/9780122699511/permanent-magnet-and-electromechanical-devices.

[102] Peter Campbell. *Permanent Magnet Materials and their Application*. Cambridge University Press, Cambridge, 1994. ISBN 9780511623073. doi: 10.1017/CBO9780511623073. URL http://ebooks.cambridge.org/ref/id/CBO9780511623073.

[103] Romain Ravaud and Guy Lemarquand. Comparison of the Coulombian and Amperian Current Models for Calculating the Magnetic Field Produced By Radially Magnetized Arc-Shaped Permanent Magnets. *Progress In Electromagnetics Research*, 95(June):309–327, 2009. ISSN 1559-8985. doi: 10.2528/PIER09042105. URL http://www.jpier.org/PIER/pier.php?paper=09042105.

[104] William K Thompson. Three-Dimensional Field Solutions for Multi-Pole Cylindrical Halbach Arrays in an Axial Orientation. 2006. URL https://ntrs.nasa.gov/archive/nasa/casi.ntrs.nasa.gov/20060047693.pdf.

[105] G Ramian, L Elias, and I Kimel. Micro-undulator FELS. *Nuclear Instruments and Methods in Physics Research Section A: Accelerators, Spectrometers, Detectors and Associated Equipment*, 250(1-2):125–133, sep 1986. ISSN 01689002. doi: 10.1016/0168-9002(86)90872-7. URL https://linkinghub.elsevier.com/retrieve/pii/0168900286908727.

[106] Isidro Kimel and Luis R. Elias. Micro-undulator fields. *Nuclear Instruments and Methods in Physics Research Section A: Accelerators, Spectrometers, Detectors and Associated Equipment*, 296(1-3):611–618, oct 1990. ISSN 01689002. doi: 10.1016/0168-9002(90)91276-H. URL https://linkinghub.elsevier.com/retrieve/pii/016890029091276H.

[107] RF Post and L Nguyen. The Design of Halbach Arrays for Inductrack Maglev Systems. 2008. URL http://citeseerx.ist.psu.edu/viewdoc/download?doi=10.1.1.589.3657&rep=rep1&type=pdf.

[108] Klaus Halbach. Strong Rare Earth Cobalt Quadrupoles. *IEEE Transactions on Nuclear Science*, 26(3):3882–3884, jun 1979. ISSN 0018-9499. doi: 10.1109/TNS.1979.4330638. URL http://ieeexplore.ieee.org/document/4330638/.

[109] P. Hammond. Electric and magnetic images. *Proceedings of the IEE Part C: Monographs*, 107(12):306, 1960. ISSN 03698904. doi: 10.1049/pi-c.1960.0047. URL https://digital-library.theiet.org/content/journals/10.1049/pi-c.1960.0047.

[110] Sang Ho Lee, Su Beom Park, Soon O. Kwon, Ji Young Lee, Jung Jong Lee, Jung Pyo Hong, and Jin Hur. Characteristic analysis of the slotless axial-flux type brushless DC motors using image method. *IEEE Transactions on Magnetics*, 42(4):1327–1330, 2006. ISSN 00189464. doi: 10.1109/TMAG.2006.871922. URL https://ieeexplore.ieee.org/document/1608459.

[111] Tze Fun Chan and Loi Lei Lai. Computation of air-gap field in an axial-flux permanent-magnet machine using the method of images. *2009 IEEE International Electric Machines and Drives Conference, IEMDC '09*, (1):1647–1651, 2009. doi: 10.1109/IEMDC.2009.5075424. URL https://ieeexplore.ieee.org/document/5075424.

[112] J. L.G. Janssen, J. J.H. Paulides, and E. A. Lomonova. 3D analytical field calculation using triangular magnet segments applied to a skewed linear permanent magnet actuator. *COMPEL - The International Journal for Computation and Mathematics in Electrical and Electronic Engineering*, 29(4):984–993, 2010. ISSN 03321649. doi: 10.1108/03321641011044406. URL https://www.researchgate.net/publication/233550251_3D_analytical_field_calculation_using_triangular_magnet_segments_applied_to_a_skewed_linear_permanent_magnet_actuator.

[113] M. F. J. Kremers, J. J. H. Paulides, J. L. G. Janssen, and E. A. Lomonova. Analytical 3-D Force Calculation of a Transverse Flux Machine. *Electrimacs 2014*, (April 2015):2668–2673, 2014. URL https://www.researchgate.net/publication/274635822_ANALYTICAL_3-D_FORCE_CALCULATION_OF_A_TRANSVERSE_FLUX_MACHINE.

[114] J. L G Janssen, J. J H Paulides, L. Encica, and E. Lomonova. Analytical modeling of permanent magnets on a soft magnetic support for a suspension system. *Proceedings of the 11th International Conference on Electrical Machines and Systems, ICEMS 2008*, pages 3825–3830, 2008. URL https://ieeexplore.ieee.org/document/4771445.

[115] E. P. Furlani. Field analysis and optimization of NdFeB axial field permanent magnet motors. *IEEE Transactions on Magnetics*, 33(5 PART

2):3883–3885, 1997. ISSN 00189464. doi: 10.1109/20.619603. URL https://ieeexplore.ieee.org/document/619603.

[116] Surong Huang, Jian Luo, F. Leonardi, and T.A. Lipo. A comparison of power density for axial flux machines based on general purpose sizing equations. *IEEE Transactions on Energy Conversion*, 14(2):185–192, jun 1999. ISSN 08858969. doi: 10.1109/60.766982. URL http://ieeexplore.ieee.org/document/766982/.

[117] Okechukwu G. Ubani, Markus A. Mueller, John Chick, and Alasdair McDonald. Analysis of an air-cored axial flux permanent magnet machine with Halbach array. *IET Conference Publications*, 2016(CP684):1–6, 2016. doi: 10.1049/cp.2016.0249. URL https://ieeexplore.ieee.org/document/7739437.

[118] Arnold Magnetic Technologies. N33H - Sintered Neodymium-Iron-Boron Magnets. URL https://www.arnoldmagnetics.com/wp-content/uploads/2017/11/N33-151021.pdf.

[119] J. Ofori-Tenkorrang and J.H. Lang. A comparative analysis of torque production in Halbach and conventional surface-mounted permanent-magnet synchronous motors. In *IAS '95. Conference Record of the 1995 IEEE Industry Applications Conference Thirtieth IAS Annual Meeting*, volume 1, pages 657–663. IEEE. ISBN 0-7803-3008-0. doi: 10.1109/IAS.1995.530362. URL http://ieeexplore.ieee.org/document/530362/.

[120] Jim Clarke. Insertion Devices Lecture 4 Permanent Magnet Undulators. URL https://www.cockcroft.ac.uk/wp-content/uploads/2014/12/Lecture-41.pdf.

[121] Mikael Alatalo. *Permanent magnet machines with air gap windings and integrated teeth windings*. Number 288. 1996. ISBN 9171973125. URL http://publications.lib.chalmers.se/records/fulltext/1106/1106.pdf.

[122] Bing Xia, Jian Xin Shen, Patrick Chi Kwong Luk, and Weizhong Fei. Comparative study of air-cored axial-flux permanent-magnet machines with different stator winding configurations. *IEEE Transactions on Industrial Electronics*, 62(2):846–856, 2015. ISSN 02780046. doi: 10.1109/TIE.2014.2353012. URL https://ieeexplore.ieee.org/abstract/document/6888515.

[123] Maarten J. Kamper, Rong Jie Wang, and Francois G. Rossouw. Analysis and performance of axial flux permanent-magnet machine with air-cored nonoverlapping concentrated stator windings. *IEEE Transactions on Industry Applications*, 44(5):1495–1504, 2008. ISSN 00939994. doi: 10.1109/TIA.2008.2002183. URL https://ieeexplore.ieee.org/abstract/document/4629361.

[124] Gang Lei, Jianguo Zhu, Youguang Guo, Chengcheng Liu, and Bo Ma. A review of design optimization methods for electrical machines. *Energies*, 10 (12), 2017. ISSN 19961073. doi: 10.3390/en10121962. URL https://www.mdpi.com/1996-1073/10/12/1962.

[125] Ankan Mishra, Sukhomay Pal, and Swarup Bag. Electromagnetic Transient-Thermal Modeling of High-Frequency Induction Welding of Mild Steel Plates. pages 407–415. 2020. doi: 10.1007/978-981-32-9487-5_32. URL http://link.springer.com/10.1007/978-981-32-9487-5_32.

[126] Motor Design Limited. URL https://www.motor-design.com/.

[127] Motor Engineer. URL http://www.motor-engineer.net/.

[128] COMSOL. Finite Element Mesh Refinement. URL https://uk.comsol.com/multiphysics/mesh-refinement.

[129] Estanislao J.P. Echenique, Ozan Keysan, and Markus A. Mueller. Rotor loss prediction in air-cored permanent magnet machines. *Proceedings of the 2013 IEEE International Electric Machines and Drives Conference, IEMDC 2013*, (November 2014):303–310, 2013. doi: 10.1109/IEMDC.2013.6556268. URL https://www.researchgate.net/publication/261283710_Rotor_loss_prediction_in_air-cored_permanent_magnet_machineshttps://www.researchgate.net/publication/261283710_Rotor_loss_prediction_in_air-cored_permanent_magnet_machines.

[130] Siemens. Simcenter 3D Low Frequency EM User Guide, 2018. URL https://docs.plm.automation.siemens.com/docs/nx/1899/en_US/sc3d_LFEM/Simcenter3D-LFEM_UserGuide.pdf.

[131] Altair Limited. Simple Coil with Core. URL https://forum.altair.com/topic/23909-simple-coil-with-core/.

[132] Walid El, Fezzani Abdessattar, and Ben Amor. Importance of the Mesh Element and the Material Selection in Linear Actuator. 1(1):14–20, 2014. URL https://www.researchgate.net/publication/266705550_Importance_of_the_Mesh_Element_and_the_Material_Selection_in_Linear_Actuator.

[133] Infolytica Corporation. Brushless DC Motor Calculating Air Gap Flux with MagNet, 2005. URL http://www-3.unipv.it/electric/cad/progetto_mem/BDC_Air_Gap_Flux.pdf.

[134] N. F. Lombard and M. J. Kamper. Analysis and performance of an ironless stator axial flux PM machine. *IEEE Transactions on Energy Conversion*, 14 (4):1051–1056, 1999. ISSN 08858969. doi: 10.1109/60.815027. URL https://ieeexplore.ieee.org/document/815027.

[135] F. Caricchi, F. Crescimbini, O. Honorzti, G. Lo Bianco, and E. Santini. Performance of coreless-winding axial-flux permanent-magnet generator with power output at 400 Hz-3000 rev/min. In *IAS '97. Conference Record of the 1997 IEEE Industry Applications Conference Thirty-Second IAS Annual Meeting*, volume 1, pages 61–66. IEEE. ISBN 0-7803-4067-1. doi: 10.1109/IAS.1997.643009. URL http://ieeexplore.ieee.org/document/643009/.

[136] Rong Jie Wang and Maarten J. Kamper. Calculation of eddy current loss in axial field permanent-magnet machine with coreless stator. *IEEE Transactions on Energy Conversion*, 19(3):532–538, 2004. ISSN 08858969. doi: 10.1109/TEC.2004.832043. URL https://ieeexplore.ieee.org/abstract/document/1325291?section=abstract.

[137] Marc T. Thompson. Practical issues in the use of NdFeB permanent magnets in maglev, motors, bearings, and eddy current brakes. *Proceedings of the IEEE*, 97(11):1758–1767, 2009. ISSN 00189219. doi: 10.1109/JPROC.2009.2030231. URL https://ieeexplore.ieee.org/document/5282572.

[138] Xu Yang, Dean Patterson, Jerry Hudgins, and Jessica Colton. FEA estimation and experimental validation of solid rotor and magnet eddy current loss in single-sided axial flux permanent magnet machines. *2013 IEEE Energy Conversion Congress and Exposition, ECCE 2013*, (December):3202–3209, 2013. doi: 10.1109/ECCE.2013.6647120.

URL https://www.researchgate.net/publication/261259749_FEA_Estimation_and_Experimental_Validation_of_Solid_Rotor_and_Magnet_Eddy_Current_Loss_in_Single-sided_Axial_Flux_Permanent_Magnet_Machines/link/55c2347008aebc967defd6a4/download.

[139] Konstantina Bitsi, Damian Kowal, and Reza Rajabi Moghaddam. 3-D FEM investigation of eddy current losses in rotor lamination steel sheets. *Proceedings - 2018 23rd International Conference on Electrical Machines, ICEM 2018*, pages 1047–1053, 2018. doi: 10.1109/ICELMACH.2018.8507048. URL https://www.diva-portal.org/smash/get/diva2:1259048/FULLTEXT01.pdf.

[140] Juha Pyrhnen, Tapani Jokinen, and Valria Hrabovcov. *Design of Rotating Electrical Machines*. John Wiley & Sons, Ltd, Chichester, UK, dec 2008. ISBN 9780470740095. doi: 10.1002/9780470740095. URL http://doi.wiley.com/10.1002/9780470740095.

[141] Siemens MagNet. Materials - permanent magnets: demagnetization. URL https://support.sw.siemens.com/product/1067459531/knowledge-base/MG600714.

[142] A. H. Isfahani, S. Vaez-Zadeh, and M. A. Rahman. Performance improvement of permanent magnet machines by modular poles. *IET Electric Power Applications*, 3(4):343–351, 2009. ISSN 17518660. doi: 10.1049/iet-epa.2007.0391. URL https://ieeexplore.ieee.org/document/5154115.